NASA Contractor Report 4262

Mesoscale Acid Deposition Modeling Studies

Michael L. Kaplan, F. H. Proctor,
John W. Zack, V. Mohan Karyampudi,
H. Price, M. D. Bousquet,
and G. D. Coats

CONTRACT NAS1-18336
DECEMBER 1989

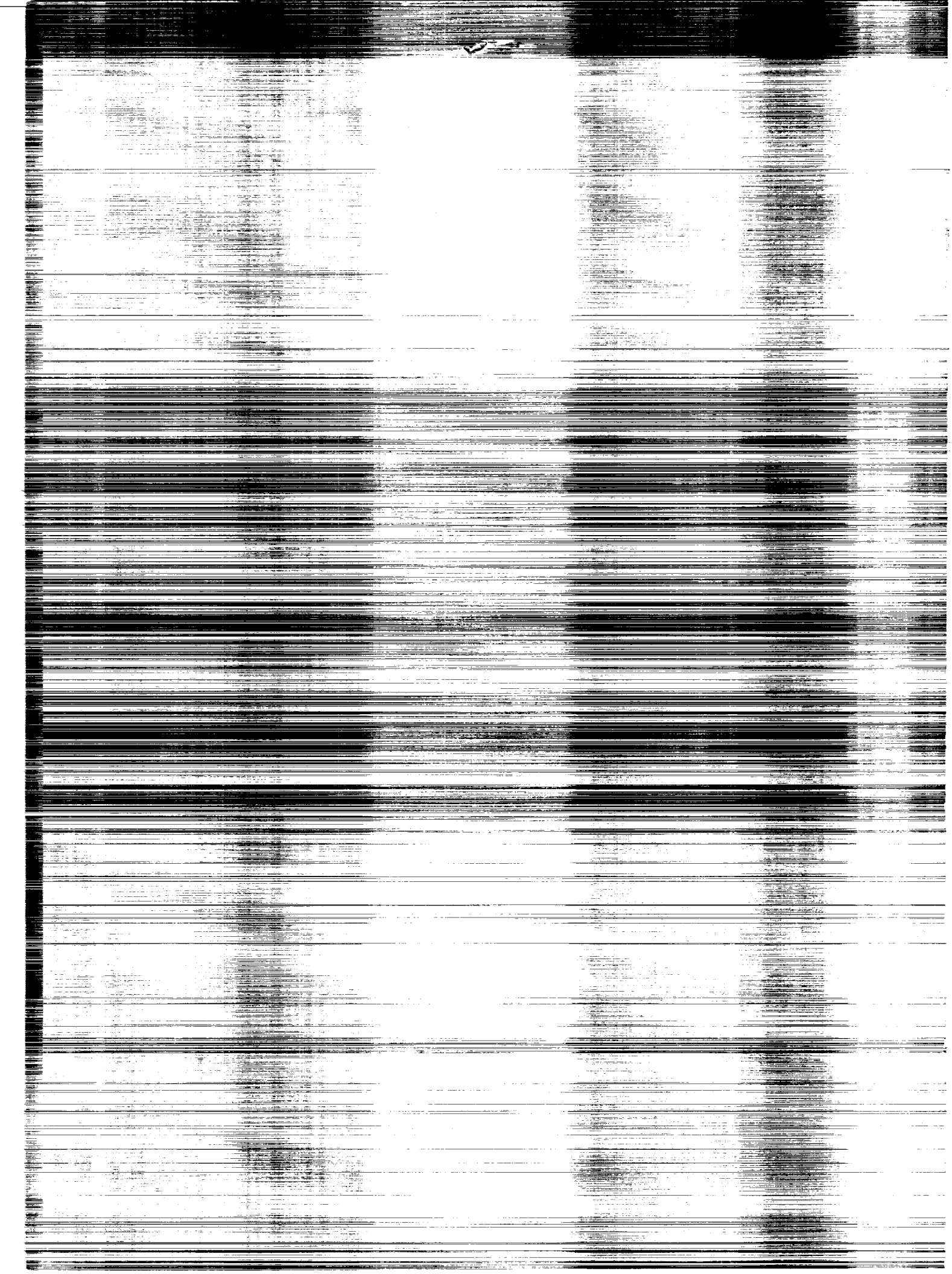

NASA Contractor Report 4262

Mesoscale Acid Deposition Modeling Studies

Michael L. Kaplan, F. H. Proctor,
John W. Zack, V. Mohan Karyampudi,
P. E. Price, M. D. Bousquet,
and G. D. Coats

MESO, Inc.
Hampton, Virginia

Prepared for
Langley Research Center
under Contract NAS1-18336

National Aeronautics and
Space Administration
Office of Management
Scientific and Technical
Information Division

1989

EXECUTIVE SUMMARY

This report summarizes the work performed by scientists and programmers at MESO Inc. in support of the National Aeronautics and Space Administration and the Environmental Protection Agency under Contract NAS1-18336. The work performed can be logically partitioned into two basic applied research topic areas : first, the use of meso and cloudscale numerical atmospheric simulation models in support of the scientific goals of the joint EPA/DOE Mesoscale Acid Deposition Studies Project, and second, the use of cloud and mesoscale numerical atmospheric simulation models in support of the joint NASA/FAA Convection-Initiated Low-Level Wind Shear Program. The two numerical models employed in the applied research are the Mesoscale Atmospheric Simulation System (MASS) and the Terminal Area Simulation System (TASS) both of which were developed primarily under the support of NASA by individuals presently working at MESO Inc.

The work performed in support of the EPA/DOE MADS Project involved : 1) the development of meteorological data bases for the initialization of chemistry models, 2) the testing and implementation of new planetary boundary layer parameterization schemes in the MASS model, 3) the simulation of transport and precipitation for MADS case studies employing the MASS model, 4) the use of the TASS model in the simulation of cloud statistics and the complex transport of conservative tracers within simulated cumuloform clouds, and 5) the optimization of atmospheric chemistry simulation codes for use on vector supercomputing systems.

The work performed in support of the NASA/FAA Wind Shear Program involved : 1) the use of the TASS model in the simulation of the dynamical processes within convective cloud systems which result in microburst phenomena, 2) the analyses of the sensitivity of microburst intensity and general characteristics as a function of the atmospheric environment within which they are formed, 3) the publication of TASS model microburst simulation results and comparisons to observed data sets from aircraft affected by microbursts, 4) the calculation, employing simulation results, of performance factors as modified by the strong wind shears accompanying microburst, and 5) the generation of simulated wind shear data bases for use by the aviation meteorological community in the evaluation of flight hazards caused by microbursts.

These tasks were performed employing computers at the NASA Langley Research Center for the aforementioned Federal agencies under contract NAS1-18336 exclusively by scientists and programmers at MESO Inc. during the period from July 1986 to July 1989.

TABLE OF CONTENTS

SECTION 1 - INTRODUCTION

For several years the National Aeronautics and Space Administration has supported the development and testing of two atmospheric numerical simulation models, i.e., the Mesoscale Atmospheric Simulation System (MASS) and the Terminal Area Simulation System (TASS) on their supercomputer systems (Kaplan et al., 1982; Proctor, 1987a,b). These models represent state-of-the-science tools which can be employed to accurately simulate the evolution of complex atmospheric circulation systems for periods of time ranging from minutes to days and over spatial regions ranging from an airport runway to North America (Kaplan et al., 1984; Zack and Kaplan, 1987; Proctor, 1989a,b). As tools which have been employed for use in the simulation of a variety of fine scale atmospheric circulations, they represent a national resource which can be employed for use by a variety of Federal agencies in the simulation of atmospheric processes which significantly impact the daily lives of the American public as well as affecting the national defense. Two atmospheric problems which represent significant challenges to the scientific research community and also affect the daily activities of many Americans are acid rain and the effect of low-level wind shear on aircraft safety. The acid rain problem is of critical interest to the Environmental Protection Agency and the Department of Energy. Both of these agencies are involved in the Mesoscale Acid Deposition Studies Project which is designed to study the impact of an urban source on regional acid deposition (Patrinos, 1985). The effect of wind shear on aircraft safety is of critical interest to the Federal Aviation Administration in their pursuit of understanding the causes of convection-initiated low-level wind shear. NASA has an interest in both problem areas as well as the facilities to perform the computer modeling at the Langley Research Center. MESO Inc.'s scientists have developed and applied these two models to a variety of problem areas and, hence, represented a unique pool of expertise to apply these tools to specific topics within each of the two general problem areas (Proctor, 1985,1986; Zack and Kaplan, 1987).

In this report report we will provide a detailed description of the work performed in the twelve tasks assigned under this contract between July 1986 and July 1989. The second section describes the requirements for each of the tasks. Section three describes the work performed, problems encountered, and results accomplished under the EPA/DOE supported tasks. The same description for the NASA/FAA supported tasks

is presented in section four. Section five summarizes the report. All references, tables, and figures are listed sequentially after section five.

SECTION II - CHRONOLOGY OF TASKS

This section briefly describes each task assignment and the expected deliverable(s). A breakdown of the starting and completion date, man-hour estimate, and total cost limitation for each of the assigned tasks is listed in Table 1. The tasks can be organized into two broad categories; those which supported the EPA/DOE MADS Project and those which supported the NASA/FAA Low-Level Wind Shear Program. Furthermore, each of the above categories can be partitioned into task subgroups in which the former category involved supporting the STEM chemistry model, testing new planetary boundary layer parameterization schemes in MASS, and employing TASS to study transport, entrainment, and cloud statistics and the latter category involved simulating microbursts in 2 and 3-dimensional environments, publishing journal articles, and calculating wind shear-induced aircraft performance factors.

EPA/DOE TASK ASSIGNMENTS

TASK ASSIGNMENT I - PERFORM STEM II CHEMISTRY MODEL SIMULATIONS

Take the existing 3-dimensional version of the STEM II chemical model to be provided by Dr. Greg Carmichael of the University of Iowa (Carmichael and Peters, 1984). Modify the model such that it can be interfaced with the modified NAPAP emissions data base to be provided by Dr. Len Peters of the University of Kentucky. Deliverables will consist of two simulations from the Mesoscale Acid Deposition Studies Field Experiment as well as all appropriate output products as dictated by the EPA contract monitor. Also, explore possible approaches for STEM II model optimization.

TASK ASSIGNMENT II - TEST BINKOWSKI PBL CODE

Continue development of a high resolution version of the Binkowski PBL code (Binkowski, 1983). Deliverable will be a one-dimensional version of the code which is operational on the MESO Inc. personal computer system. Prepare a plan for the integration of the new PBL code into the 3-dimensional MASS model.

TASK ASSIGNMENT V - IMPLEMENT BLACKADAR PBL INTO MASS 4.0

Implement a version of the Blackadar high resolution PBL code into the MASS 4.0 model. Modify the code where appropriate, including adding changes to the moisture formulation. Test the model with a 3-dimensional simulation of the April 10 1979 AVE-SESAME case study. Once it has been implemented and tested, perform a nested grid simulation of the May 3 1985 MADS case study. Compare the simulation with the results from the MASS 3.0 simulation of the May 3 1985 case study.

TASK ASSIGNMENT VI -PRODUCE DATA BASES FOR THE STEM II "ENGINEERING MODEL"

Produce data bases for the STEM II 'Engineering Model'. These data bases will be derived from the coarse mesh (i.e., 50 km grid mesh) version of MASS 3.0. Produce data bases as specified by personnel at the University of Iowa who maintain this version of STEM. These case studies will include the three MADS case study simulations performed with MASS 3.0. Modify the initial structure of the data bases relative to the grid as specified by the University of Iowa personnel. Also produce any additional programming support necessary to maintain and update the half precision (32 bit) version of STEM.

TASK ASSIGNMENT VIII - RUN TWO MASS MODEL SIMULATIONS FROM THE WASHINGTON D. C. FIELD EXPERIMENT

Run two nested grid simulations with the MASS model for cases from the EPA Washington D. C. field experiment. These cases are the 8 November 1986 and 28 March 1987 dates. High resolution terrain and asynoptic moisture data will be used for the nested grid simulations. The output from these simulations will be used to analyze the transport of atmospheric constituents which occurred in the vicinity of Washington D. C. on these dates. A detailed comparison between the simulated precipitation and the precipitation observed by the standard NWS observing sites and the special EPA field observations will be made in order to assess the realism of the simulations.

TASK ASSIGNMENT IX - PRODUCE AXISYMMETRIC TASS MODEL STATISTICS ON NONSHEARING CUMULUS CLOUDS

Run the axisymmetric version of the TASS cloud model on a significant sample of cases in which there is convection with little or no vertical wind shear. The cases will be representative of a range of convective phenomena from shallow nonprecipitating cumulus clouds to deep cumulonimbus which produce heavy rain. The number and type distribution of cases will be specified by the project director. Statistics which relate the strength of the cloud updraft to a variety of external parameters will be compiled. The parameters of interest will be specified by the project director.

TASK ASSIGNMENT XI - EMPLOY INERT TRACERS IN THE 3-DIMENSIONAL TASS MODEL TO CALCULATE CLOUD ENTRAINMENT STATISTICS

Conduct several experiments with the three-dimensional version of TASS and examine the significance of both cloud top and lateral entrainment. The experiments shall examine entrainment for a range of cloud sizes varying from shallow nonprecipitating cumulus to small cumulonimbus. Entrainment rates are to be assessed by injecting inert tracers at various model layers. Statistics which relate cloud size, positive buoyant energy, cloud base mass flux, and entrainment rates shall be compiled for a particular ambient vertical wind shear.

NASA/FAA TASK ASSIGNMENTS

TASK ASSIGNMENT III - PRODUCE AXISYMMETRIC TASS SIMULATIONS FOR THE DFW MICROBURST CASE STUDY

Produce two simulations with the axisymmetric version of the TASS model for the August 2 1985 Dallas-Ft. Worth (DFW) microburst case study. The first simulation will employ a 10 meter grid mesh length and represent a first attempt/quick look simulation with a simple initialization. Then the case will be simulated again with a more comprehensive and sophisticated initialization and a much more detailed analysis will be performed. Compare these two simulations' results to

the available observed data and the simulation results from the 3-dimensional TASS model simulation.

TASK ASSIGNMENT IV - PRODUCE THE FIRST DRAFT OF A JOURNAL ARTICLE ON MICROBURST SENSITIVITY STUDIES WITH THE AXISYMMETRIC TASS MODEL

Produce the first working draft of a paper to be submitted to a major scientific journal on the results of numerical sensitivity studies with the axisymmetric TASS model. The paper will emphasize model results and the sensitivity of the model simulation of downburst/microburst phenomena to differing initial environments. Once the first draft is produced, the paper will be modified appropriately and submitted for publication.

TASK ASSIGNMENT VII - PRODUCE DATA TAPES, OUTPUT PLOTS, AND JOURNAL ARTICLES FROM TASS AXISYMMETRIC MICROBURST SIMULATIONS

Produce data that supports the request made to NASA by NOAA regarding pathological microburst cases. Data produced should be that which is already on hand; no new numerical experiments are required. Produce five magnetic tapes based on data derived from the axisymmetric TASS simulation of the DFW microburst case. The data word at each grid point must include liquid water content, reflectivity, wind components, temperature, and pressure. The previous tapes made for the June 30 1982 Denver case could be used as a model. Produce a final draft of the first of two microburst papers and submit to a major scientific journal. This first paper emphasizes microburst dynamics and structure. Produce additional plots of profiles of data from the airplane flight data recorder for the DFW microburst case study. These data will be closely compared to the TASS model simulation. Complete analyses/comparison of the model simulation to the flight data information. Produce a first draft of a second paper on microburst phenomena to be, eventually, submitted to a major scientific journal. This paper will emphasize microburst sensitivity to precipitation distribution, precipitation intensity, environment, effect of low-level inversions, and effect of rotation on microburst structure.

TASK ASSIGNMENT X - DEVELOP SOFTWARE FOR COMPUTING F-FACTORS FOR FLIGHT PATH TRAJECTORIES FROM AXISYMMETRIC TASS AND PRODUCE THREE-DIMENSIONAL TASS SENSITIVITY STUDIES

Develop software for computing F-factors for simple flight path trajectories using data from the axisymmetric version of TASS. Then produce contour plots of the F-factor for simple flight paths using data from the 20 meter resolution DFW simulation. Modify software so F-factors at various flight path angles can be calculated. Then produce contour plots of the F-factor for several flight path angles, again using the 20 meter resolution DFW data. Produce and deliver five data tapes from one of the axisymmetric dry-microburst simulations. The data word is to contain velocity, pressure, temperature, radar reflectivity, snow, rain, and water vapor. Conduct preliminary assessment of simulated multiple microburst interactions using the three-dimensional version of TASS. Conduct preliminary assessment of microburst sensitivity to ambient vertical wind shear. Experiments are to be conducted with the three-dimensional version of TASS, with the microburst being initialized by a prescribed precipitation distribution at the top boundary.

TASK ASSIGNMENT XII - PRODUCE HIGH-RESOLUTION THREE-DIMENSIONAL TASS SIMULATIONS OF MIST AND CCOPE CASE STUDIES

Compute the predictive F-factor based on range bin incremental cells using data from the 20 meter resolution DFW simulation and compare with the F-factors computed for simple flight paths. Complete the production of the film of the 20 m DFW simulation. The color movie film will show the time-evolution of the wind-vector, radar reflectivity, temperature-deviation, vorticity, and F-factor fields. Produce five data tapes from the axisymmetric dry-microburst simulation of the Denver July 14 1982 case. The data word is to contain velocity, pressure, temperature, radar reflectivity, snow, rain, and water vapor. The lower threshold of the radar reflectivity is to be set at -35 dBZ. Produce high-resolution 3-dimensional simulations of the (1) MIST, July 20 1986 storm and (2) CCOPE July 19 Miles City storm. Both simulations are to be compared with actual observations, and the results are to be presented at the "Second International Conference on Cloud Modeling".

SECTION III - DETAILED DESCRIPTION AND RESULTS OF TASKS PERFORMED IN SUPPORT OF THE EPA/DOE MADS PROJECT

TASK ASSIGNMENT I - PERFORM STEM II CHEMISTRY MODEL SIMULATIONS

The first work involved producing two data bases for the STEM II chemistry model. There are two versions of this model. The first is a high resolution (20 km horizontal grid mesh interval) version employing a 10x10x14 3-dimensional matrix of grid points. The vertical structure of the model included layers at 10, 200, 400, 800, 1200, 1600, 2000, 2400, 2800, 3200, 3600, 4000, 5000, and 6000 m heights. The second version of the model is named the 'engineering' version and employs a 40x30 matrix of grid points spaced 50 km apart and employing much simpler chemistry. Initial data from the MASS model data base for the 2-3 May 1985 MADS case study was interpolated to each of the STEM model grids for simulations to be executed by the MESO Inc. programmers. Several attempts were made to run the high resolution version of STEM II for the 2-3 May 1985 case study before a successful 18 hour simulation was achieved. Boundary condition problems caused by the fictitious buildup of large emissions forced several simulations to terminate prematurely thus requiring the restarting of the code which was run in segments on the Cyber 205. Eventually a complete 18 hour simulation was achieved and the output sent to the University of Iowa for plotting.

The STEM II code did not run in a highly efficient manner on the Cyber 205 computer system. In an effort to optimize the model a detailed timing analysis was performed to determine which subroutines were requiring the most CPU time. The results of the timing analysis are depicted in Table 2. It was found that four subroutines required approximately 70% of the total CPU time. These four routines are : 1) LIQRXN, 2) REACTN, 3) TRANS1, and 4) TRANS2. These routines are involved in solving the ordinary differential equations for liquid and gas phase chemistry. A two-part strategy was employed to optimize the model. First, the code was rewritten in half-precision (32 bit) arithmetic to reduce the time per arithmetic operation. Second, the four key subroutines were vectorized to significantly increase their "efficiency" relative to the existing scalar code. After a number of recoding experiments it became apparent that the improvement in the speed of STEM II execution due solely to the use of half-precision arithmetic was

only on the order of 10-20%. This meager improvement was because it was not possible to achieve the desired computational accuracy with all variables in half-precision mode. Hence, only a portion of the code could employ half-precision arithmetic. After discussing these results with the EPA contract monitor at a meeting at DOE headquarters in Washington during January 1987 it was his opinion that further efforts at comprehensive code vectorization would be less fruitful then recoding the model on a new parallel processing system. Also discussed at this meeting were the technical results of the STEM II simulations of the 2-3 May 1985 MADS case study. This version of the model came to be known as MesoSTEM. Probably the most significant aspect of these simulation results concerned the long distance acid deposition which spread southwestward from the New York City metropolitan area into the upper Delaware River Valley region of Pennsylvania and New Jersey. This was the result of simulated strong low-level east-northeasterly windflow and prolonged heavy precipitation. Generally the simulation results matched well against the observed hydrogen peroxide data. A major difficulty with this particular storm is that just prior to the onset of the major frontal storm, there was a convective rain event on the Pennsylvania side of the observational network. Some of the samplers measuring deposition were redeployed, but not all. This event also filled many of the stages of the sequential samplers, and very likely left a very acidic residue on the manifold which connects the funnel to the sampling bottles. Thus, there was some question about the quality of the data at the sites which were affected by the convective episode. Nevertheless, the EPA technical monitor felt that the modeling results were very encouraging.

TASK ASSIGNMENT II - TEST BINKOWSKI PBL CODE

In an effort to improve the parameterization of the atmospheric processes within the planetary boundary layer as simulated by the MASS 3.0 model, several high resolution one-dimensional PBL models were tested. It was anticipated that the most accurate model would be a candidate to replace the existing MASS mixed-layer PBL parameterization scheme which is based on generalized similarity theory (Blackadar and Tennekes, 1968; Zilitinkevich, 1975; Kaplan et al., 1982). Three schemes were planned to be tested employing MESO Inc.'s personal computer system. The first was developed by the EPA contract monitor Frank Binkowski and employed a hybrid K theory formulation (Binkowski, 1983).

The second scheme developed by A. K. Blackadar and used in the Penn State/NCAR model utilizes a modified version of similarity theory (Blackadar, 1979). The third formulation developed by T. Yamada, presently at the Los Alamos National Laboratories, is based on second-order closure theory (Yamada, 1976). Repeated attempts were made to solicit Yamada for a copy of his code but were fruitless due to his desire not to provide MESO Inc. with a copy of his scheme. Therefore, experiments were conducted with only the Binkowski and Blackadar formulations.

The first work under this task involved flowcharting Binkowski's one-dimensional code and performing some additions. These modifications included the addition of an equation for the turbulent flux of water vapor and the transfer of the surface energy budget from Blackadar's PBL formulation to Binkowski's PBL scheme. The 1200 UTC 9 May 1979 case was selected as the test sounding to be employed. This was selected because there was high frequency AVE-SESAME temporal verification data, minimal cloudiness, and the horizontal advection was weak so that the vertical transport processes within the PBL were the most significant factor in the diurnal deepening of the boundary layer. The location selected was of Midland, Texas. First, the 1200 UTC Midland sounding was used to initialize the one-dimensional Blackadar formulation. Results indicated a cold, wet bias probably due to the absence of the horizontal advection of temperature. Then the Binkowski PBL was executed on the same data set. An immediate problem was encountered in which the model became unstable when 60 layers were employed. The problem vanished with the 20 layer version and it was suspected that the problem was due to roundoff errors with the personal computer. The initial experiments assumed the horizontal advection of temperature to be zero and that the observed winds would be substituted for the geostrophic winds. Results from both the Binkowski and Blackadar one-dimensional versions were compared and verified for the 2100 UTC time period which represented nine hour simulations. A tabulation comparing the two PBL simulations to the SESAME observations is presented in Tables 3a-3c. It is apparent from this table that the Binkowski PBL is much colder than both reality and the Blackadar formulation. Notice also the large error in the simulated PBL depth with the Binkowski formulation. Significant errors can also be seen with the Blackadar scheme likely due to the assumption of no horizontal temperature advection and the use of observed U and V wind components in place of the observed geostrophic wind values. Further analysis indicated

a possible problem with the formulation of the friction velocity in Binkowski's PBL. These results were also presented at the MADS Project meeting at DOE headquarters in January 1987.

TASK ASSIGNMENT V - IMPLEMENT BLACKADAR PBL INTO MASS 4.0

Prior to code modifications in MASS 4.0 an extensive review of the PBL code in the Penn State/NCAR model was completed. After completing this review the structure of the MASS sigma layers was modified so that variable depth vertical layering could be employed. This permitted the concentration of vertical layers near the earth's surface and greatly improved vertical resolution within the PBL. Modifications to the MASS data preprocessor code were necessary so that the initial data could be produced for nonuniformly-spaced sigma layers. Additionally, MESO programmers modified the preprocessor code to utilize the optimum interpolation scheme to improve the fine scale structure of the surface data employed in the model's initial data fields as well as producing a higher resolution terrain data base. Upon completion of these software modifications, a version of the Blackadar PBL was coded in scalar form for simplicity in the debugging process. Then, an initial data set was prepared for the 10 April 1979 AVE-SESAME case study. Three different 24 hour simulations were performed with the 58 km version of MASS 4.0. (This is the model version which contained the split-explicit time integration scheme.) The first (control) simulation employed a version of the model with the generalized similarity theory PBL and constant soil moisture everywhere within the domain. The second simulation differed only in the existence of the new Blackadar PBL as well as variable vertical resolution. Finally, the third simulation was identical to the second with the exception of variable soil moisture. The most striking differences were in the control simulation and the second simulation highlighting the differences in the PBL formulations.

The Blackadar PBL significantly enhances the accuracy of the simulation as can be diagnosed in a comparison with the the observations all of which are depicted in Figures 1 through 15. A review of the AVE-SESAME 2100 UTC surface, 2030 UTC 85 kPa, 2035 UTC radar, and severe weather observations clearly indicates the concentration of low-level convergence and vorticity just east of the dryline and south of the warm front over the western part of the Red River Valley separating Texas and Oklahoma. The two simulations indicate rather significant differences in

the surface heating and its subsequent effects on the mass and momentum fields in the Red River Valley and west Texas regions. The most dramatic differences at 2100 UTC can be seen in the region stretching from the Texas Panhandle to the Rio Grande River Valley. Here, surface temperatures are much lower in the control simulation, which utilizes the mixed-layer PBL than are observed in nature, with a rather marked cold bias when compared to the observations. The Blackadar simulation, on the other hand, produces consistently accurate point by point verification when compared to the observations as well as a much more coherent warm air advection pattern. For example, in the region between Midland and Lubbock, Texas the Blackadar PBL produces very accurate surface temperatures which are only 1-2 °C too warm while the control simulation is 4-6 °C too cool in the same region thus resulting in a diffuse and poorly organized pattern of low-level warm air advection in the control simulation. This, in turn, results in a less concentrated and accurate region of surface pressure falls in the control simulation which affects the low-level acceleration of the wind field. The patterns of mean sea level pressure, pressure tendency, 85 kPa height, model level 1 winds, and 85 kPa winds depicted in Figures 6 through10 indicate that the Blackadar simulation produces stronger convergence and a more accurate pattern of convergence when compared to the surface observations in Figure 1. This, in turn, produces more accurate vertical motion and mean relative humidity fields as diagnosed from the observed convection and severe weather reports. Figures 11 and 12 indicate that the Blackadar PBL produces a better positioning of the low-level convergence as inferred from the upward motion and regions of high relative humidity than does the control simulation employing the mixed-layer PBL. The vertical structure within the PBL (Figure 15) is also considerably better defined in the simulation employing the Blackadar PBL than it is the control when compared to soundings observed along or in the immediate proximity of the dryline (not shown).

Hence, the Blackadar PBL provided a more realistic simulation for the 10 April 1979 case study by producing significantly larger values of surface sensible heat flux which produced a more coherent pattern of low-level frontogenesis and surface pressure falls. This pressure fall pattern produced low-level winds which verified more accurately against surface observations. Apparently, the vertical flux of surface sensible heat is much larger with the Blackadar PBL thus making it a better formulation in regions where there is a deep nearly dry adiabatic boundary layer. One very interesting feature of the Blackadar PBL is its ability to

produce a nearly dry adiabatic layer and still allow substantial vertical wind shear as is often observed in major tornado outbreak case studies (Figure 15).

TASK ASSIGNMENT VI - PRODUCE DATA BASES FOR THE STEM II "ENGINEERING MODEL"

This task represented essentially a continuation of TASK ASSIGNMENT I as new data bases were prepared for use in both versions of the STEM II model. Data bases were prepared for two MADS case studies, i.e., the 3 May 1985 and the 4 April 1985 events. These data were interpolated from initial meteorological data used to run MASS 3.0. Unlike the previous STEM simulations, the 'engineering' version employed a coarse 50 km mesh length and only a single model layer of 40x30 grid points as well as simpler chemistry. These data sets were then written to magnetic tape and sent to the University of Iowa scientists involved in the MADS Project. Additionally a data set was prepared for the third MADS case study as was performed for the first two case studies and sent to the University of Iowa. This effort also involved providing University of Iowa scientists programming and systems information support for the NASA Langley computer system.

TASK ASSIGNMENT VIII - RUN TWO MASS MODEL SIMULATIONS FROM THE WASHINGTON D.C. FIELD EXPERIMENT

This task painfully dramatizes the difficulty of reconstructing complete data sets to initialize a mesoscale model for historical case studies from archived tapes. The two case studies to be simulated were the November 8 1986 (case study 1) and the March 28 1987 (case study 2) field experiment days. After producing a detailed inventory of the in-house data available for these two case studies data tapes were ordered from NOAA PROFS for use in MASS model initialization and for use in providing time-dependent model boundary conditions. The MASS model preprocessor was modified to employ asynoptic moisture data. The location, timing, and duration of the two nested grid simulations was planned. Also, verification data from NWS was compiled and archived for both case studies. Plotting software was modified for use in studying transport processes. The first data tapes received from NOAA PROFS indicated that the initialization data was incomplete, i.e., components of

the data fields which were ordered for case study 1 were actually never written to tape at PROFS. In addition to this, some of the data received from PROFS for the second case study was also missing or contaminated, i.e., written over with other, unknown, data files. Both case study data sets were then reordered from NCAR. The magnetic tape containing the two case studies was received from NCAR, however, it was determined that the tape was unreadable due to the presence of contaminated binary records which resulted in the return of the tape to NCAR and the ordering of a new one.

New data sets arrived from NCAR and were made compatible with the MASS model preprocessor format. The initialization data were then prepared for the model simulations. The MASS preprocessor was run utilizing data from 1200 UTC 7 November 1986. A noisy analysis was produced due to errors which were present in the data set received from NCAR. The errors had to be deleted and the preprocessor had to be executed again. Before executing the preprocessor again it was necessary to build a consistent data set above 300 mb where data was lacking from NCAR. The rebuilt data set in the model stratosphere was of concern to MESO scientists because it was very likely that it would cause unrealistic adjustments and contaminate the simulations. Thus, the inability to acquire data sets which were complete and error free from Federal meteorological archives made the completion of this simulation-based task technically unachievable.

TASK ASSIGNMENT IX - PRODUCE AXISYMMETRIC TASS MODEL STATISTICS ON NONSHEARING CUMULUS CLOUDS

In an effort to find a group of soundings which would provide a spectrum of convective clouds, daily soundings were processed and plotted for the period from 16 July 1980 to 31 July 1980. A group of thirteen soundings was selected for use in this task (as shown in Figure 16) and were then processed so that they could be input data to initialize the axisymmetric version of TASS. The soundings were selected by the EPA contract monitor for previously noted period from 0000 UTC rawinsonde reports over the southeastern U. S.. Before the simulations could be performed it was necessary to: (1) modify existing postprocessing code to plot time versus height cross sections of vertical velocity, (2) add code to TASS to calculate convective available potential energy (CAPE), and (3) perform several test simulations to determine which thermal bubble configuration consistently produced cloud formation

and realistic cloud structure. Figure 17 shows the differences in evolution for three different initial perturbations with either the radius and/or strength of the surface heat flux changed. By reducing the radius of the heat flux impulse while holding the magnitude constant at 1200 W/m^2 (compare Run36 to Run38), the cloud which forms has a lower cloud top and a weaker peak updraft. Alternately, reducing the magnitude of the surface flux while keeping the radius of the impulse constant at 2400m (compare Run36 to Run37) delays the formation of the cloud by roughly six minutes and also reduces the strength of the cloud. These effects are somewhat dependent on the sounding used (both the instability and the available moisture). Thirteen TASS cloud simulations were performed using the same surface heat flux (sensible heat only, no moisture flux) of 600 W m^{-2} over an area 2 km in radius. The resulting cells varied with peak development heights ranging from 3.5 to 14 km and with maximum vertical velocities from 7 to 34 ms^{-1}. For some of the cases, two clouds developed during the simulation and both were included in this study. Linear correlation coefficient statistics relating several different parameters were calculated, including CAPE values, maximum vertical velocity, cloud top height, cloud base vertical velocity, radar reflectivity, and cloud volume. Table 4 lists each case (A and B indicate two clouds), the cloud top height, the total CAPE from the sounding and the partial CAPE only calculated up the model cloud top. This CAPE is used in the following correlations.

Figures 18 - 23 depict the results of the study. Figure 18 depicts the linear correlation coefficient and line of best fit for CAPE versus the maximum updraft, cloud top height, and the radar reflectivity. The highest linear correlation is between the CAPE and W_{max} which is to be expected since the maximum vertical velocity predicted by parcel theory for an undiluted parcel of air is a direct function of the available buoyant energy. Figure 19 depicts the linear correlation coefficient and line of best fit between W_{max} and (1) cloud top height, (2) the height of W_{max}, and (3) radar reflectivity as well as the relationship between W_{max} height and cloud top. The highest correlation was between cloud top and W_{max} while the lowest, as in the previous figure, involved radar reflectivity. The added factors of sounding temperature and ice content probably caused the reduced direct correlation involving radar reflectivities. Figure 20 depicts correlation coefficients and curves of best fit between cloud volume and (1) cloud base mass flux, (2) W_{max}, (3) cloud base W, and (4)

mean cloud base mass flux. Interestingly, all four curves of best fit are a logarithmic rather than linear function. This represents a departure from the previous two figures. This logarithmic function indicates a relatively poor linear correlation in all but the W_{max} versus cloud volume correlation. Figure 21 correlates cloud top height with both total cloud base mass flux and mean cloud base mass flux. Compared to Figure 20 (the correlations with volume), there is more scatter and less of a clearly logarithmic pattern. From this study it is quite clear that there is a strong interdependence among available buoyant energy, cloud volume, W_{max}, and cloud top height. In the absence of large values of CAPE, cloud statistics are much more variable and are difficult to stereotype. Finally, Figure 22 depicts the composite W_{max} profiles for shallow, medium, and deep cloud systems. This figure further reinforces the concept of a high correlation between maximum vertical velocity and cloud top height. Figure 23 provides the evolution of the updrafts, downdrafts and visible cloud (the combination of the cloud water and reflectivity plots) for a small cumulus (23a-d), a moderate cloud (23e-h) and a deep cell (23i-l). The moderate cloud produces light rain which does not reach the ground, and the deep cell produces graupel in the upper levels and a heavy shower.

TASK ASSIGNMENT XI - STUDY CLOUD ENTRAINMENT USING INERT TRACERS IN THE THREE-DIMENSIONAL TASS MODEL

The three-dimensional version of the TASS cloud model was used in a series of simulations to better understand the dependence of cloud edge mixing or entrainment on the ambient wind shear. The first three cases were simulations of a small isolated cumulus cloud with no shear, light shear (maximum U velocity of 5 m/s) and moderate shear (maximum U velocity of 10 m/s), respectively. The fourth and fifth cases were simulations of a moderately towering cumulus cloud with light and moderate shear as previously defined. The initial environment for the small cumulus cases (cases 1-3) had a weak subsidence inversion at 2.5 km with a deep dry layer above 3 km (see Figure 24a for the model-smoothed sounding). The initial sounding used for the towering cumulus cases (cases 4-5) was much more unstable at all levels with a gradual decrease in moisture above 4 km (see Figure 24b). The u-components of the wind profiles are shown in Figure 25 for (a) cases 2-3 and (b) cases 4-5.

The time vs. height evolution of positive vertical velocity and cloud water for cases 1-3 is shown in Figure 26. The maximum updraft speed and the resulting cloud are both significantly weaker for the moderate shear case due to the increased mixing and dilution of the updraft. In Figure 27, the effect of the wind shear is clearly visible in the structure of the vertical velocity (W) and cloud water (XIC) at 24 min of simulation time.

The clouds simulated in cases 4 and 5 are much deeper than the first three cases with cloud tops reaching 7.2 and 6.8 km, respectively, as shown in the time/height plots in Figure 28. The effects of the wind shear are not as evident in the time/height evolution as they were for the smaller cumulus cases, although the visible structure of the cloud and the updraft are still noticeably altered by the shear as seen in the x-z slices (Figure 29). The four tracer fields were initialized in horizontal layers from 0-1.5 km, 1.5-3.5 km, 3.5-5.5 km and 5.5-9.0 km at a constant value of $100 g/m^3$. X-Z slices of the four tracer fields are shown in Figure 30 for cases 4 and 5 at 34 min. The upward vertical transport of the first two tracers within the updraft is evident as well as the sinking motion in the upper portions of the cloud due to negative buoyancy, which is transporting the upper tracers downward especially on the the downshear (right) side of the cloud. This downward transport increases with increasing shear, when comparing case 4 to case 5.

Figures 31 and 32 shows how the tracer mass integrated over the cloud volume evolves with time. Generally, the amount of tracer mass in the cloud is higher for the cases with stronger wind shear and also lags in time relative to the lower shear cases. This appears to be in part because the cases with higher shear tend to have larger cloud volumes due to increased mixing, even though they are generally weaker. Figures 33 and 34 show the time evolution of the percentage of each tracer relative to the total tracer in the cloud for all five cases. Initially, only the tracer 1 field (from below the cloud base) has advected upward into the cloud. As the cloud grows upward into the upper layers of tracer, these are continually entrained through the cloud edges and top. This is particularly evident in Figure 34a-b for the stronger cloud. Figure 35 shows both the total cloud base mass flux over the model domain (CBMF) and the CBMF only within the cloud. The model domain is 5.1x4.1 km for cases 1-3 and 8.2x7.0 km for cases 4-5. The in-cloud mass flux shows a slight increase for increasing shear at cloud base and also between the first three cases and the last two. The total CBMF is dramatically stronger for cases 4-5

which may be a function of the grid domain, but is also probably a function of the environment and the stronger clouds in cases 4 and 5. In Figure 36, the components of the CBMF (total and in-cloud only) are shown for all five cases. In all cases, the total and upward in-cloud flux are identical with almost no downward flux within the cloud at cloud base. The mass fluxes at cloud base are similar even as the shear increases for both the small and moderate cells. The differences between the small versus moderated clouds are much larger. One interesting feature is the mirror-image appearance of the upward and downward fluxes at cloud base for the three small clouds. For the two larger clouds (36d-e), the downward flux decreases to zero at cloud base as the cloud continues its upward growth and the compensating downdrafts at cloud edge also move upward.

SECTION IV - DETAILED DESCRIPTION AND RESULTS OF TASKS PERFORMED IN SUPPORT OF THE NASA/FAA WIND SHEAR PROGRAM

TASK ASSIGNMENT III -PRODUCE AXISYMMETRIC TASS SIMULATIONS OF THE DFW MICROBURST CASE STUDY

This task involved producing several very high resolution axisymmetric simulations employing initial data from the observed Stephenville, Texas sounding at 0000 UTC 3 August 1985 and a sounding generated from the MASS model preprocessor. The initial simulation experiments produced simulations with 10 and 40 meter resolutions over a 2x2 km (horizontal x vertical) area and 12 minutes of real time. The microburst was triggered by imposing a distribution of rain and hail at the 2 km model top. These initial simulations clearly showed the need for high resolution in defining the fine scale eddies which form within the roll vortex at the 8-9 minute period of the simulation. Additional simulations were then performed over a larger (4x4 km) domain. Much was learned about the dynamics of the gust front/roll vortex from these simulations. The speed of movement of the gust front/roll vortex proved to be independent of the grid mesh which was employed. On the other hand, the vertical structure of the gust front/roll vortex is highly dependent upon resolution with the complex eddy structure only resolved in the finest scale simulation. The structure of the simulated roll vortex did not differ significantly in the 2-dimensional simulations when compared to 3-dimensional simulations. Figures 37 through 42 illustrate the results of the 10 m grid mesh simulation for radar reflectivity (RRF), pressure perturbation (P), stream function (PSI), temperature deviation from the environment (TAU), the vertical wind component (W), and the radial wind component (U). For comparison, Figures 43 through 48 depict the same fields for the 40 m resolution simulation. These are displayed for the 7-9 minute period when the vortex roll near the ground rapidly develops. An overview of the comparison between the two simulations indicates that between 8 and 9 minutes the 10 m mesh simulation produces a much tighter roll vortex structure than the 40 m mesh simulation. In particular, the vertical component of motion (W), radial component of motion (U), and stream function fields (PSI), indicate the explosive interaction between the pressure force, momentum field, and surface frictional stresses in producing a complex set of very fine scale

eddies within the vortex itself. The results from these simulations were then closely compared to the flight data recorder information taken from the damaged Delta aircraft. The winds from both the simulations and the flight data recorder were compared. The results of this comparison are shown in Figure 49.

Additional numerical experiments performed under this task included a 20 meter resolution axisymmetric simulation which was integrated out to 14 minutes of real time. The dynamical fields were plotted at 30 second time intervals. MESO scientists closely analyzed the dynamics and structure of the ring vortex circulation associated with the gust front flow as well as the dynamics of vorticity production within the ring vortex. Figure 50 depicts the temperature deviation and winds from the 20 meter simulation. The analysis clearly related the concentration of vorticity in the ring vortex to the solenoid term in the vorticity equation.

TASK ASSIGNMENT IV -PRODUCE FIRST DRAFT OF JOURNAL ARTICLE ON MICROBURST SENSITIVITY STUDIES WITH THE AXISYMMETRIC TASS MODEL

This paper involved a series of detailed analyses of simulation experiments with soundings from the 30 June 1982 JAWS experiment and the 2 August 1985 DFW microburst (published as "Numerical Simulations of an Isolated Microburst. Part I: Dynamics and Structure", J. Atmos Sci., Vol. 45, 3137-3160). The primary purpose of the paper was to study the dynamics and structure of microbursts. In this section some of the most important findings from the simulation experiments will be described.

Two case studies of wet microbursts were simulated with the axisymmetric TASS model. The microbursts were simulated by specifying a distribution of precipitation at the top boundary of the model and allowing it to fall into the model domain. The mass loading, due to the weight of the precipitation, acted to initiate the development of a downdraft, which subsequently intensified by cooling due to microphysical processes. The spreading of the rain-cooled air near the surface produced strong outflow and large horizontal wind shear. In both case studies simulated hail was specified at the top boundary. The ambient environments of both cases were dry adiabatic from the surface to above 2 km AGL. There are several general conclusions which were reached as a result of the two simulation studies.

1) The simulated microbursts in the two cases were driven primarily by the cooling due to the evaporation of rain, and second, by the cooling due to the melting of hail; precipitation loading had only a weak impact in these simulations.

2) The simulations revealed a microburst ring vortex. The ring vortex first appeared a short distance above the leading edge of the descending precipitation shaft. The ring vortex propagated downward following the leading edge of the precipitation shaft and rapidly intensified as it neared the ground. Upon reaching the ground, the ring vortex circulation expanded outward following the leading edge of the cool outflow. The circulation of the ring vortex was centered within the upper portion of the cool outflow and extended into ambient air above the outflow. Stretching of the ring vortex vorticity was apparently opposed by the turbulent expansion of the ring vortex core.

3) The temperature departure from ambient was much greater near the ground than at higher levels within the downdraft. The relatively cold air near the ground was largely responsible for the sudden intensification of the ring vortex as it neared the ground.

4) The peak horizontal wind speeds occurred in association with the ring vortex. The peaks occurred in the lower portion of the ring vortex, where outflow speeds were enhanced by the circulation of the ring. The overall maximum outflow speed occurred as the ring vortex first reached the ground. After this time, the peak outflow speed slowly diminished in intensity and propagated with the ring vortex to larger radii.

5) In the two cases that were simulated, the outflow expanded with time and became a macroburst. A secondary, inner outflow peak formed adjacent to the downdraft, remained stationary and persisted with the downdraft. This inner peak was associated with a microburst outflow which was embedded within the expanding macroburst.

6) The time scale of the initial microburst was very short; lasting only several minutes. Peak outflow speed occurred about 4 minutes after

precipitation first reached the ground. The mean horizontal wind shear was greatest only two minutes after precipitation initially reached the ground, and decreased steadily as the microburst outflow expanded. Peak downdraft velocity and precipitation rates occurred at about the time of maximum horizontal wind shear.

7) The peak microburst downdraft speed occurred at 500-1000 m AGL. Below the peak, a pressure dome apparently acted to decelerate the downdraft and accelerate the radial flow outwards.

8) The depth of the outflow was roughly 500 m in these two case study simulations. Outflow depth within the burst-front head was deeper, but remained under 1 km. The maximum horizontal winds occurred within 80 m of the ground.

9) A nondimensional vertical profile taken from the 20 m resolution simulation of the DFW case matched those of a laboratory wall jet and a Doppler radar observation of a microburst. The half-velocity height was about four or five times greater than the height of the outflow peak.

10) The model results indicated that vertical profiles of horizontal wind may be different from a vertical profile of the maximum differential wind. The maximum differential wind profile typically indicated deeper outflow and in the latter stages of microburst development, a secondary upper peak.

11) The simulated burst-front structure was influenced by ground friction. Ground friction reduces the horizontal wind speed just above the ground and retards the propagation of the burst-front at the ground surface. Stronger winds aloft pushed the burst-front ahead of its surface position, producing an overhanging nose structure. This led to unstable overturning near the leading edge of the outflow. The propagation speed of the burst-front was considerably less than the peak horizontal wind speed behind the front.

12) The burst-front head contained strong upward and downward currents. The strongest upward motion was associated with the ring

vortex and was located within the relatively cool air behind the burst-front. The upcurrents acted to sweep cool surface air upwards to higher altitudes and, for this reason, the deepest region of cool air outside of the incipient precipitation area was found in the burst-front head. The advancing burst-front head forced warmer and more moist ambient air upward; some of this ambient air was then entrained into the outflow region behind the head.

Results from the two numerical simulations provide useful information which may be helpful in developing wind shear alert procedures. The primary findings of this paper concerning the interests of aviation are summarized below.

1) The results indicated a microburst lifetime of several minutes, making a timely alert for a particular microburst event very difficult.

Horizontal wind shear several minutes prior to peak intensity may be just above ambient, and severe low-level shear may last only several minutes before the microburst either dissipates or grows into a macroburst. Embedded microbursts, however, may exist for relatively long periods of time.

2) The simulations indicate that a pressure dome develops underneath the microburst downdraft, and forms prior to significant outflow winds. This suggests that a high resolution network of ground-level pressure sensors may provide one or two minutes warning time of a developing microburst.

3) A precipitation shaft with rain curling upward along its edges may provide a useful visual and radar indicator of an ongoing microburst. The upward curling rain would indicate a strong ring vortex circulation. The velocity field of the ring vortex may be detected by Doppler radars and used as an alert signature.

4) The model results supported by observations indicate a possible relationship between peak outflow speed and peak temperature drop. This relationship may prove valuable for microburst detection with infrared sensors.

TASK ASSIGNMENT VII - PRODUCE DATA TAPES, OUTPUT PLOTS, AND JOURNAL ARTICLES FROM TASS AXISYMMETRIC MICROBURST SIMULATIONS

As the title indicates this task represents a synthesis of many subtasks. One of these subtasks was initiated by a request made by NOAA of NASA to provide data on so-called 'pathological' microburst case studies. Five magnetic tapes were produced from data derived from the 2-dimensional DFW microburst simulation.

Another subtask involved further comparisons between the axisymmetric microburst simulation and the Delta flight data recorder for the DFW microburst case study. Examples of these comparisons can be seen depicted in Figures 49 and 51. In these figures comparisons between TASS and observed environmental temperature deviations and U and W wind components are shown. This work eventually resulted in a paper entitled, "A Relationship Between Peak Temperature Drop And Velocity Differential In A Microburst", which was submitted to the Third Conference on the Aviation Weather System (note Figure 52).

The third subtask which was performed during this task assignment involved production of the first draft of the second paper published in the Journal of Atmospheric Sciences (published as "Numerical Simulations Of An Isolated Microburst. Part II: Sensitivity Experiments", J. Atmos. Sci., Vol. 46, 2143-2165). This paper emphasized the sensitivity of microburst structure to a variety of environmental factors including : 1) the type, width, and intensity of precipitation, 2) the effects of a low-level inversion on microburst development, and 3) the effects of rotation. Listed below is a summary of the key findings and conclusions of this paper.

The two-dimensional axisymmetric TASS model was used to investigate the sensitivity of numerically-simulated isolated microbursts. The principle result was that a complex interaction of different factors may influence the existence as well as the intensity of microbursts. Microburst intensity is sensitive to : 1) the ambient temperature and humidity, 2) the horizontal width of the precipitation shaft or downdraft, 3) the magnitude of the precipitation loading, 4) the type of precipitation (i.e., rain, snow, hail, or graupel), and 5) the duration of the precipitation.

While the ambient environment and the horizontal scale of the downdraft or precipitation was found to have a dominant effect, the

simulated microbursts also exhibited significant sensitivity to the type of precipitation, as well as to the intensity and duration of the precipitation. Specific conclusions are listed below.

1) The potential intensity of wet microbursts are affected by the height of the melting level, the mean lapse rate below the melting level, and the ambient humidity levels through the melting layer. The intensity and likelihood of wet microbursts increase as the lapse rate becomes steeper, as the melting level becomes higher above the ground, and as the humidity becomes lower at the melting level and higher at low-levels.

2) With an increase in the diameter of the downdraft resulting from increasing width of precipitation shafts, the peak outflow speeds, the depth of the outflow, and the height of the outflow peak all increase, but the mean horizontal wind shear decreases. Peak downdraft velocity, on the other hand, is greatest for an optimal downdraft diameter of about 1 km.

3) An increase in mass loading of precipitation can increase the intensity of a microburst.

4) The duration of precipitation has little effect on the peak intensity if greater than several minutes, but weaker microbursts are produced by relatively short bursts of precipitation.

5) Ground-based stable layers act to reduce the intensity of the outflow and weaken the circulation of the ring vortex. They can increase the lifetime of the microburst by suppressing the expansion rate, preventing them from expanding to become macrobursts. They also can account for the sudden temperature increases from ambient which are sometimes observed within actual microbursts.

6) Notable sensitivity to precipitation type exists, and this sensitivity may change with environment. Snow and graupel are most effective in producing microbursts within typical dry microburst environments, but hail is more effective in producing wet microbursts within the more stable environments. The intensity of microbursts driven by rain only, ranks low relative to other

precipitation types. Snow is very effective in generating low-reflectivity microbursts within classical dry microburst environments. The structure of a snow-driven microburst is unique, with a relatively narrow stalactite-shaped radar echo, an intense downdraft, modest cooling, and strong shear. The ambient environment most suitable for this type of microburst contains a deep dry adiabatic layer extending well above the melting level, and nearly saturated conditions above the adiabatic layer.

7) The dynamical consequences of tangential rotation on microbursts were to weaken the low-level downdraft and outflow. Stronger rotation aloft reduces the pressure aloft, which weakens the acceleration of the downdraft due to the enhanced upward-directed pressure gradient force. Rotation at low-levels is diminished by the advection of angular momentum within the outflow.

8) Within many of the microburst simulations, peak temperature drop can be related to peak outflow speed. A relationship between these variables was found to be applicable to many of the wet microburst experiments. However, the relationship was not valid if a ground-based stable layer existed prior to the microburst, nor was it valid for snow-driven microbursts.

9) The ratio of ΔU to W_{min} (or U_{max} to W_{min}) was found to be quite sensitive to environmental conditions, radius of the downdraft, and precipitation type. Therefore, it may be difficult to estimate peak outflow speeds given only W_{min}, or vice-versa.

10) An index developed from simulations of wet microbursts with hail within nine different observed environments predicts a high wet microburst potential within environments having a high melting level, a steep lapse rate, relatively dry air at the melting level, and relatively moist air at low-levels.

Results from this study also indicate the importance of ice-phase microphysics and emphasizes the need for its inclusion in numerical cloud models, especially those used in the study of microbursts and downdraft interactions.

TASK ASSIGNMENT X - DEVELOP SOFTWARE FOR COMPUTING F-FACTORS FOR FLIGHT PATH TRAJECTORIES FROM AXISYMMETRIC TASS AND PRODUCE THREE-DIMENSIONAL TASS SENSITIVITY STUDIES

As was the case with an earlier task, this task represents a group of subtasks each of which involved a significant amount of work. The most important single subtask involved computing so-called F-factors from TASS simulations. The F-factor is a measure of the degree to which aircraft performance is compromised by horizontal and vertical motions along its flight path. It represents an index which reflects the potential hazard from microburst phenomena. A significant amount of software was written in an effort to calculate F-factors for simple flight paths and flight path trajectories at a given constant angle from axisymmetric TASS simulations of the DFW case study. Software was also written to contour the F-factor fields. F-factors were computed using the DFW 20 m simulation assuming simple flight trajectories. Color plots were produced to illustrate the spatial variations of the F-factor. In addition to the above, software was developed to compute the predictive F-factor based on range bin incremental cells and to compute normalized outflow velocities. In the latter the speeds are normalized by the maximum outflow velocity and the height coordinate is normalized by the height at which the outflow speed is one-half of the maximum.

An additional subtask involved producing axisymmetric model simulations for the 14 July 1982 Denver microburst. This observed sounding was modified by inserting a 500 meter deep isothermal layer. Output from a 25 m axisymmetric simulation for this case was written to 8 data tapes for subséquent analysis. These results were presented at the First Combined Manufacturers' and Technology Airborne Windshear Review meeting.

A great deal of effort was undertaken during this task assignment to develop and improve the 3-dimensional TASS model code. These improvements included: 1) increasing the flexibility of TASS software to specify the grid stretching to be employed in a given simulation, 2) adding a Rayleigh damping layer to the top 3 layers of the model, 3) adding software to combine a vapor pulse with a temperature pulse in the initial perturbation which is used to trigger convection in the model, 4) adding a collection efficiency for snow accreting cloud droplets based on potential flow theory, 5) changing the subgrid turbulence parameterization to

account for nonisotropic turbulence, 6) adding a subroutine to the model in order to produce a two-dimensional time vs. height plot of the area with a radar reflectivity greater than some threshold value, and 7) adding a prognostic equation for the number of hail particles, rather than assuming a hail distribution based on a constant intercept value. This last modification produced poorer results when tested than did the original formulation.

In addition to these subtasks, a significant amount of effort was expended analyzing 3-dimensional TASS simulation results. This included analyzing results from the MIST 20 July 1986 storm and the CCOPE 19 July 1981 storm. These simulation results were presented at the Second International Conference on Cloud Modeling in France. Data was acquired for use in simulating the July 1988 Denver microburst incident and preliminary experiments were performed. Papers were also presented at the recent AMS 15th Conference on Severe Local Storms and at a windshear meeting at NCAR concerning the 3-dimensional simulation of the DFW case study. A paper was also submitted to the International Aviation Meteorology Conference on the forecasting of wet microbursts using an index developed from simulation results. Also, a color movie of TASS model output for the DFW case study was made.

TASK ASSIGNMENT XII - PRODUCE HIGH RESOLUTION TASS SIMULATIONS OF MIST AND CCOPE CASE STUDIES

One of the first subtasks performed under task assignment XII involved completing two conference papers to be submitted to the 3rd International Conference on Aviation Meteorology. These papers dealt with the development of a wet microburst forecast index and the relationship between microburst temperature drop and outflow velocity. The index which can be expressed as :

$$\text{radial wind shear} = \left[\left(T_s-(5.5 \times 10^{-3}H_f)+\frac{Q_{v1000}-(Q_vH_f \times 1.5)}{3}\right) \times H_f\right]^{1/2}$$

where T_s is the surface temperature, H_f is the height of the freezing level, and Q_v is the water vapor mixing ratio employed here at the freezing level and at 1000 m above the surface. The microburst intensity description category is intense, severe, hazard, and caution for index values > 50, 46-50, 36-45, and 25-35 respectively.

Also developed during this task was software to calculate F-factors for simple flight paths in either the north-south or east-west directions from the 3-dimensional TASS simulation. F-factor fields were produced for the Denver July 88 and MIST 20 July 86 case studies.

An effort was made to improve the quality of the simulation of the Denver July 88 microburst by initializing the model with a sounding produced by the MASS model. A special sounding was observed at Denver at 2200 UTC or about 2 hours before the microburst event, but the sounding's representativeness of the environment two hours later was uncertain. The MASS model preprocessor had been employed previously to initialize TASS for the DFW case study and resulted in a significantly improved TASS simulation. In the DFW case study, the problem was spatial in that the accident occurred close to the 0000 UTC observation but the closest physical sounding was nearly 90 miles away from DFW at Stephenville, Texas. In the July 88 case study the problem was temporal and the MASS model simulation of the vertical atmospheric structure at DEN at 2200 UTC, which was initialized from observed data at 1200 UTC, did not accurately recreate the observed atmospheric structure. The performance of MASS was inadequate because it significantly underpredicted the depth of the dry adiabatic layer which preceded the intense microburst. Nevertheless, we were able to achieve a successful simulation of the Denver July 88 case with the TASS model using the observed 200 UTC sounding.

During this task assignment the journal articles were revised and put into final form for publication and the two conference papers were presented at the 3rd International Conference on Aviation Meteorology.

SECTION V - SUMMARY

The results of tasks performed during a three-year contract period have been described. The work performed under this contract was intended to support the Environmental Protection Agency and Department of Energy in the area of mesoscale acid deposition modeling studies and the Federal Aviation Administration and the National Aeronautics and Space Administration in the area of low-level convection-initiated wind shear modeling studies. In support of the mesoscale acid deposition study, work performed by MESO Inc. included : 1) the testing and optimization of a Sulphur Transport Eulerian Model (STEM), 2) the testing and modification of existing planetary boundary layer formulation codes, 3) the simulation and verification of complex transport and vertical mixing processes within the earth's planetary boundary layer employing the MASS model, and 4) the use of the TASS model to simulate the statistics of a spectrum of convective cloud systems including the sensitivity of clouds to environmental energy and the characteristics of lateral entrainment within cloud systems as a function of environmental factors. In support of the convection-initiated wind shear program, work performed by MESO Inc. included : 1) two and three-dimensional simulations of microburst case studies employing the TASS model, 2) indepth analyses of the characteristics of microbursts and their sensitivity to a wide range of environmental factors, 3) the generation of data bases for NASA and other Federal agencies which could be employed to study the potential low-level wind shear hazards associated with microbursts, 4) the calculation of aircraft performance indices based upon model-generated output fields, and 5) detailed technical publications of the science of microburst phenomena as determined from model simulations and aircraft-derived data sets.

The knowledge gained from these studies highlight the utility of numerical atmospheric simulation models in the solution of a wide variety of technical problems.

SECTION VI - REFERENCES

Binkowski, F., 1983: A simple model for the diurnal variation of the mixing depth and transport flow. *Bound. Layer Meteor.*, **27**, 217-236.

Blackadar, A. K., 1979: High resolution models of the planetary boundary layer. Advances in Environmental Science and Engineering. Vol. 1, Gordon and Breach, 50-85.

Blackadar, A. K., and H. Tennekes, 1968: Asymptotic similarity in neutral barotropic planetary boundary layers. J. Atmos. Sci., 25, 1015-1020.

Carmichael, G. R., and L. K. Peters, 1984: An eulerian transport/chemistry/removal model for SO2 and sulphate. I: Model development. *Atmos. Environ.*,**18**, 937.

Kaplan, M. L., J. W. Zack, V. C. Wong, and J. J. Tuccillo, 1982: Initial results from a Mesoscale Atmospheric Simulation System and comparisons with the AVE-SESAME I data set. *Mon. Wea. Rev.*,**110**, 1564-1590.

Kaplan, M. L., J. W. Zack, V. C. Wong, and G. D. Coats, 1984: The interactive role of subsynoptic scale jet streak and boundary layer processes in organizing an isolated convective complex. *Mon. Wea. Rev.*, **112**, 2212-2238.

Proctor, F. H., 1985: Numerical simulation of precipitation-induced downbursts. 2nd Intl. Conf. on the Aviation Weather System, Montreal, *Amer. Meteor. Soc.*, 291-298.

Proctor, F. H., 1986: Three-dimensional simulation of the 2 August CCOPE hailstorm with the Terminal Area Simulation System. WMO Tech. Document No. **139**, 227-240.

Proctor, F. H., 1987a: The Terminal Area Simulation System - Volume I: Theoretical Formulation. NASA CR-4046, DOT/FAA/PM-86/50,I,176 pp.

Proctor, F. H., 1987b: The Terminal Area Simulation System - Volume II: Verification Experiments. NASA CR-4047, DOT/FAA/PM-86/50,II, 112 pp.

Proctor, F. H., 1988: Numerical simulations of an isolated microburst. Part I: Dynamics and structure. *J. Atmos. Sci.*, **45**, 3137-3160.

Proctor, F. H., 1989: Numerical simulations of an isolated microburst. Part II: Sensitivity experiments. *J. Atmos. Sci.*, **46**, 2143-2165.

Yamada, T., 1976: On the similarity functions A, B, and C of the planetary boundary layer. *J. Atmos. Sci.*, **33**, 781-793.

Zack, J. W., and M. L. Kaplan, 1987: Numerical simulations of the subsynoptic features associated with the AVE-SESAME I case. Part I: The preconvective environment. *Mon. Wea. Rev.*, **115**, 2367-2394.

Zilitinkevich, S. S., 1975: Resistance laws and prediction equations for the depth of the planetary boundary layer. *J. Atmos. Sci.*, **32**, 741-752.

SECTION VII - TABLES

TABLE 1
CONTRACT TASK ASSIGNMENTS

TASK NO.	STARTING DATE	COMPLETION DATE	COST LIMITATION	LABOR EST.
1	8-06-86	12-15-86	$15,916	678 hours
2	8-06-86	12-15-86	$18,706	677 hours
3	10-01-86	2-10-87	$12,900	462 hours
4	11-05-86	3-01-87	$12,900	462 hours
5	4-01-87	7-31-87	$18,362	616 hours
6	4-01-87	7-31-87	$14,945	616 hours
7	4-01-87	10-1-87	$41,027	1359 hours
8	9-24-87	2-24-88	$18,800	580 hours
9	9-24-87	2-24-88	$ 7,321	250 hours
10	10-02-87	10-31-88	$89,319	2298 hours
11	9-15-88	7-15-89	$24,000	875 hours
12	4-01-88	2-28-89	$49,317	1672 hours

Table 2
Stem Timing Statistics

Module Name	Call Freq.	% Call Freq.	CPU Time	% CPU Time
ACCRET	47	0	.003	0
AQUPHA	377	0	.186	0
ASMM	47	0	.027	0
ASMX	47	0	.002	0
AUTOCO	47	0	.001	0
CBCTFL	47	0	.003	0
CLEAN	46	0	.129	0
CLOUDF	47	0	.002	0
COVER	12	0	.000	0
COVER1	47	0	.001	0
DECOMP	421	0	.015	0
DEPOS	47	0	.004	0
EQUIFN	91441	6	3.978	2
EVAPOR	47	0	.007	0
F	368	0	.005	0
FILTER	0	0	.000	0
FLUXV	658	0	.036	0
FREEZE	47	0	.007	0
HCOEX1	140	0	.022	0
HCOEX2	4760	0	.281	0
HCOEY1	140	0	.023	0
HCOEY2	4760	0	.282	0
HORX	2	0	.077	0
HORY	2	0	.072	0
INPUT	1	0	1.839	1
INPUT2	2	0	1.281	1
INTERP	47	0	.000	0
INTSOL	0	0	.000	0
LIQIC1	0	0	.000	0
LIQIC2	47	0	.119	0
LIQIP1	1444	0	.058	0
LIQRXN	134644	10	69.898	34 *
MATSO	820080	58	12.303	6
MELT	47	0	.000	0
PMDIRECT	1	0	.001	0
PRINT	46	0	8.480	4
RACOEF	0	0	2.137	1
RACOE1	646	0	.194	0
RADATN	23221	2	.442	0
RADSOL	0	0	.000	0
RAD1	0	0	.000	0
RAD2	0	0	.000	0
RAINF	47	0	.007	0
REACTN	23221	2	23.620	11 *
RIMING	47	0	.002	0

RXN	46	0	3.984	2
SION	92458	7	11.973	6
SNOWF	47	0	.003	0
SNOWR	23221	2	.167	0
SOLAR	47	0	.000	0
STEM2F	0	0	1.217	1
STORM	47	0	.001	0
SYMINIT	1	0	.065	0
TIMSET	141	0	.012	0
TOTALX	2	0	.001	0
TOTALY	2	0	.001	0
TOTALZ	4	0	.000	0
TOTAL0	4	0	.006	0
TOTAL1	1	0	.001	0
TOTAL2	2	0	.001	0
TRANS1	43201	3	29.896	14 *
TRANS2	24120	2	21.842	10 *
TRCOEF	141	0	.006	0
TRID	1598	0	.150	0
TRID1	63206	4	3.523	2
TRNSPT	47	0	.019	0
UDVEL	47	0	.000	0
VCOEF1	47	0	.025	0
VCOEF2	1598	0	.332	0
VCOEL1	141	0	.062	0
VCOEL2	53686	4	7.797	4
VERTCL	47	0	.004	0
VERTLQ	1	0	1.281	1
ZFILT	0	0	.000	0

* Key Subroutines

Table 3A

Blackadar Model Variables at Time = 2100 UTC 5-9-79 (9 Hrs)

K	Z	U	V	UG	VG	SPD	DIR	THETA	Q
2	5460	12.2	14.7	12.3	14.7	19.1	219.7	48.76	.48
3	4960	11.1	16.0	11.0	16.1	19.5	214.7	47.03	.15
4	4460	10.9	18.2	10.7	18.2	21.3	211.0	45.82	.16
5	4010	10.5	23.2	11.7	23.3	25.4	204.3	44.64	.60
6	3610	9.3	18.4	9.4	18.6	20.6	206.8	43.91	.79
7	3235	8.8	13.5	8.7	13.6	16.1	212.9	43.03	.89
8	2885	9.1	9.1	9.0	9.0	12.9	224.9	41.20	1.02
	**********	TOP OF THE PBL - 2802 METERS						**********	
9	2560	8.7	5.7	9.4	5.2	10.4	236.8	38.60	2.37
10	2260	7.4	3.5	8.5	1.9	8.2	244.5	37.69	5.16
11	1985	6.4	5.5	8.9	2.7	8.4	229.0	37.36	8.65
12	1735	4.4	9.3	9.7	7.7	10.3	205.3	37.24	11.12
13	1510	0.9	11.0	8.1	13.4	11.0	184.7	37.20	12.56
14	1310	-0.9	10.1	5.4	15.0	10.2	174.6	37.19	13.06
15	1135	-0.8	8.9	3.8	13.4	8.9	174.6	37.19	13.08
16	985	-0.4	8.3	3.5	12.1	8.3	177.2	37.19	13.01
17	835	0.0	8.0	3.5	11.1	8.0	179.8	37.19	12.92
18	685	0.2	7.7	3.1	10.3	7.7	181.6	37.19	12.84
19	560	0.4	7.4	2.7	9.7	7.4	183.0	37.19	12.79
20	460	0.5	7.1	2.2	9.3	7.1	183.9	37.19	12.75
21	360	0.6	6.9	1.8	8.9	6.9	184.8	37.19	12.71
22	260	0.7	6.7	1.3	8.5	6.7	185.8	37.19	12.68
23	160	0.7	6.5	0.8	8.2	6.5	186.5	37.19	12.64
24	60	0.8	6.3	0.3	7.9	6.3	187.2	37.19	12.61
25	5	1.3	6.4	0.0	7.7	6.6	191.4	38.16	11.76

Table 3B

Binkowski Model Variables at Time = 2100 UTC 5-9-79 (9 Hrs)

K	Z	U	V	UG	VG	SPD	DIR	THETA	Q
25	6210	13.5	12.1	13.3	11.9	18.1	228.1	49.14	.81
24	5710	12.2	14.7	12.3	14.7	19.1	219.7	48.79	.48
23	5210	11.1	16.0	11.0	16.1	19.5	214.6	47.04	.15
22	4710	10.7	18.3	10.7	18.2	21.2	210.3	45.75	.18
21	4210	7.7	20.3	11.7	23.3	21.7	200.8	43.79	.75
20	3810	8.9	17.7	9.4	18.6	19.8	206.6	43.53	.79
19	3410	10.2	14.8	8.7	13.6	17.9	214.6	43.15	.83
18	3060	11.2	11.4	9.0	9.0	16.0	224.7	42.52	.90
17	2710	10.1	5.8	9.4	5.2	11.6	240.2	40.37	1.27
16	2410	10.0	2.3	8.5	1.9	10.2	257.3	38.74	2.76
15	2110	10.4	6.7	8.9	2.7	12.4	237.3	36.47	6.94
14	1860	8.8	8.2	9.7	7.7	12.1	227.1	36.11	7.55
13	1610	7.0	9.5	8.1	13.4	11.8	216.7	35.70	8.22
12	1410	3.4	13.4	5.4	15.0	13.8	194.2	32.94	12.51
11	1210	0.0	11.3	3.8	13.4	11.3	180.1	30.94	15.14
	**********		TOP OF THE PBL			1153 METERS		**********	
10	1060	-0.2	10.8	3.5	12.1	10.8	179.1	30.80	15.36
9	910	-0.2	10.7	3.5	11.1	10.7	179.0	30.77	15.56
8	760	-0.2	10.6	3.1	10.3	10.6	179.0	30.76	15.56
7	610	-0.2	10.5	2.7	9.7	10.5	179.0	30.76	15.47
6	510	-0.2	10.5	2.2	9.3	10.5	179.1	30.76	15.33
5	410	-0.2	10.5	1.8	8.9	10.5	179.1	30.76	15.18
4	310	-0.2	10.4	1.3	8.5	10.4	179.2	30.77	15.02
3	210	-0.1	10.4	0.8	8.2	10.4	179.2	30.80	14.87
2	110	-0.1	10.4	0.3	7.9	10.4	179.2	30.92	14.77
1	10	-0.1	10.3	0.0	7.7	10.3	179.4	33.19	14.77

TABLE 4
2D CAPE VALUES FOR 18 CASES

CASE	CLOUD TOP (KM)	TOTAL CAPE (M^2/S^2)	CLOUD TOP CAPE (M^2/S^2)
82	12.7	789.0	789.3
83	3.5	684.5	73.3
83B	5.2	"	264.3
84	6.6	198.5	127.6
85A	3.5	1328.5	106.4
85B	6.0	"	442.7
86	8.2	1099.0	629.3
87A	4.5	376.7	107.2
87B	6.0	"	206.3
88A	3.7	231.9	0.
88B	3.6	"	0.
89	7.3	1346.1	842.0
90	14.0	531.8	531.8
92	7.5	1122.4	668.1
94A	3.5	1269.5	22.5
94B	4.0	"	46.8
95	5.4	280.5	69.7
96	3.4	0.	0.

SECTION VIII - FIGURES

1) Observed surface weather charts for (a) 1200 UTC, (b) 1500 UTC, (c) 1800 UTC, and (d) 2100 UTC 10 April 1979. Station observations are plotted in conventional SI units.

2) National Weather Service radar summaries for (a) 1435 UTC, (b) 1735 UTC, and (c) 2035 UTC 10 April 1979. Echo tops and bases are plotted in decameters.

3) Summary of severe weather reported between 1200 UTC 10 April 1979 and 0600 UTC 11 April 1979.

4) Observed 85 kPa heights (dm) and winds (ms^{-1}) for (a) 1130 UTC, (b) 1430 UTC, (c) 1730 UTC, and (d) 2030 UTC 10 April 1979. Solid lines are height contours in units of 30 dm. Dashed lines are isotachs at intervals of 2.5 ms^{-1}.

5) MASS 4.0 simulated surface temperature (°C) valid at 2100 UTC 10 April 1979 for the (a) mixed-layer PBL and the (b) Blackadar PBL model versions.

6) MASS 4.0 simulated altimeter setting (kPa x 10) and 100-50 kPa thickness (m) valid at 2100 UTC 10 April 1979 for the (a) mixed-layer PBL and the (b) Blackadar PBL model versions.

7) MASS 4.0 simulated altimeter setting tendency (x 10 kPa hr^{-1}) for the period from 1800-2100 UTC 10 April 1979 for the (a) mixed-layer PBL and the (b) Blackadar PBL model versions.

8) MASS 4.0 simulated model level 1 wind vectors and isotachs (ms^{-1}) valid at 2100 UTC 10 April 1979 for the (a) mixed-layer PBL and the (b) Blackadar PBL model versions.

9) MASS 4.0 simulated 85 kPa temperature (°C) and height (m) valid at 2100 UTC 10 April 1979 for the (a) mixed-layer PBL and the (b) Blackadar PBL model versions.

10) MASS 4.0 simulated 85 kPa level wind vectors and isotachs (ms^{-1}) valid at 2100 UTC 10 April 1979 for the (a) mixed-layer PBL and the (b) Blackadar PBL model versions.

11) MASS 4.0 simulated 70 kPa ω (x 10^{-4} kPa s^{-1}) valid at 2100 UTC 10 April 1979 for the (a) mixed-layer PBL and the (b) Blackadar PBL model versions.

12) MASS 4.0 simulated surface-50 kPa mean relative humidity (%) valid at 2100 UTC 10 April 1979 for the (a) mixed-layer PBL and the (b) Blackadar PBL model versions.

13) Observed positive buoyant energy (PBE) (jkg^{-1}) and negative buoyant energy (NBE) (jkg^{-1}) for a parcel originating at the level of maximum static energy valid at (a) 1130 UTC and (b) 1730 UTC 10 April 1979. Shading depicts area of PBE > 1000 jkg^{-1}.

14) MASS 4.0 simulated model lowest layer dewpoint (°C) valid at 2100 UTC 10 April 1979 for the (a) mixed-layer PBL and the (b) Blackadar PBL model versions.

15) MASS 4.0 simulated SKEW T - LOG P soundings valid at 2100 UTC 10 April 1979 for the (a) mixed-layer PBL and the (b) Blackadar PBL model versions.

16) Thirteen soundings used for the 2D axisymmetric cloud simulations.

17) Time vs. height plots of peak upward velocity in m s^{-1} (a-c) and peak cloud water content in g m^{-3} (d-f).

18) Linear correlation coefficient and line of best fit for TASS-simulated Convective Available Potential Energy (CAPE) (jkg^{-1}) versus the maximum updraft (ms^{-1}), cloud top height (m), and radar reflectivity (dBZ) for eighteen case studies.

19) Linear correlation coefficient and line of best fit for TASS-simulated maximum updraft (ms^{-1}) versus a) cloud top height (m), b) height of maximum updraft (m), and c) radar reflectivity (dBZ) as well as the

same for d) the height of the maximum updraft (m) versus cloud top height (m) for eighteen case studies.

20) Linear correlation coefficient and line of best fit for TASS-simulated cloud volume (m^3) versus a) cloud base mass flux (x 10^6 kgs^{-1}), b) maximum updraft (ms^{-1}), c) mean cloud base mass flux (kg m^{-2} s^{-1}), and d) cloud base W (ms^{-1}), for eighteen case studies.

21) Linear correlation coefficient and line of best fit for TASS-simulated cloud top height (km) versus a) cloud base mass flux (x 10^6 kg s^{-1}), and b) mean cloud base mass flux (kg m^{-2} s^{-1}), for eighteen cases.

22) Composite maximum vertical velocity (ms^{-1}) versus height (km) as simulated by TASS for a) shallow, b) medium, and c) deep cloud systems.

23) Examples of the time evolution versus height of (a) peak upward velocity (m/s), (b) peak cloud water content (g/m^3), (c) peak downward velocity (m/s), and (d) peak radar reflectivity (dBz) for a small cumulus (case 94). Time evolutions of the same four fields follow for a moderate cumulus (case 83) (e-h) and for deep convection (case 92) (i-l).

24) The two model-generated soundings used for (a) cases 1-3 and (b) cases 4-5.

25) The profile of the u-component of velocity (m/s) used for (a) cases 2 and 3, and (b) cases 4 and 5.

26) Time vs. height plots of positive vertical velocity (WMAX) for (a) case 1, (b) case 2 and (c) case 3 and cloud water mixing ratio (CWMAX) for (d) case 1, (e) case 2 and (f) case 3. WMAX is in m/s with a contour interval of 2 m/s, and CWMAX has a contour interval of 0.5 g/m^3.

27) X-Z slices through the cloud center (at 24 min) of vertical velocity (W) for (a) case 1, (b) case 2 and (c) case 3 and cloud water mixing ratio (XIC) for (d) case 1, (e) case 2, and (f) case 3. W has a contour interval of 2 m/s and XIC has a contour interval of 0.25 g/m^3.

28) Time vs. height plots of positive vertical velocity (WMAX) for (a) case 4 and (b) case 5 and cloud water mixing ratio (CWMAX) for (c) case 4 and (d) case 2. Units as in Figure 20.

29) X-Z slices through the cloud center (at 34 min) of vertical velocity (W) for (a) case 4 and (b) case 5 and cloud water mixing ratio (XIC) for (c) case 4 and (d) case 5. W has a contour interval of 2 m/s and XIC has a contour interval of 0.4 g/m^3.

30) X-Z slices through the cloud center of tracer fields 1-4 (TRC1-TRC4) for case 4 (a)-(d) and case 5 (e)-(h) at 34 min of simulation time. Contour interval is 10 g/m^3.

31) Mass totals of the tracer fields integrated over the cloud volume plotted against time for cases 1-3 (a)-(c). Units are in kg.

32) Mass totals of the tracer fields integrated over the cloud volume plotted against time for cases 4 (a) and 5 (b). Units are in kg.

33) The evolution over time of the percentage of each of the four integrated tracer fields relative to the total integrated tracer in the cloud for cases 1-3 (a-c).

34) The evolution over time of the percentage of each of the four integrated tracer fields relative to the total integrated tracer in the cloud for cases 4 and 5 (a-b).

35) The time evolution of (a) the total cloud base mass flux (kg/s) over the model domain for cases 1-5 and (b) the cloud base mass flux (kg/s) only within the cloud for cases 1-5.

36) The time evolution of the upward, downward and total components of the cloud base mass flux (kg/s) for cases 1-5 (a-e).

37) 10 m TASS axisymmetric radar reflectivity (dBZ) valid at a) 7, b) 8, and c) 9 minutes during the DFW microburst case study.

38) 10 m TASS axisymmetric pressure deviation (mb) valid at a) 7, b) 8,

and c) 9 minutes during the DFW microburst case study.

39) 10 m TASS axisymmetric stream function (s^{-1}) valid at a) 7, b) 8, and c) 9 minutes during the DFW microburst case study.

40) 10 m TASS axisymmetric temperature deviation (°C) valid at a) 7, b) 8, and c) 9 minutes during the DFW microburst case study.

41) 10 m TASS axisymmetric vertical velocity (ms^{-1}) valid at a) 7, b) 8, and c) 9 minutes during the DFW microburst case study.

42) 10 m TASS axisymmetric radial velocity (ms^{-1}) valid at a) 7, b) 8, and c) 9 minutes during the DFW microburst case study.

43) 40 m TASS axisymmetric radar reflectivity (dBZ) valid at a) 7, b) 8, and c) 9 minutes during the DFW microburst case study.

44) 40 m TASS axisymmetric pressure deviation (mb) valid at a) 7, b) 8, and c) 9 minutes during the DFW microburst case study.

45) 40 m TASS axisymmetric stream function (s^{-1}) valid at a) 7, b) 8, and c) 9 minutes during the DFW microburst case study.

46) 40 m TASS axisymmetric temperature deviation (°C) valid at a) 7, b) 8, and c) 9 minutes during the DFW microburst case study.

47) 40 m TASS axisymmetric vertical velocity (ms^{-1}) valid at a) 7, b) 8, and c) 9 minutes during the DFW microburst case study.

48) 40 m TASS axisymmetric radial velocity (ms^{-1}) valid at a) 7, b) 8, and c) 9 minutes during the DFW microburst case study.

49) Comparison of TASS-simulated vertical (W) and radial wind (U) components (ms^{-1}) versus the same observed fields derived from the Delta flight data recorder for a) 10.5 and b) 11 minutes during the DFW microburst case simulation.

50) Temperature deviation (°C) and winds (ms^{-1}) from the 20 m TASS axisymmetric simulation valid at a) 12, b) 12.5, c) 13, d) 13.5, and e) 14 minutes during the DFW microburst case simulation.

51) Comparisons between axisymmetric TASS-simulated temperature deviation (°C) and observed temperature deviation (°C) from the Delta flight data recorder for a) 10.5 and b) 11 minutes during the DFW microburst case simulation.

52) A TASS-derived relationship between maximum radial velocity (ms^{-1}) and temperature drop (°C) accompanying microbursts.

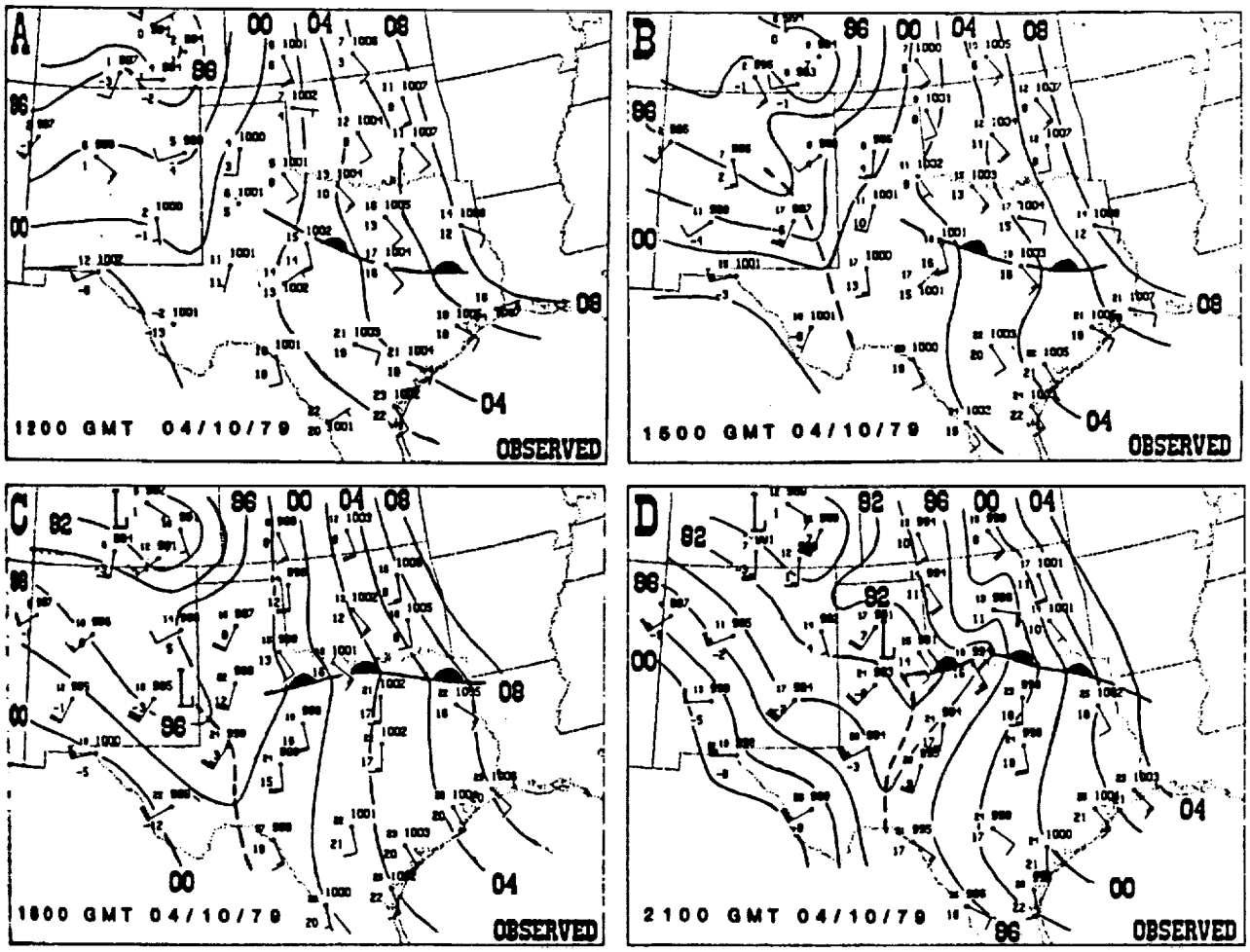
A
1200 GMT 04/10/79
OBSERVED
B
1500 GMT 04/10/79
OBSERVED
C
1800 GMT 04/10/79
OBSERVED
D
2100 GMT 04/10/79
OBSERVED

FIGURE 1

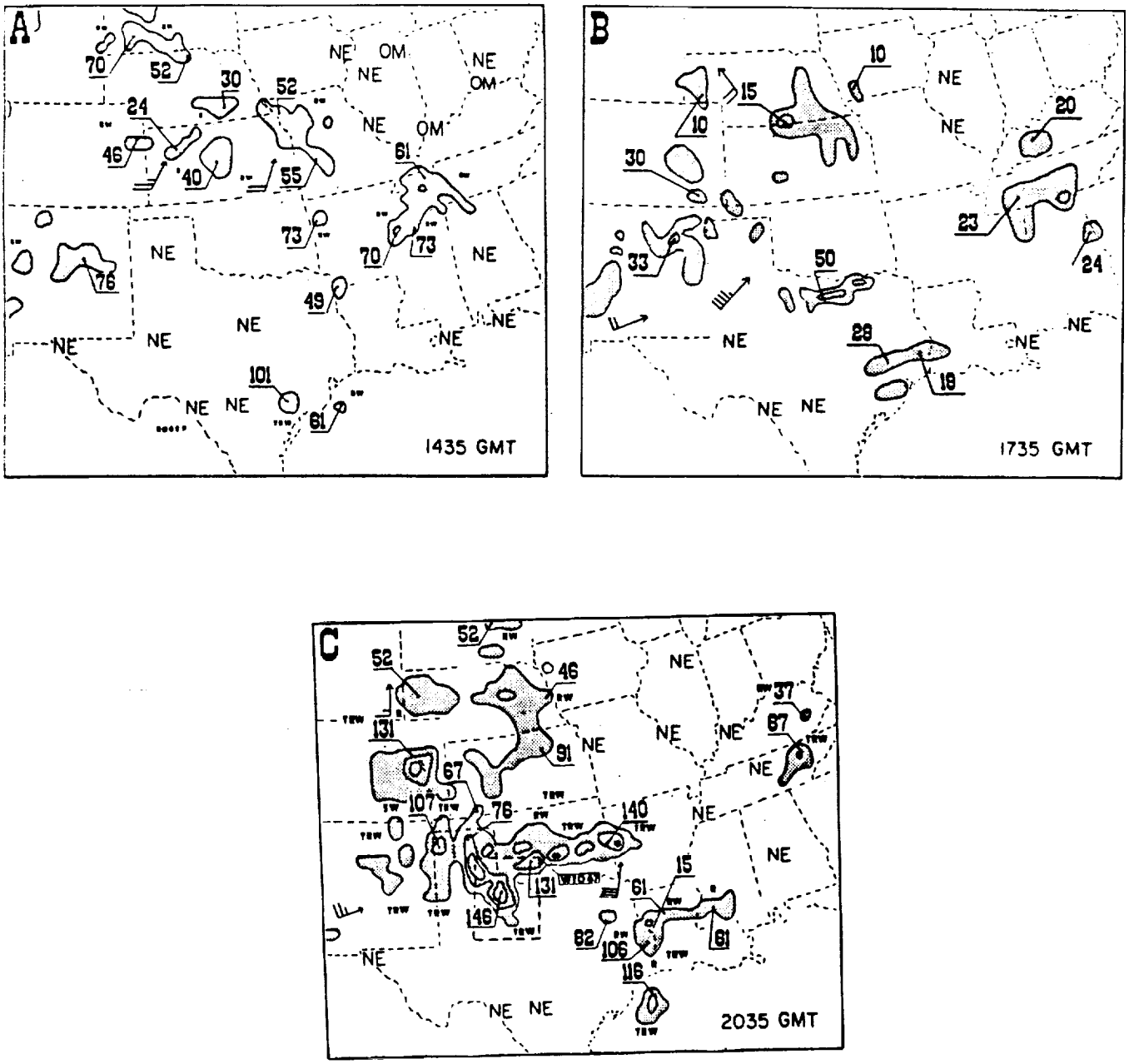

FIGURE 2

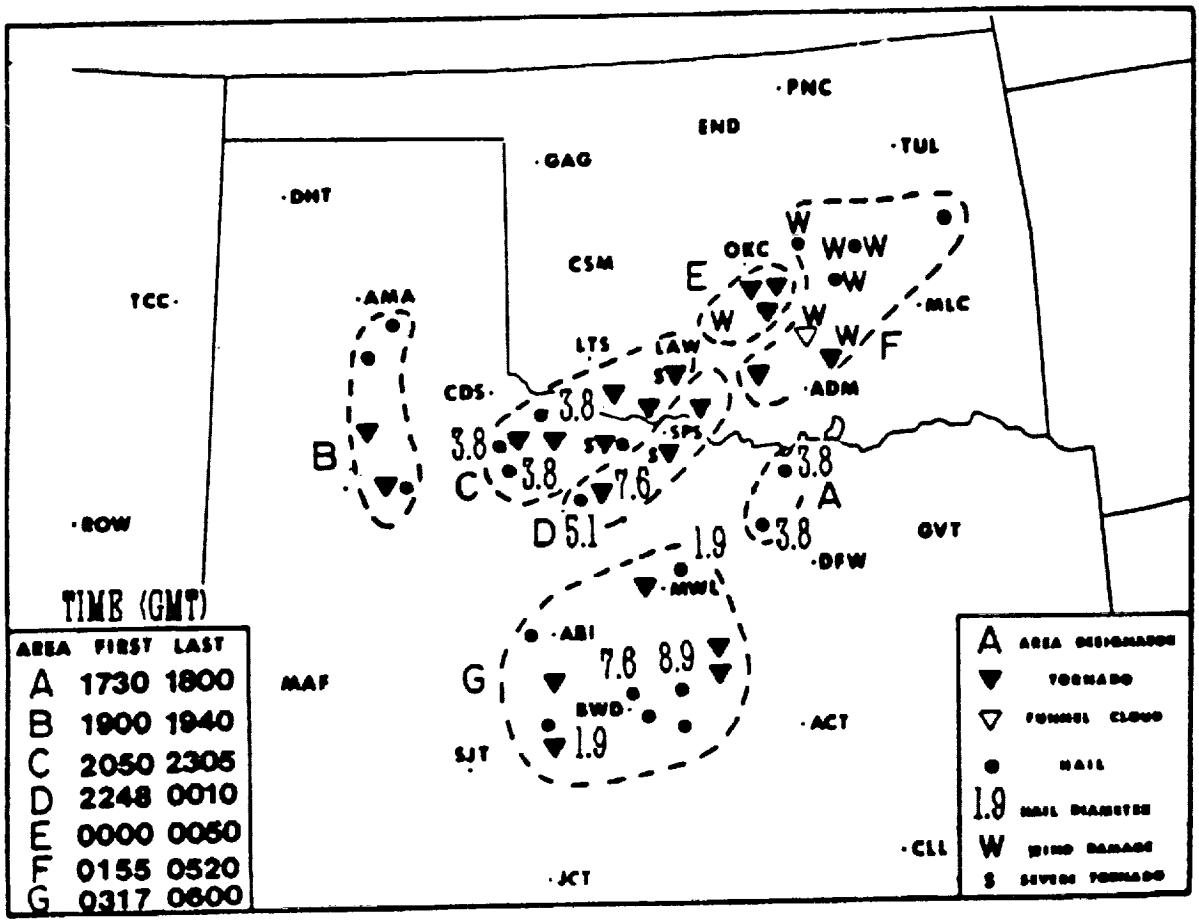
PNC
END
TUL
GAG
DHT
CSM
OKC
MLC
TCC
AMA
LTS
LAW
ADM
CDS
SPS
ROW
MAF
ABI
BWD
SJT
ACT
DFW
GVT
CLL
JCT
A
B
C
D
E
F
G
3.8
7.6
5.1
1.9
8.9
TIME (GMT)
AREA FIRST LAST
A 1730 1800
B 1900 1940
C 2050 2305
D 2248 0010
E 0000 0050
F 0155 0520
G 0317 0600

FIGURE 3

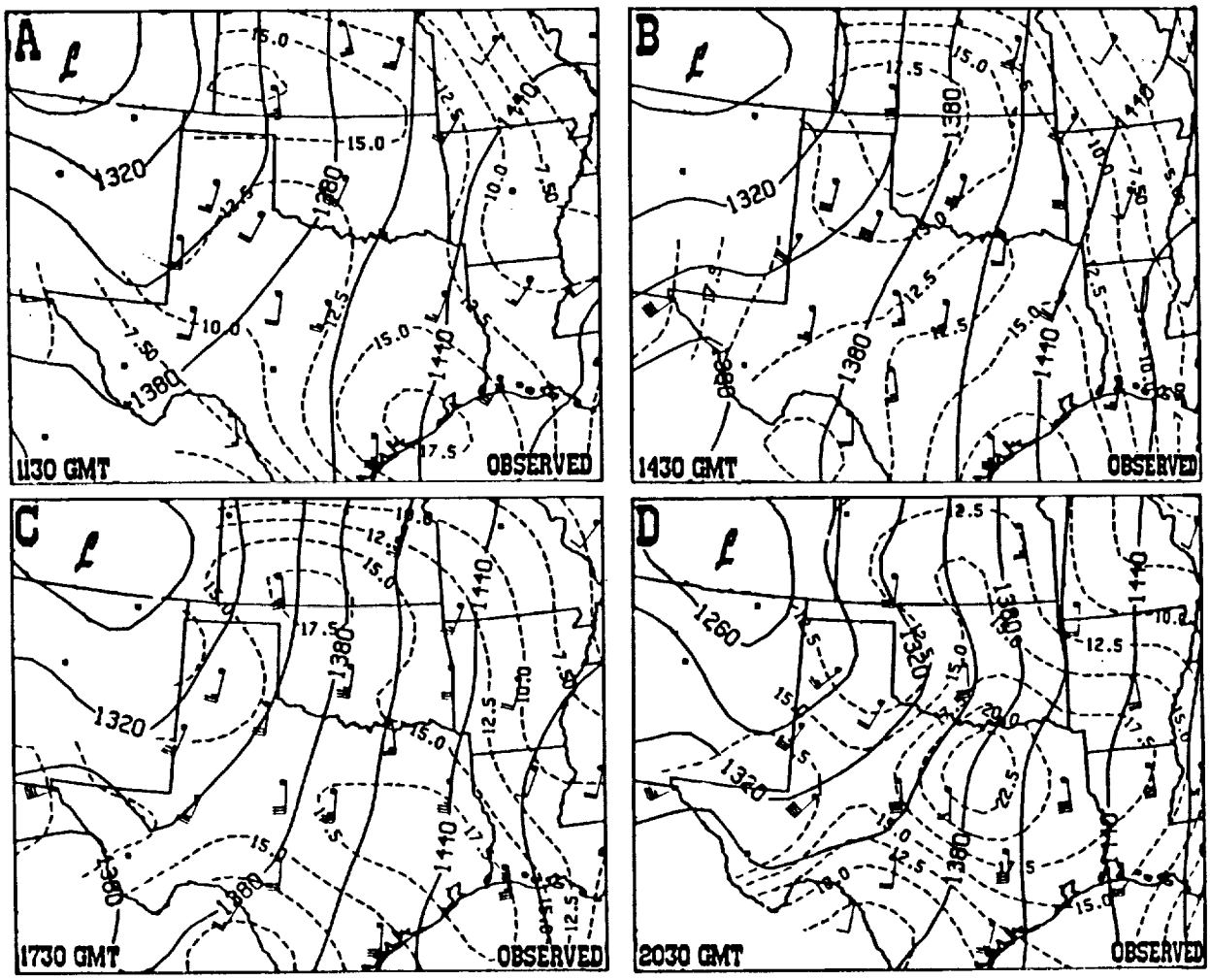
A
1130 GMT
OBSERVED
B
1430 GMT
OBSERVED
C
1730 GMT
OBSERVED
D
2030 GMT
OBSERVED

FIGURE 4

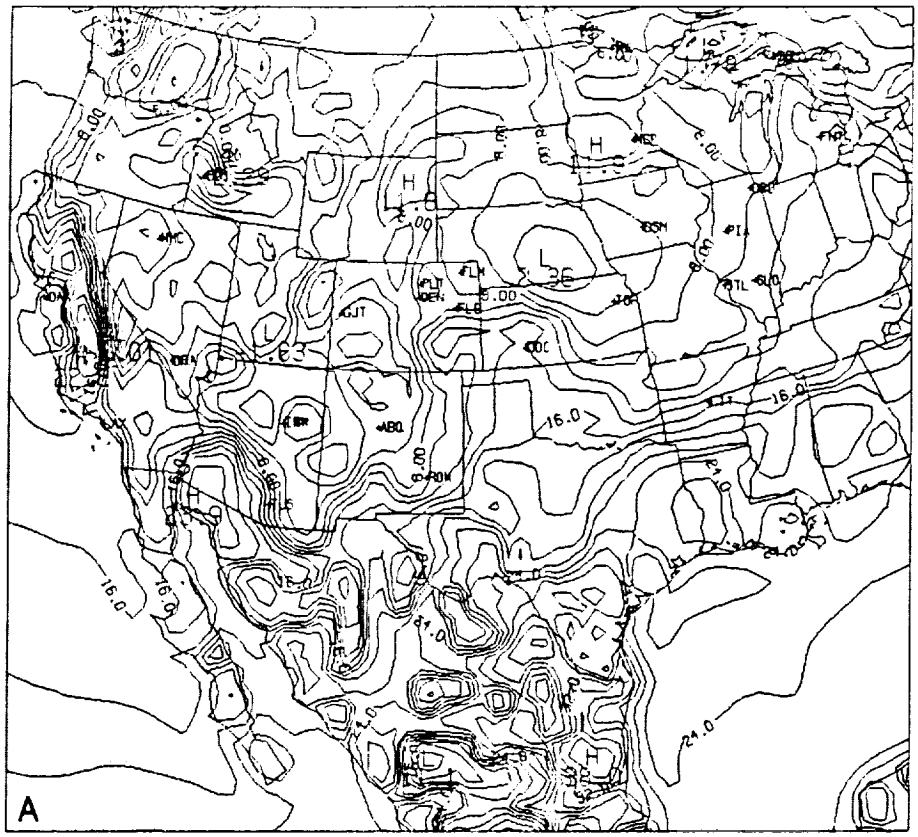

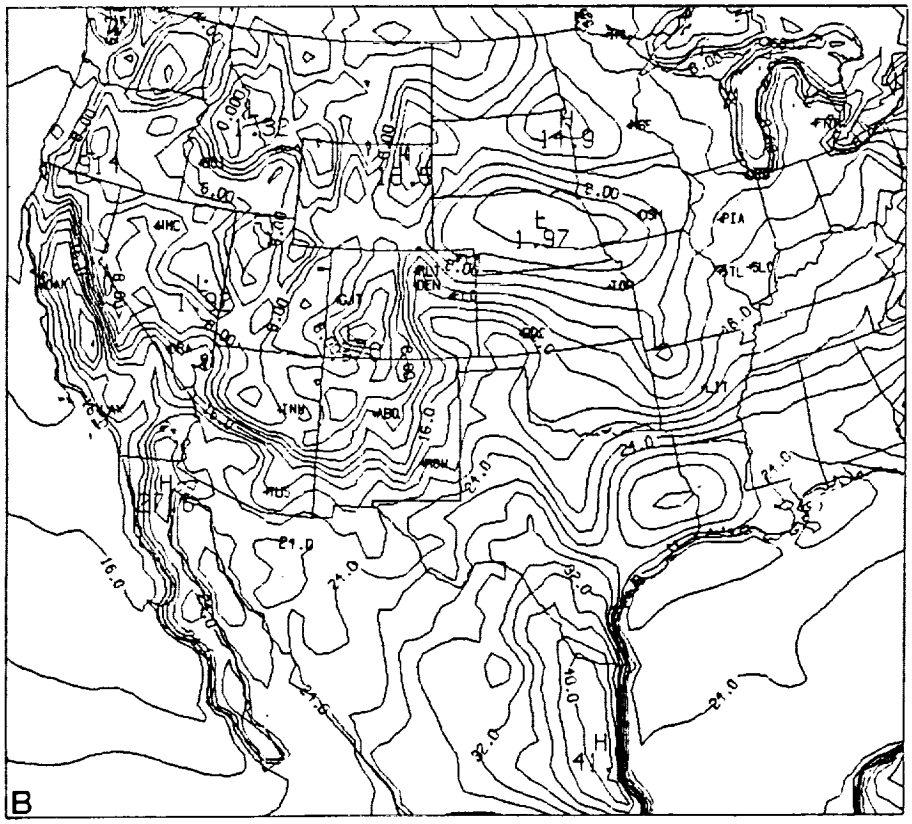

FIGURE 5

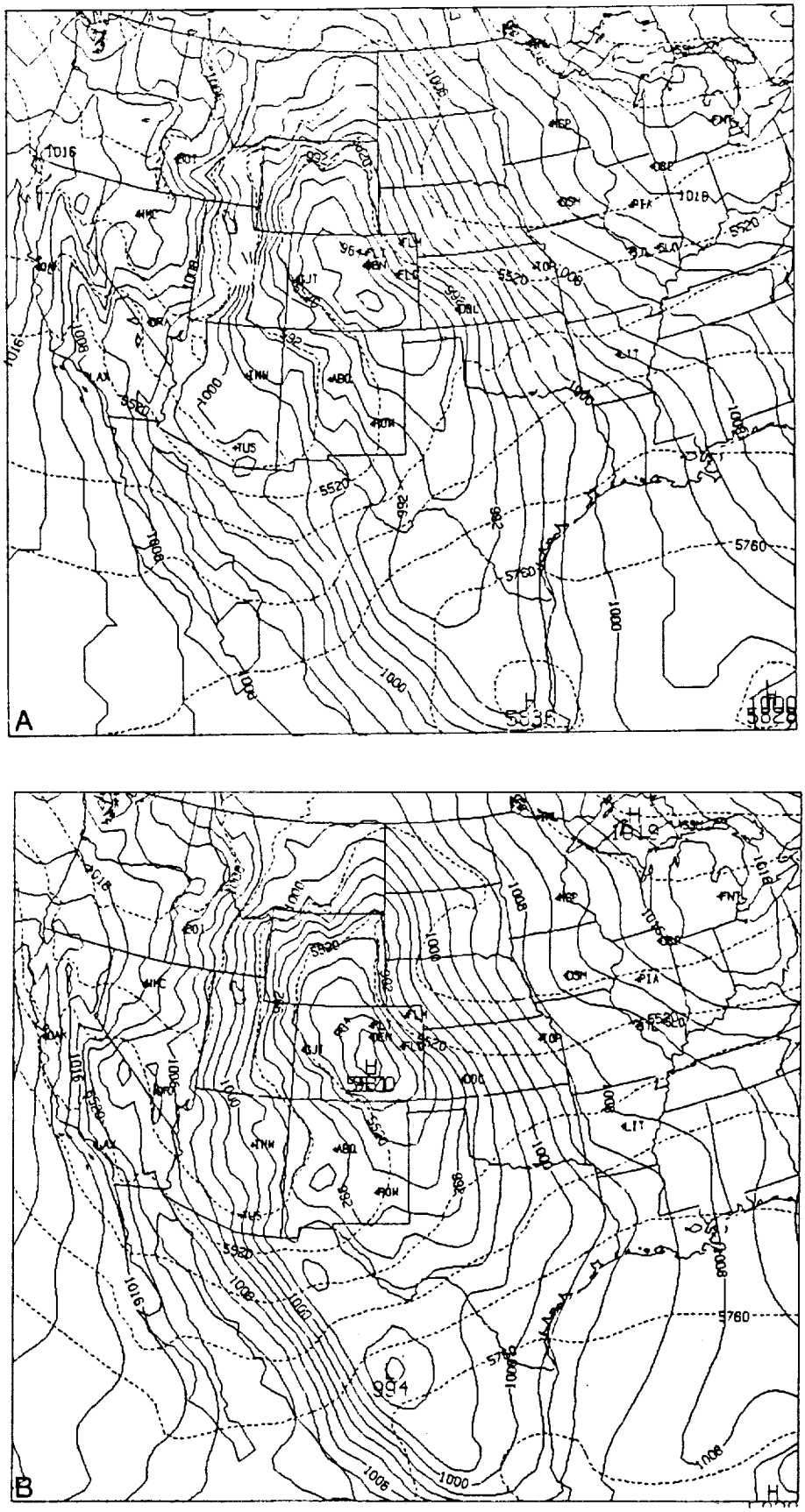

FIGURE 6

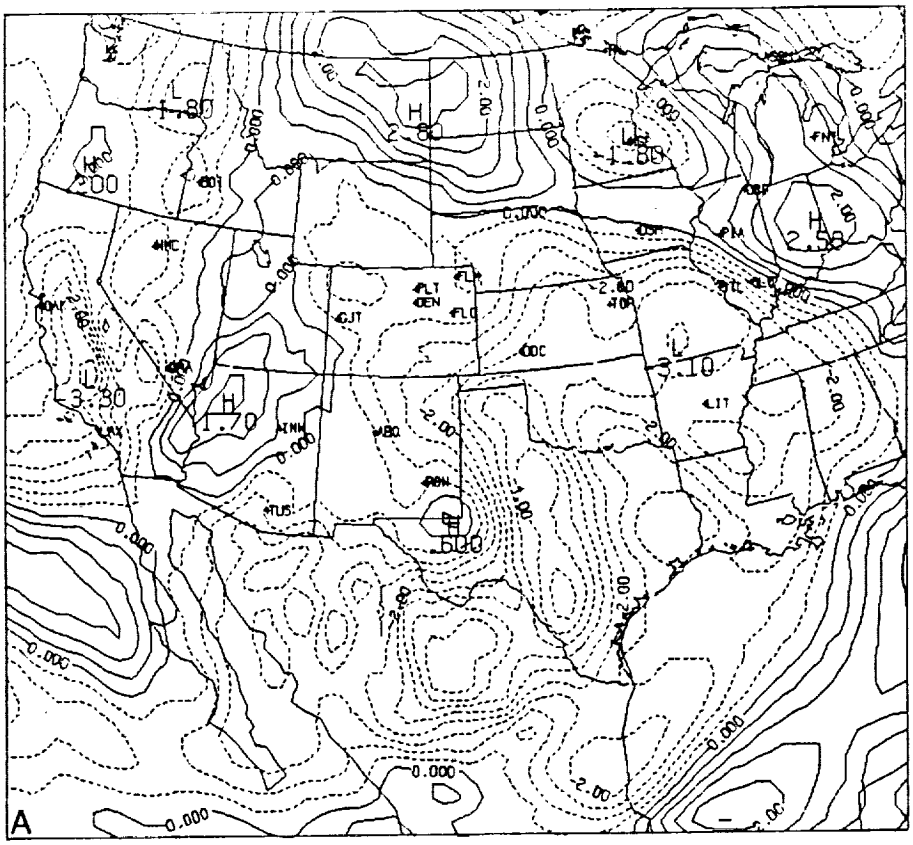
A
L
1.80
H
2.00
-3.80
H
1.70
L
-3.10
H
2.58
H
2.00
0.000

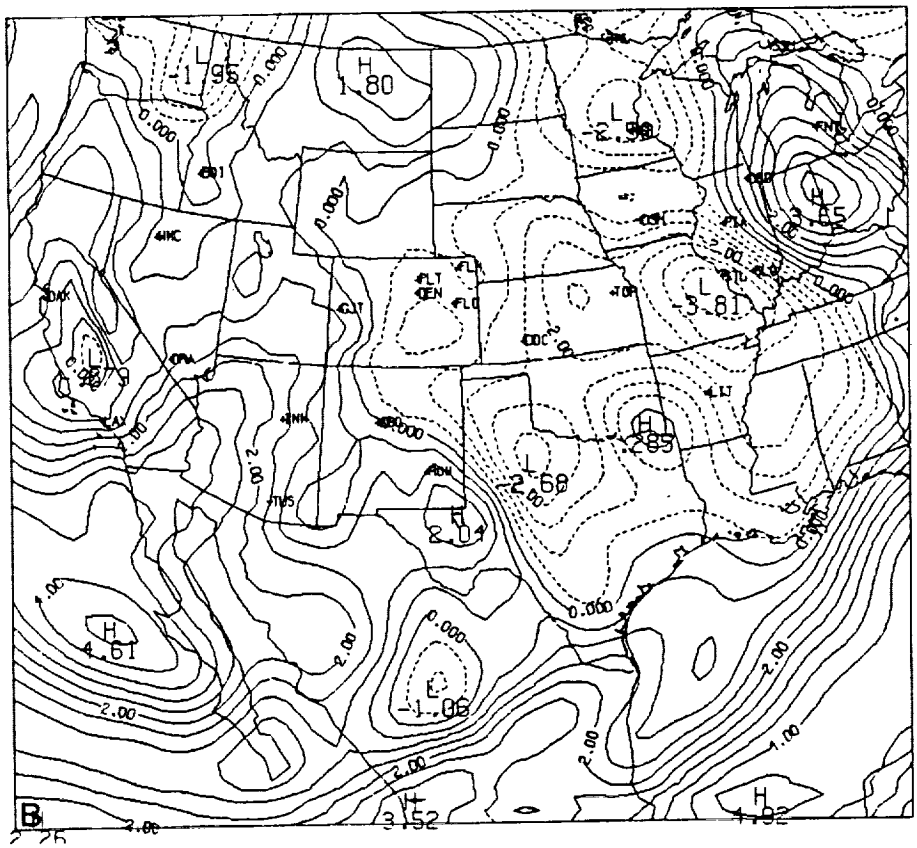
B
-1.95
H
1.80
L
-3.81
H
2.85
L
-2.68
H
2.04
H
4.61
L
-1.08
H
3.52
H
4.82
0.000
2.00

FIGURE 7

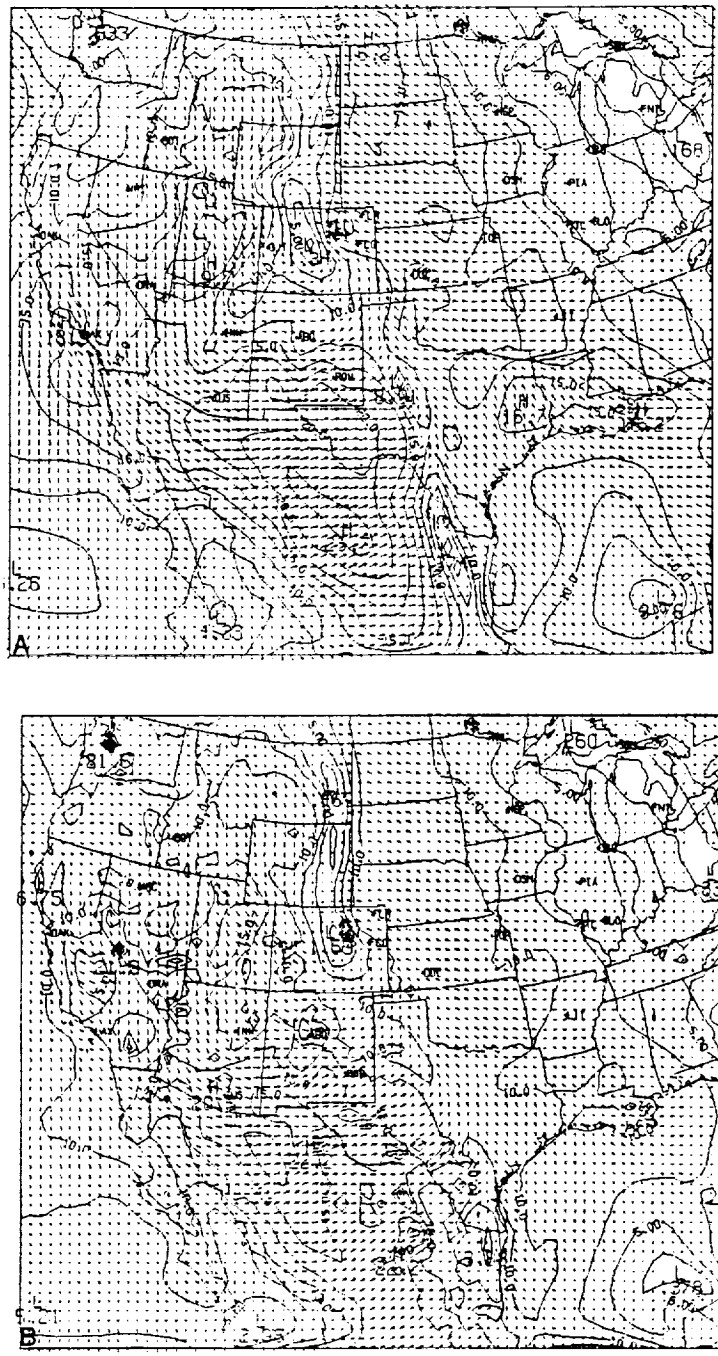

FIGURE 8

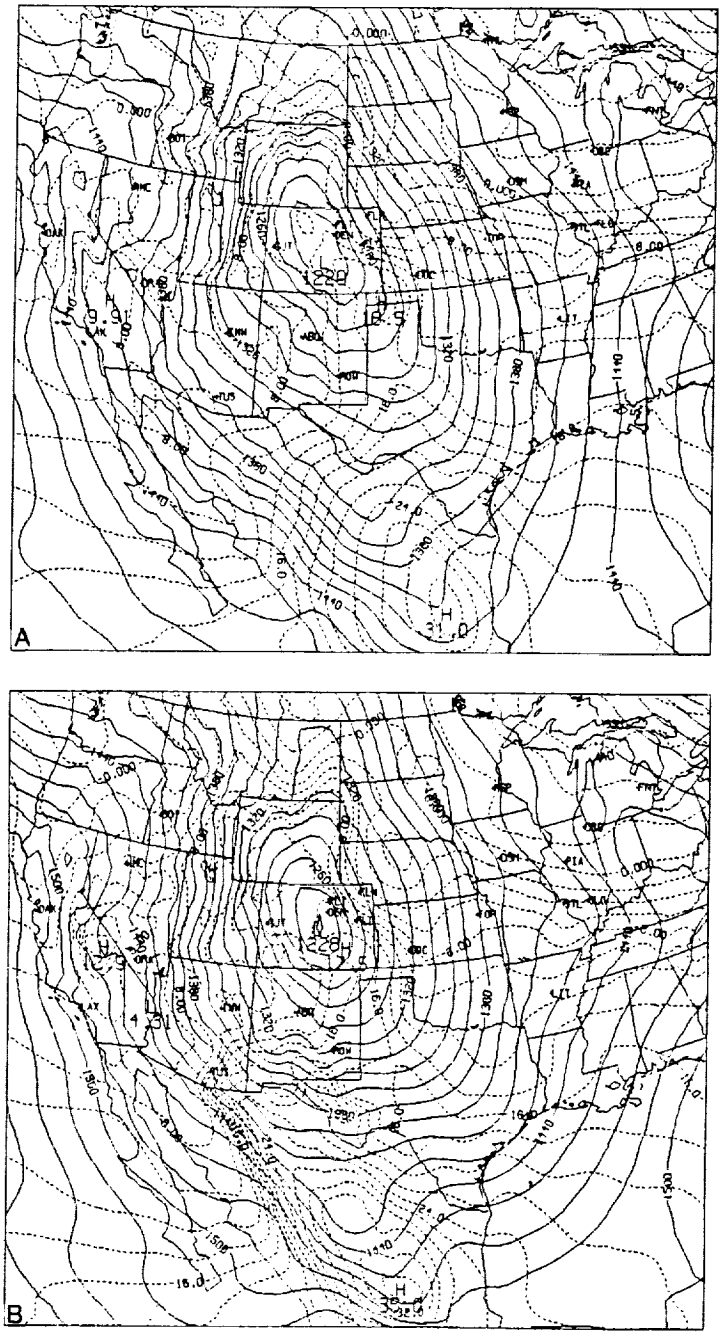

FIGURE 9

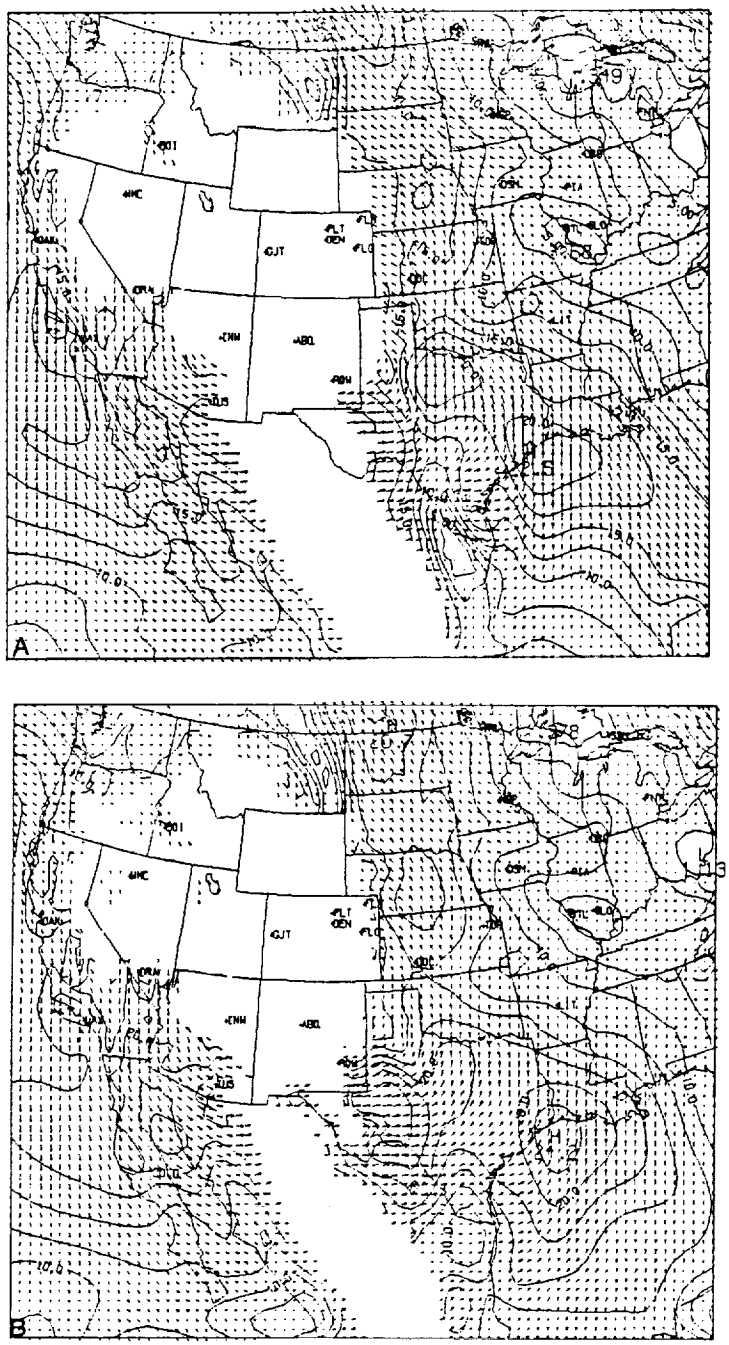

FIGURE 10

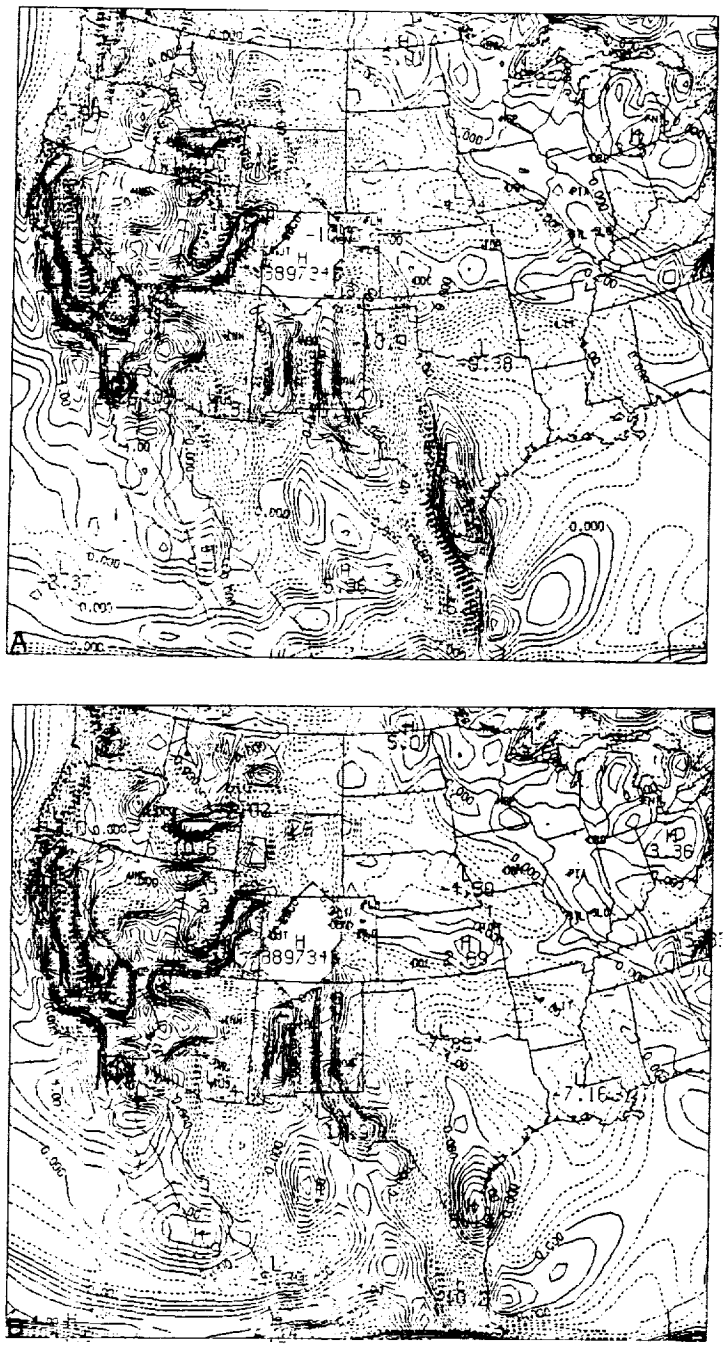

FiGURE 11

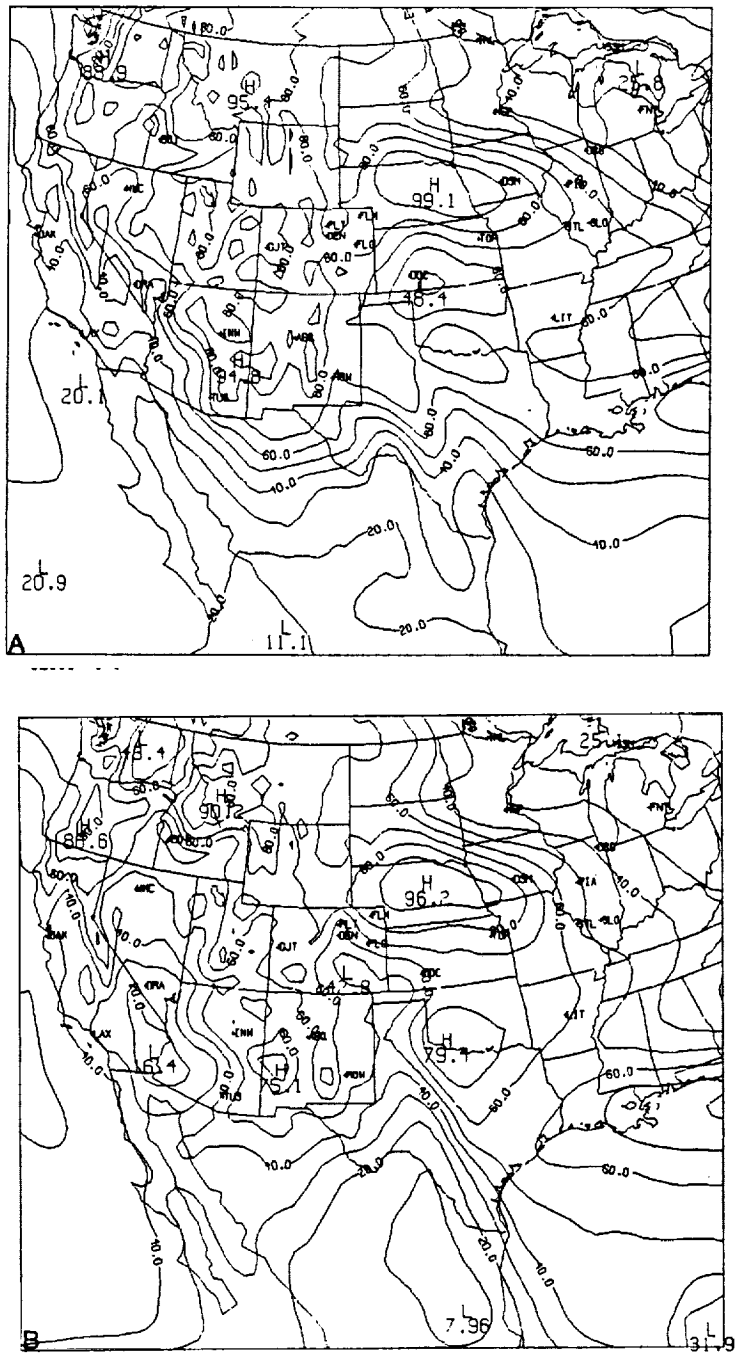

FIGURE 12

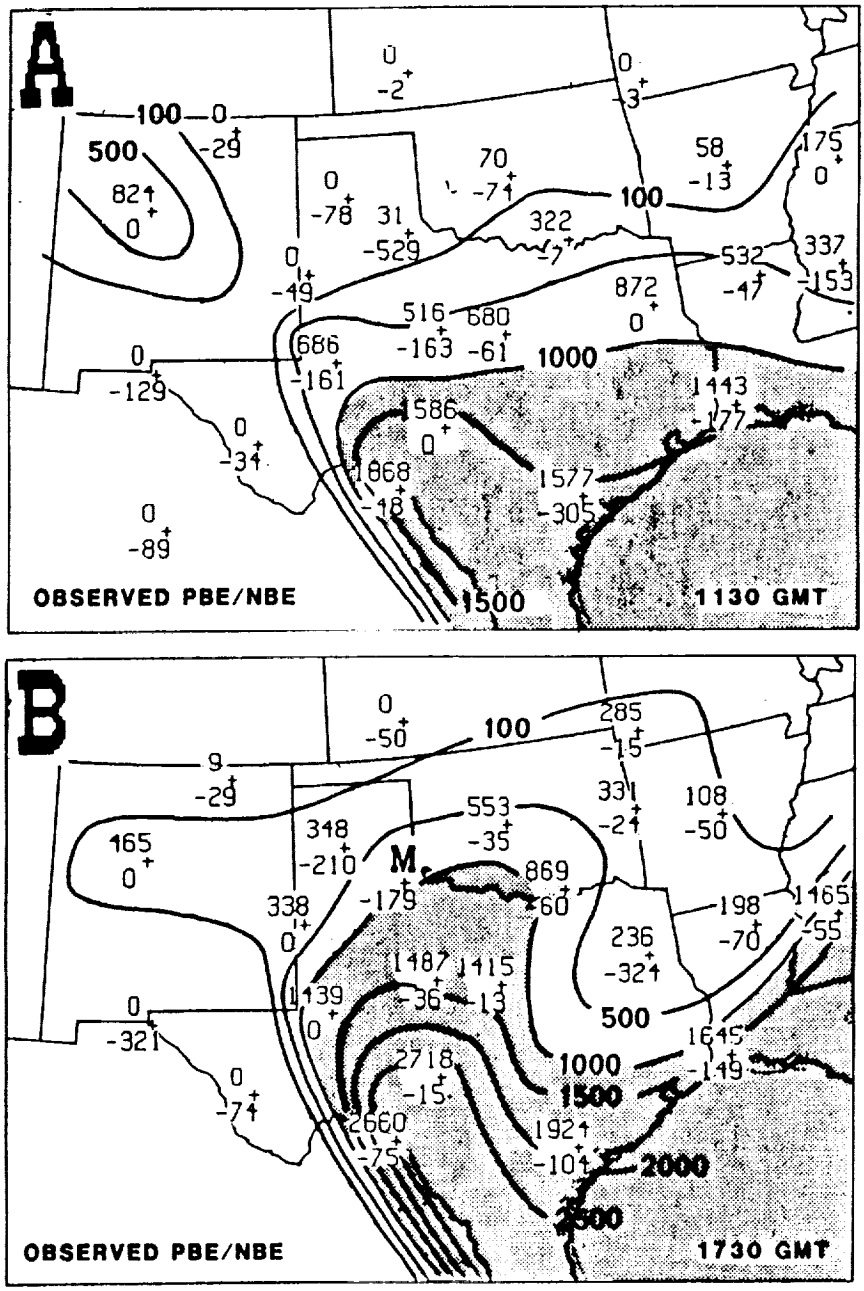
A
100
500
1000
1500
OBSERVED PBE/NBE
1130 GMT
B
100
500
1000
1500
2000
2500
OBSERVED PBE/NBE
1730 GMT

FIGURE 13

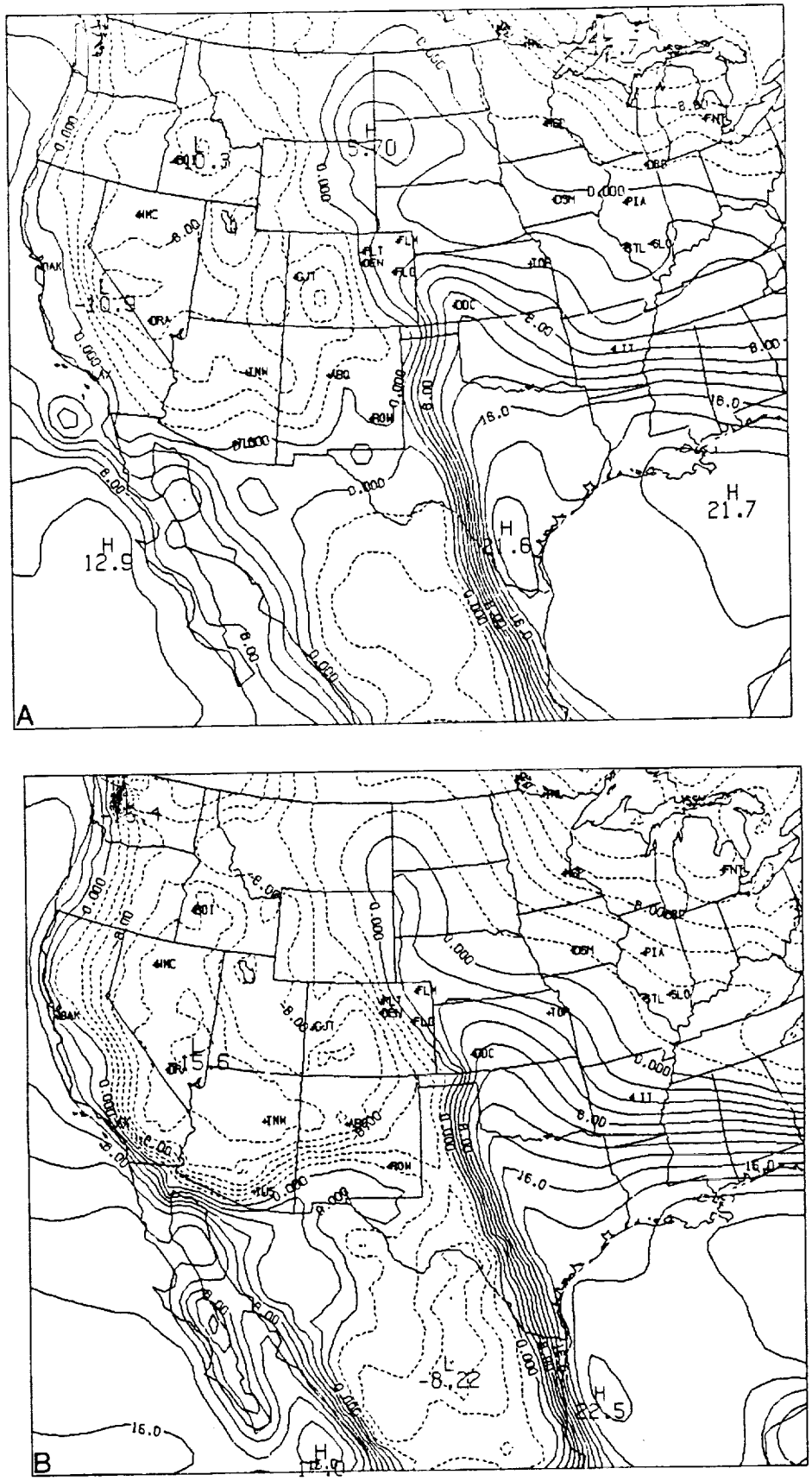

FIGURE 14

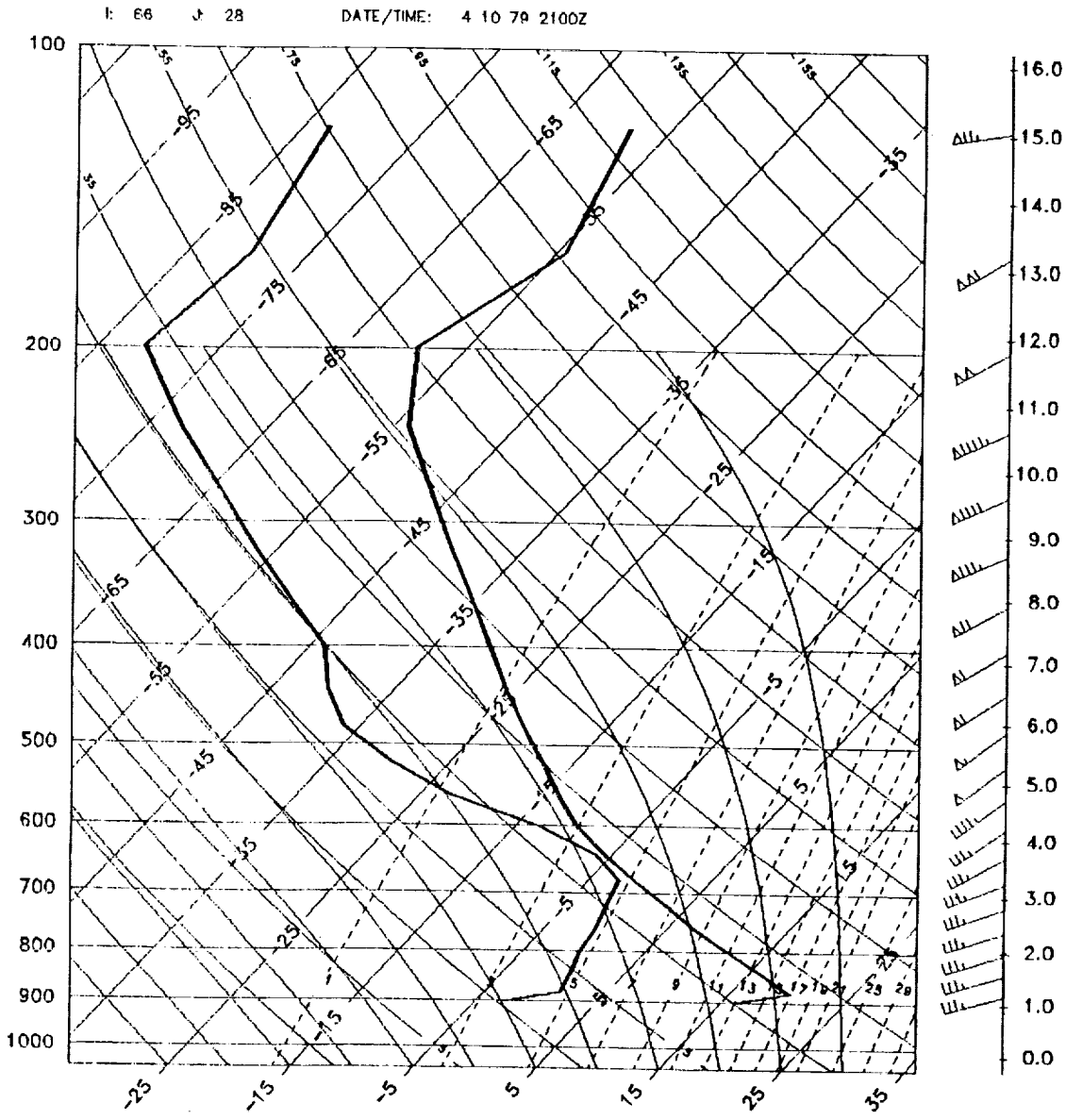
I: 66 J: 28 DATE/TIME: 4 10 79 2100Z
100
200
300
400
500
600
700
800
900
1000
-25
-15
-5
5
15
25
35
16.0
15.0
14.0
13.0
12.0
11.0
10.0
9.0
8.0
7.0
6.0
5.0
4.0
3.0
2.0
1.0
0.0

FIGURE 15A

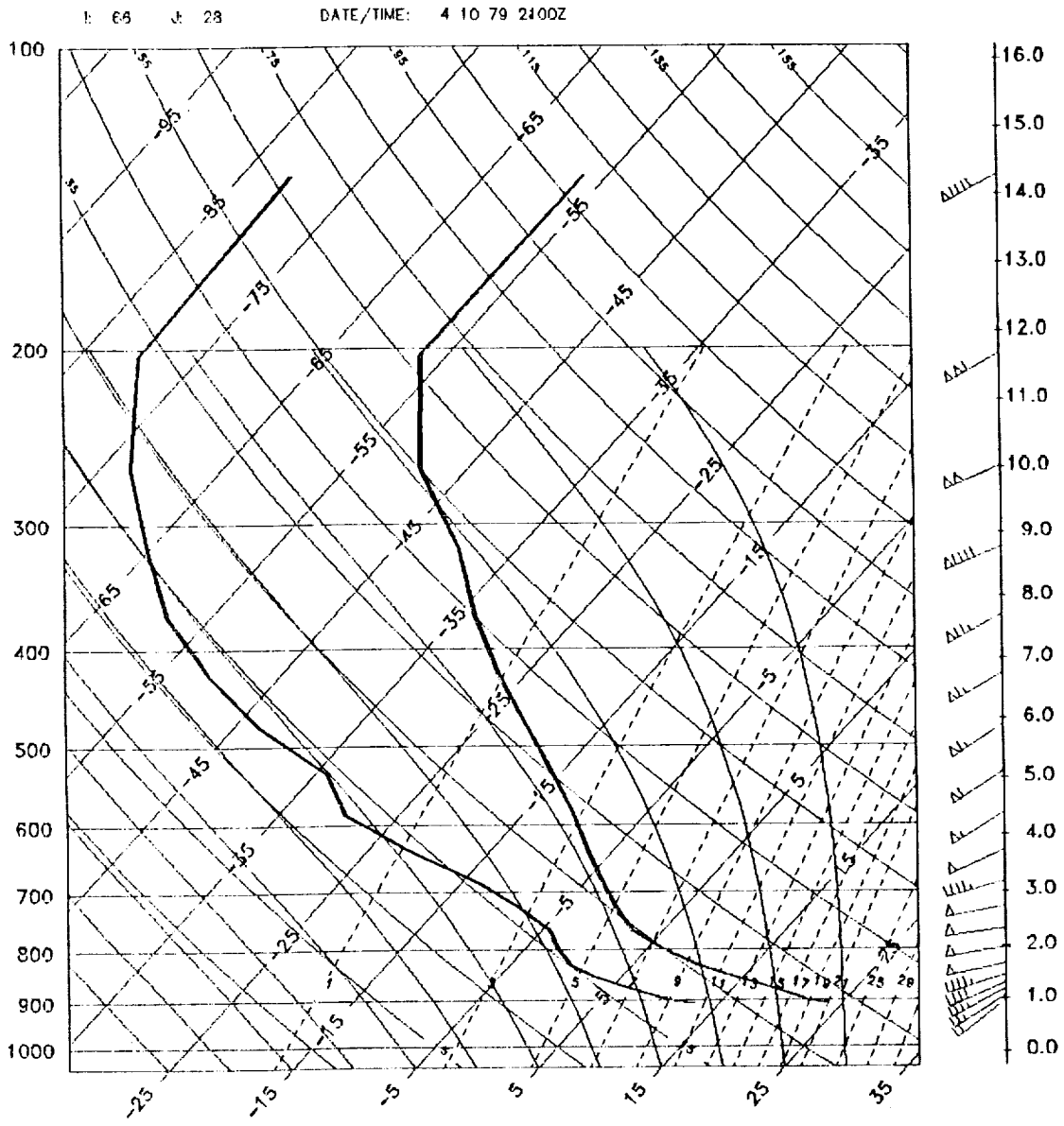
I: 66 J: 28
DATE/TIME: 4 10 79 2400Z
100
200
300
400
500
600
700
800
900
1000
-25
-15
-5
5
15
25
35
16.0
15.0
14.0
13.0
12.0
11.0
10.0
9.0
8.0
7.0
6.0
5.0
4.0
3.0
2.0
1.0
0.0

FIGURE 15B

CASE 82 CAPE=789

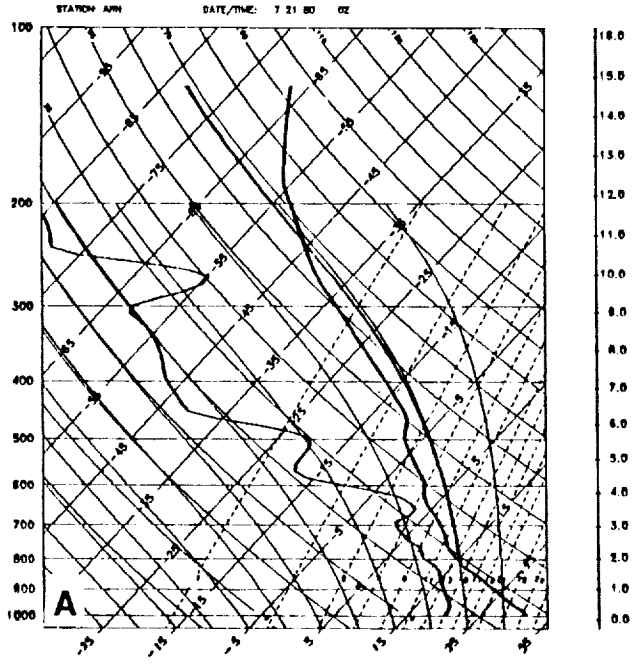

CASE 83 CAPE=685

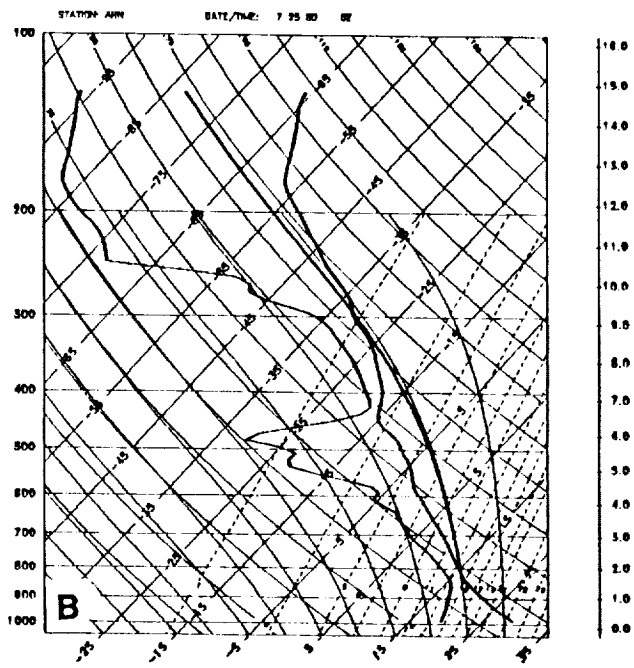

CASE 84 CAPE=199

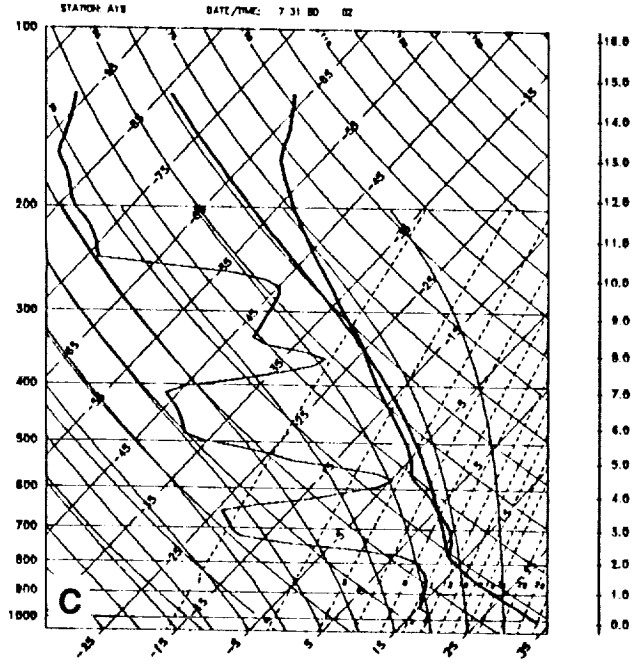

CASE 85 CAPE=1329

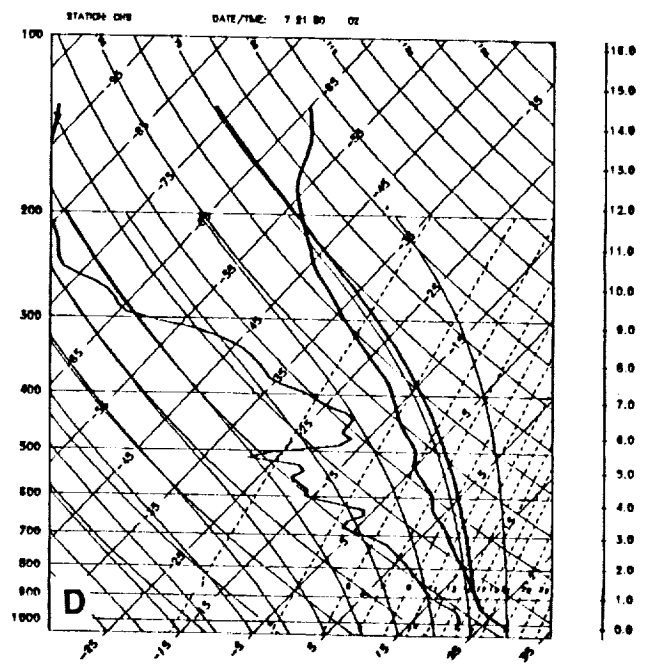

FIGURE 16

ORIGINAL PAGE IS
OF POOR QUALITY

CASE 86 CAPE=1099

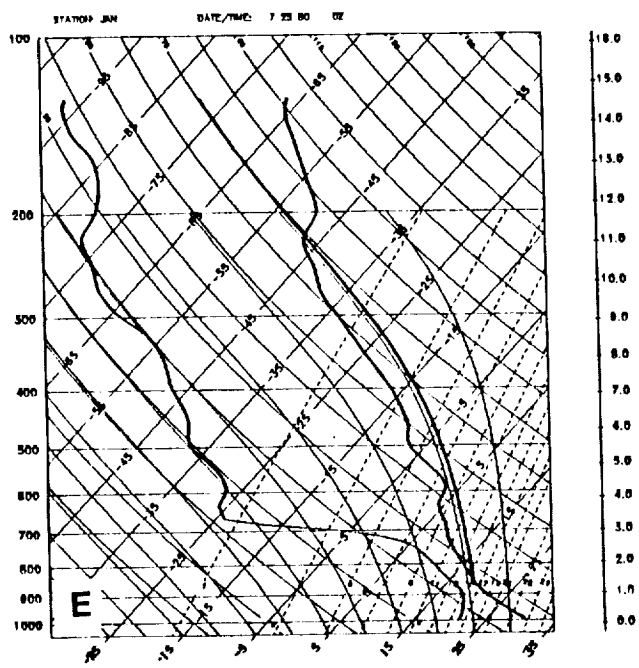

CASE 87 CAPE=377

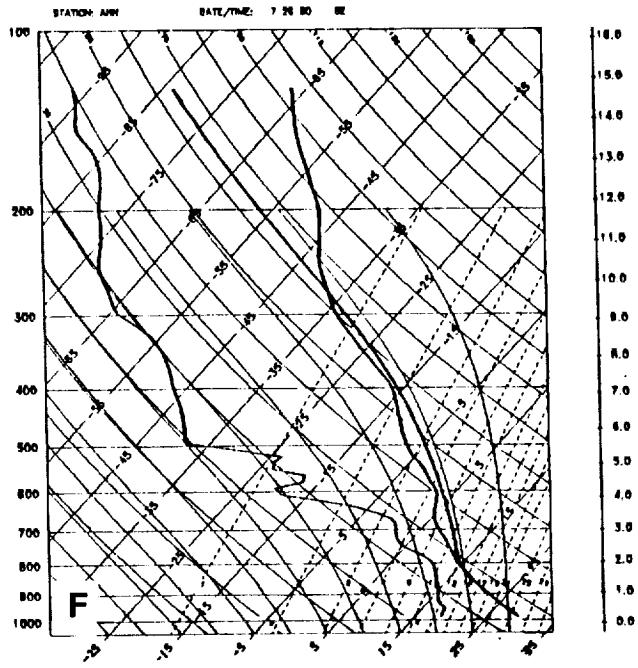

CASE 88 CAPE=232

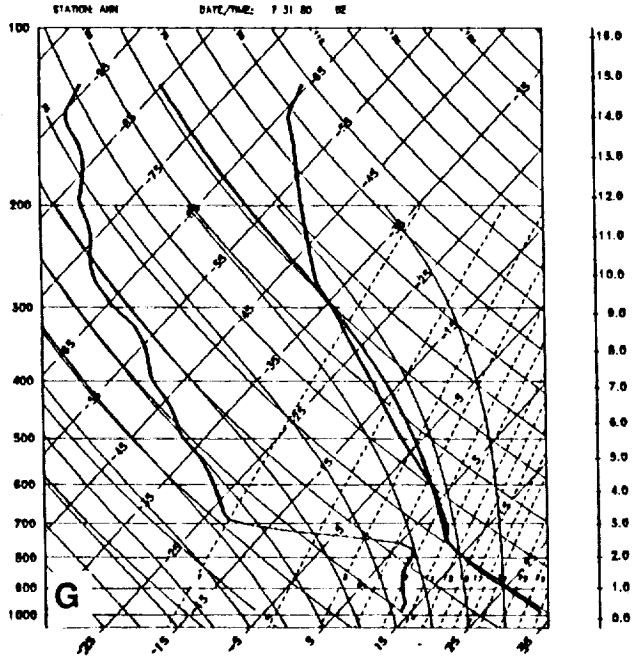

CASE 89 CAPE=1346

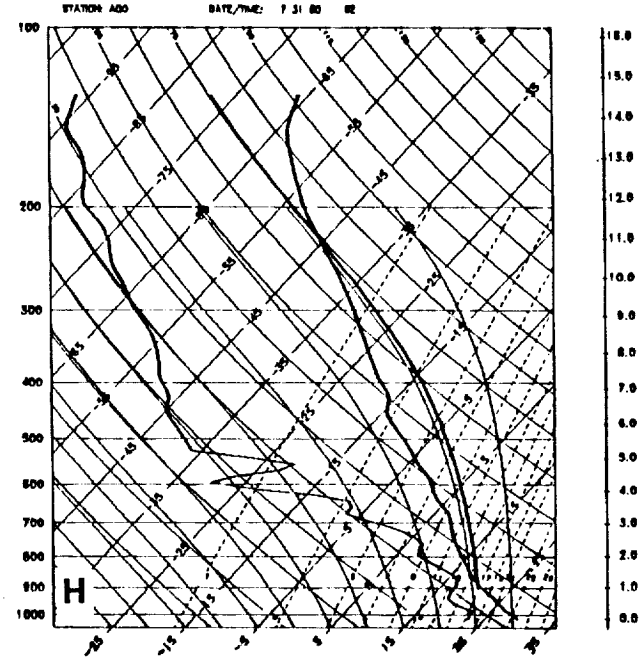

FIGURE 16 cont.

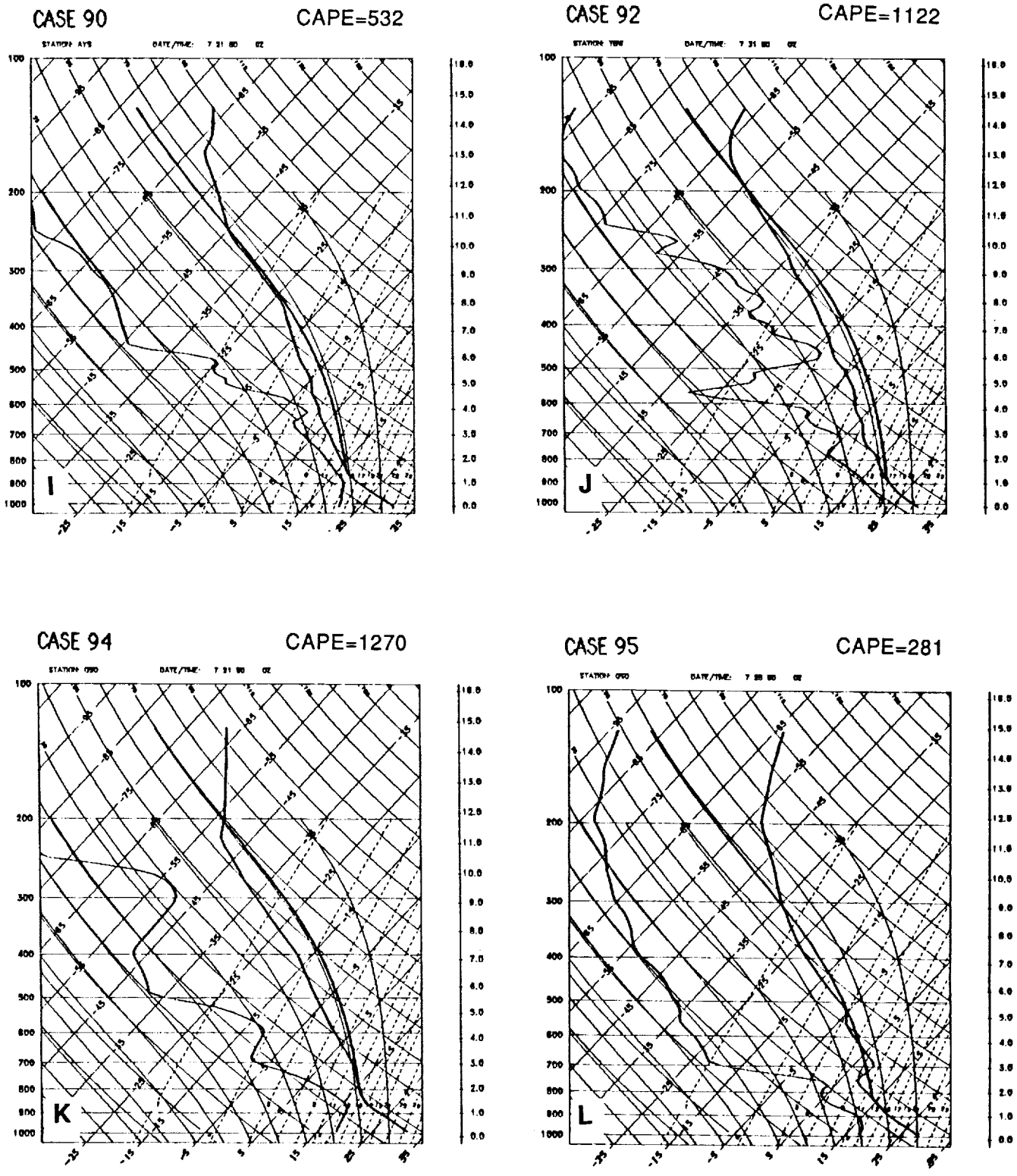

FIGURE 16 cont.

ORIGINAL PAGE IS
OF POOR QUALITY

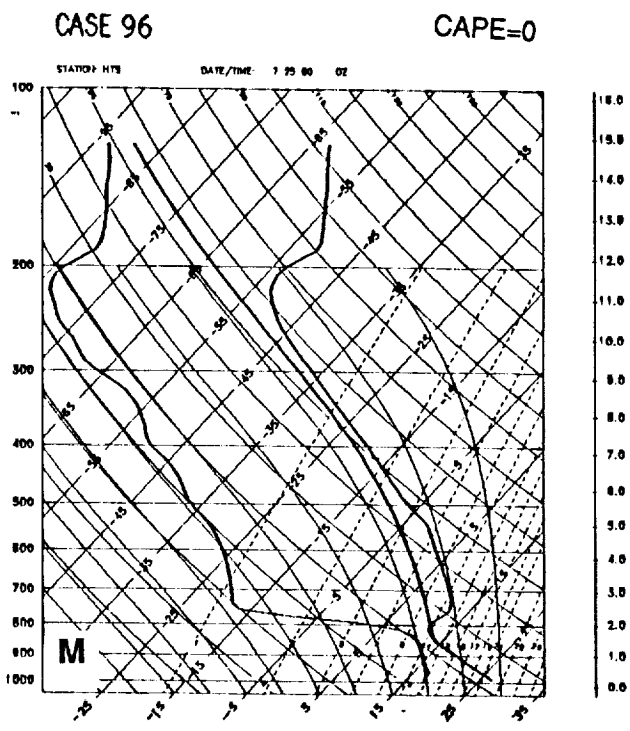

FIGURE 16 cont.

RUN 36
FLUX=1200W/m2
RADIUS=2400m

RUN 37
FLUX=600W/m2
RADIUS=2400m

RUN 38
FLUX=1200W/m2
RADIUS=1600m

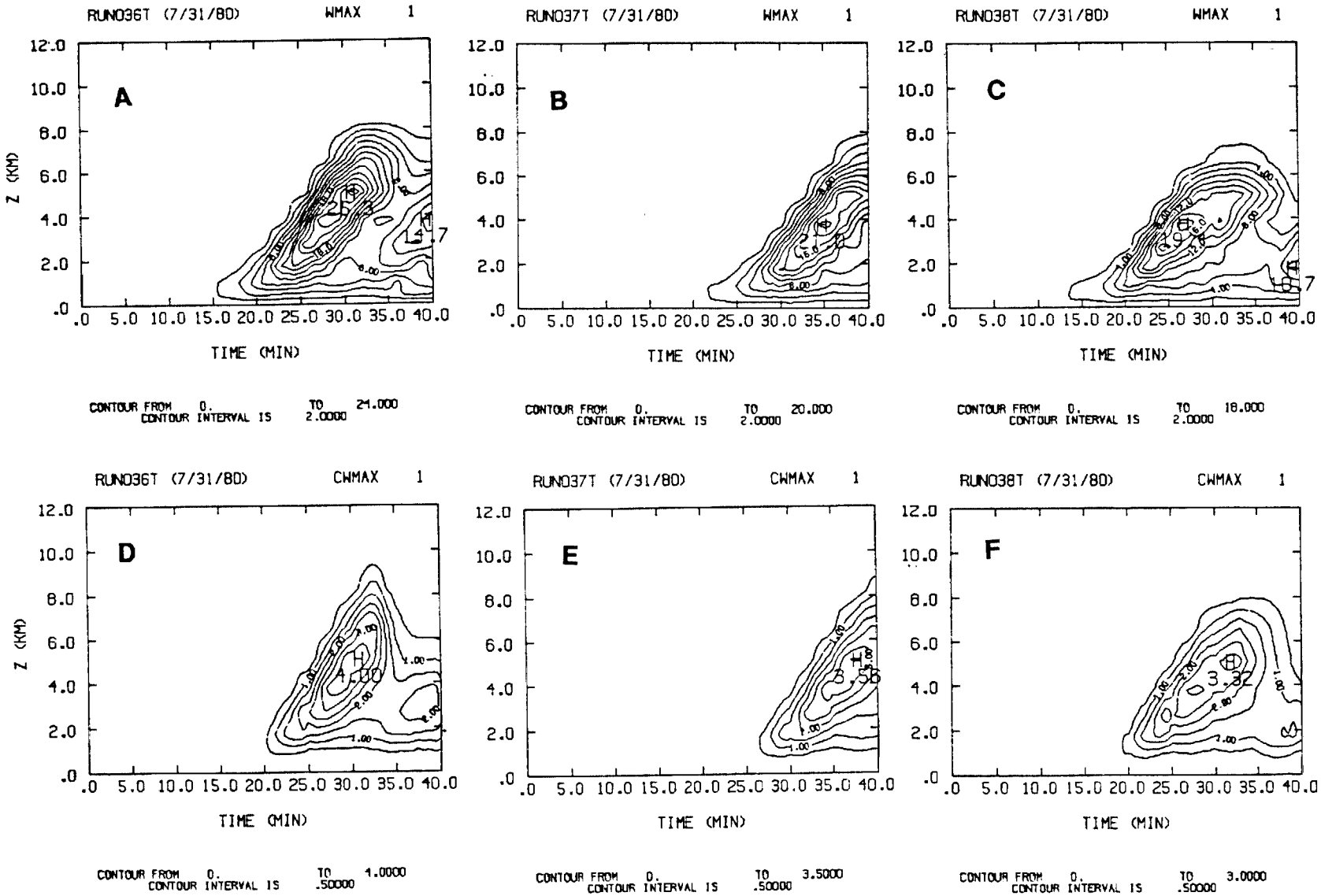

FIGURE 17

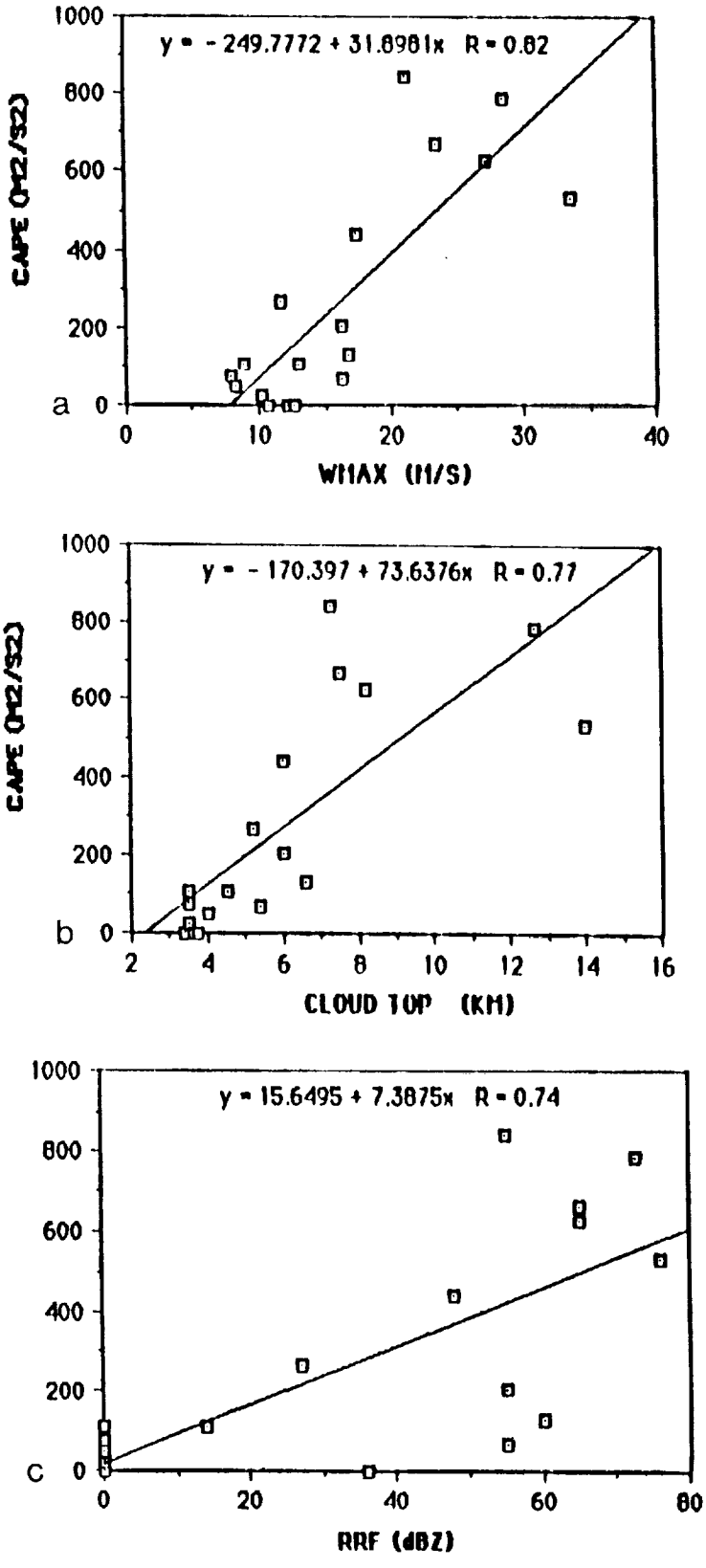
y = -249.7772 + 31.8981x R = 0.82
CAPE (M2/S2)
1000
800
600
400
200
a 0
0
10
20
30
40
W1AX (M/S)
y = -170.397 + 73.6376x R = 0.77
CAPE (M2/S2)
1000
800
600
400
200
b 0
2
4
6
8
10
12
14
16
CLOUD TOP (KM)
y = 15.6495 + 7.3875x R = 0.74
CAPE (M2/S2)
1000
800
600
400
200
c 0
0
20
40
60
80
RRF (dBZ)

FIGURE 18

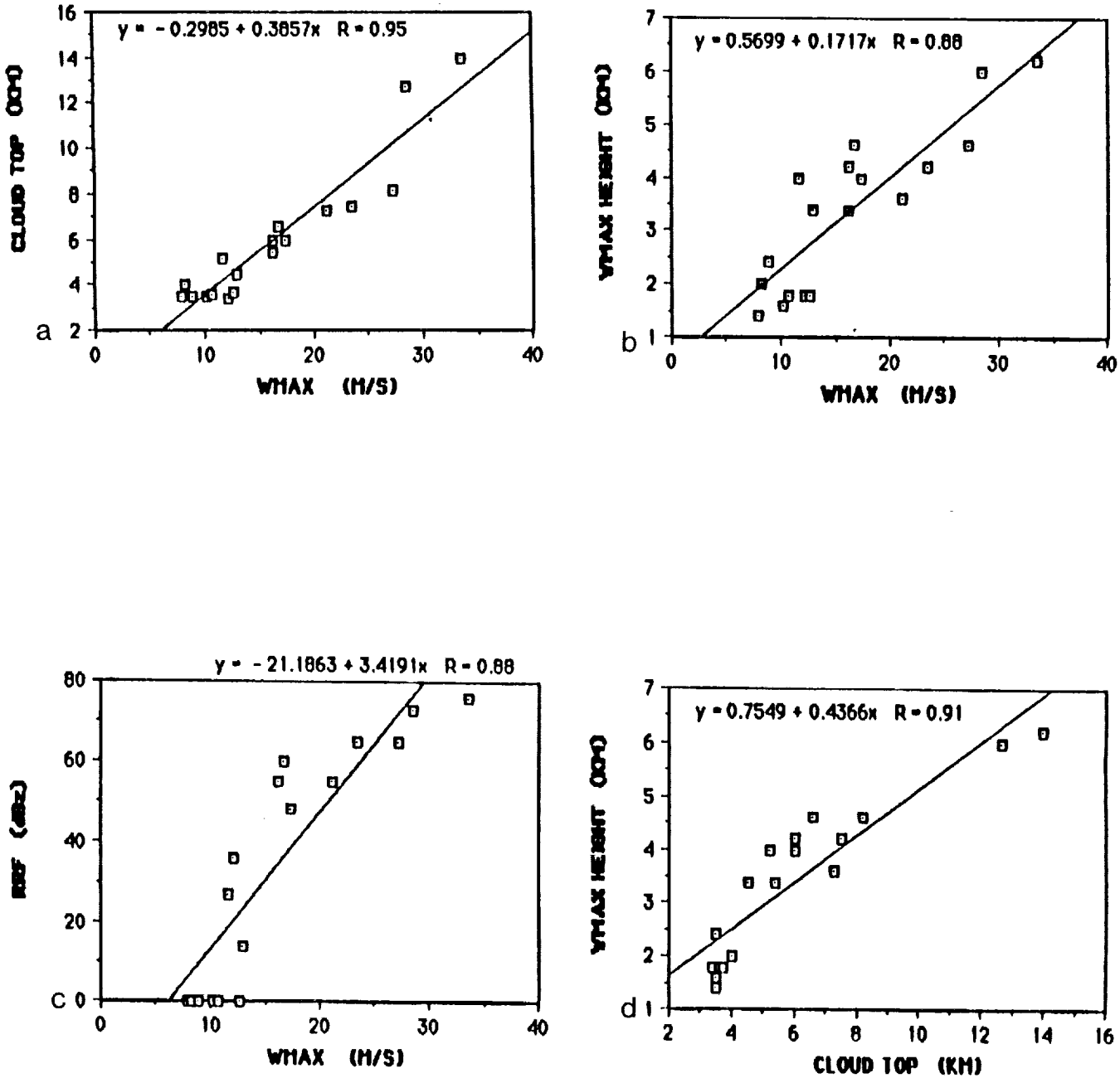
y = -0.2985 + 0.3857x R = 0.95
CLOUD TOP (KM)
WMAX (M/S)
a
y = 0.5699 + 0.1717x R = 0.88
VMAX HEIGHT (KM)
WMAX (M/S)
b
y = -21.1863 + 3.4191x R = 0.88
REF (dBz)
WMAX (M/S)
c
y = 0.7549 + 0.4366x R = 0.91
VMAX HEIGHT (KM)
CLOUD TOP (KM)
d

FIGURE 19

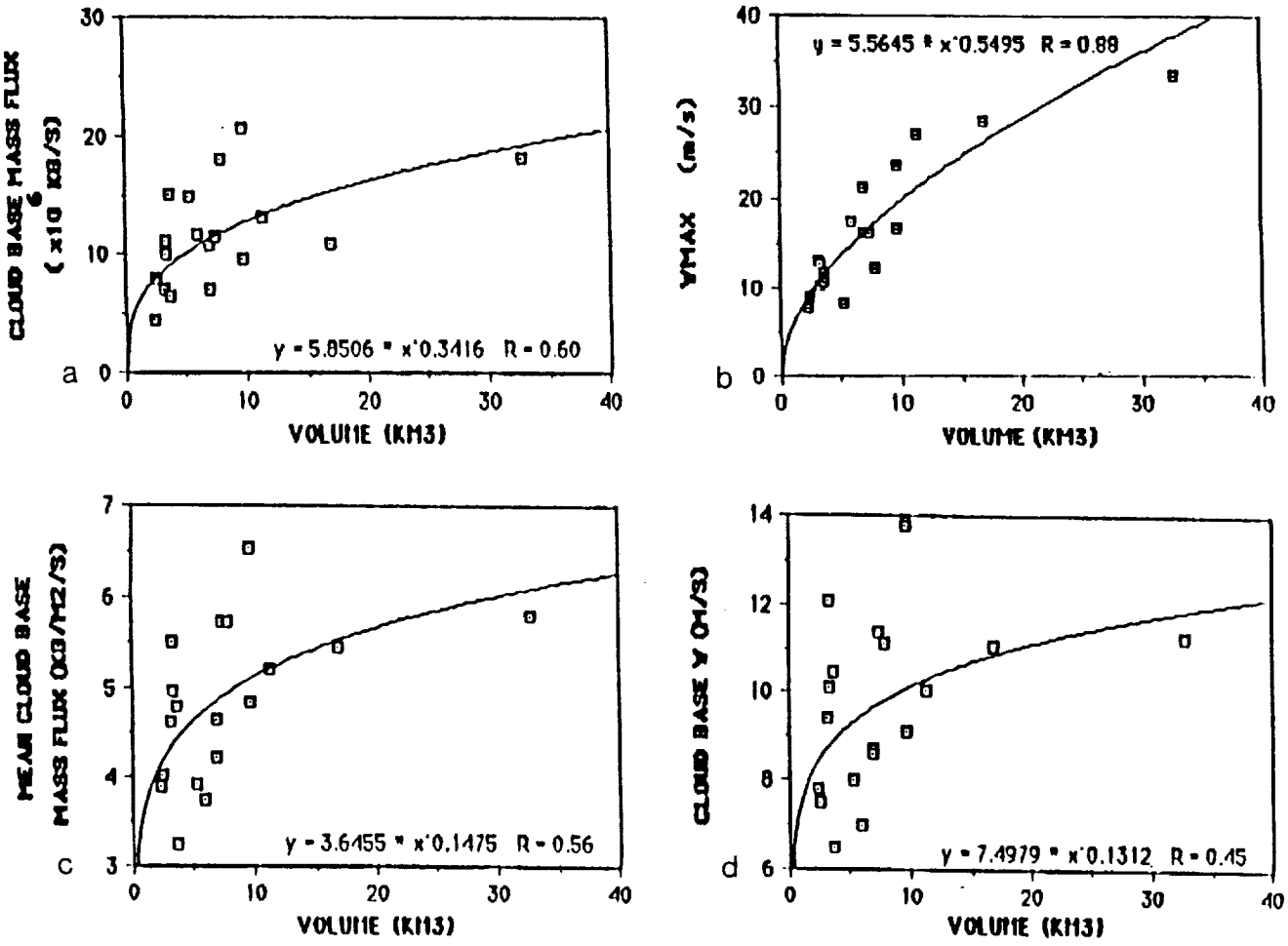
a
CLOUD BASE MASS FLUX
(x10 KG/S)
y = 5.8506 * x'0.3416 R = 0.60
VOLUME (KM3)
b
YMAX (m/s)
y = 5.5645 * x'0.5495 R = 0.88
VOLUME (KM3)
c
MEAN CLOUD BASE
MASS FLUX (KG/M2/S)
y = 3.6455 * x'0.1475 R = 0.56
VOLUME (KM3)
d
CLOUD BASE W (M/S)
y = 7.4979 * x'0.1312 R = 0.45
VOLUME (KM3)

FIGURE 20

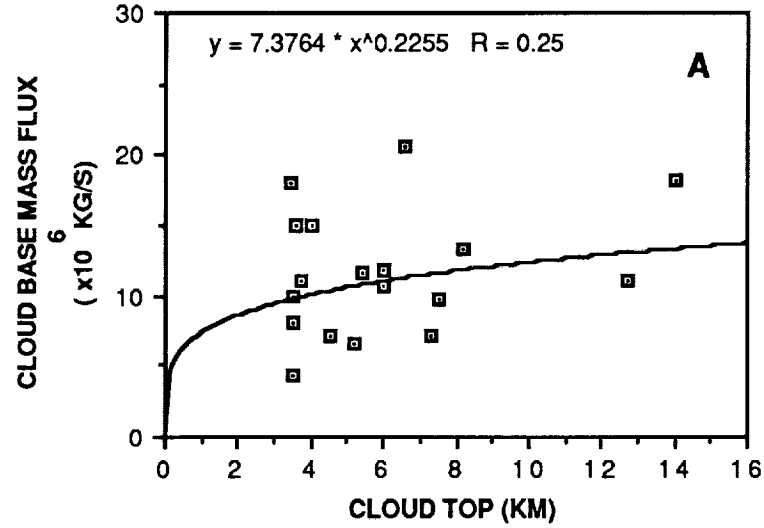
y = 7.3764 * x^0.2255 R = 0.25
A
CLOUD BASE MASS FLUX
6
(x10 KG/S)
30
20
10
0
0 2 4 6 8 10 12 14 16
CLOUD TOP (KM)

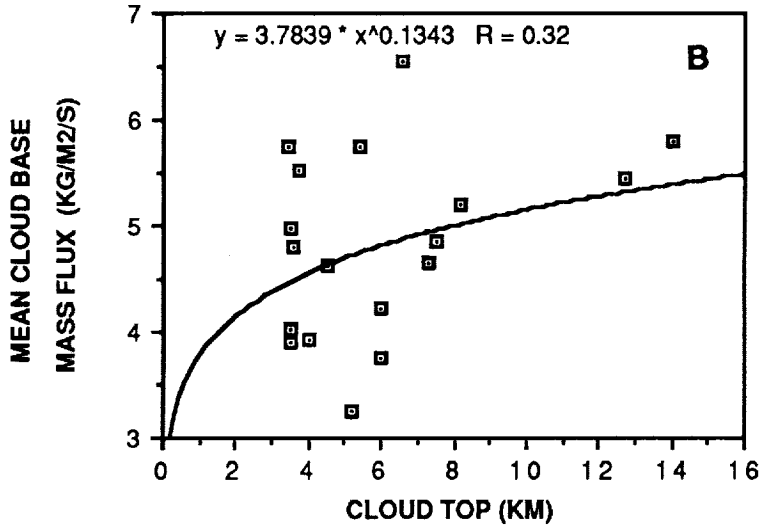
y = 3.7839 * x^0.1343 R = 0.32
B
MEAN CLOUD BASE
MASS FLUX (KG/M2/S)
7
6
5
4
3
0 2 4 6 8 10 12 14 16
CLOUD TOP (KM)

FIGURE 21

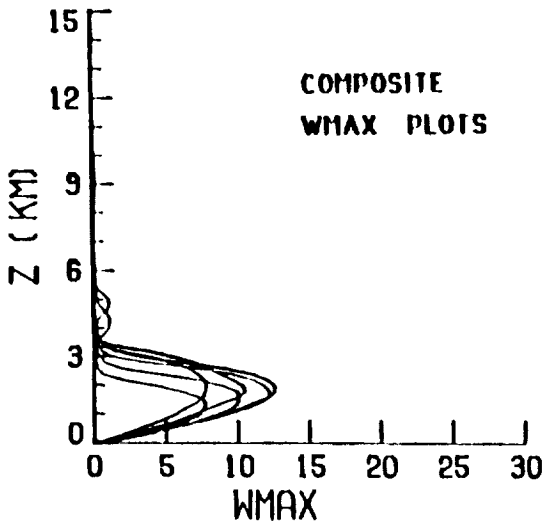

a

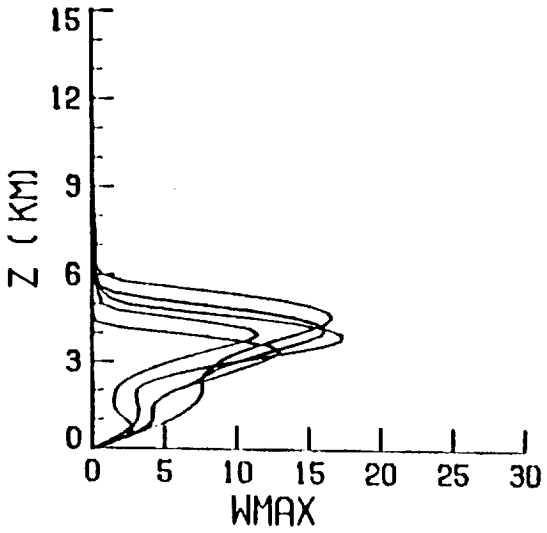

b

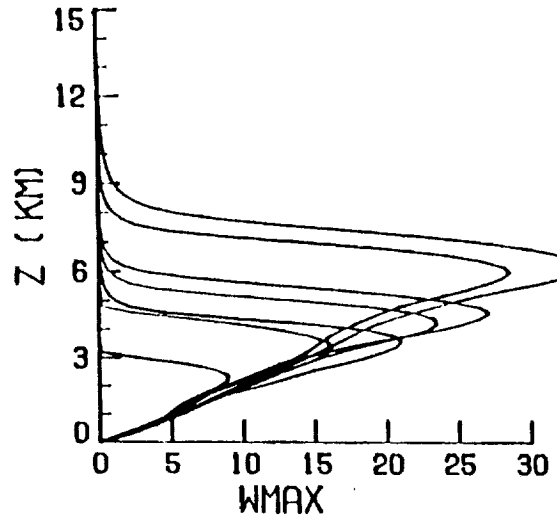

c

FIGURE 22

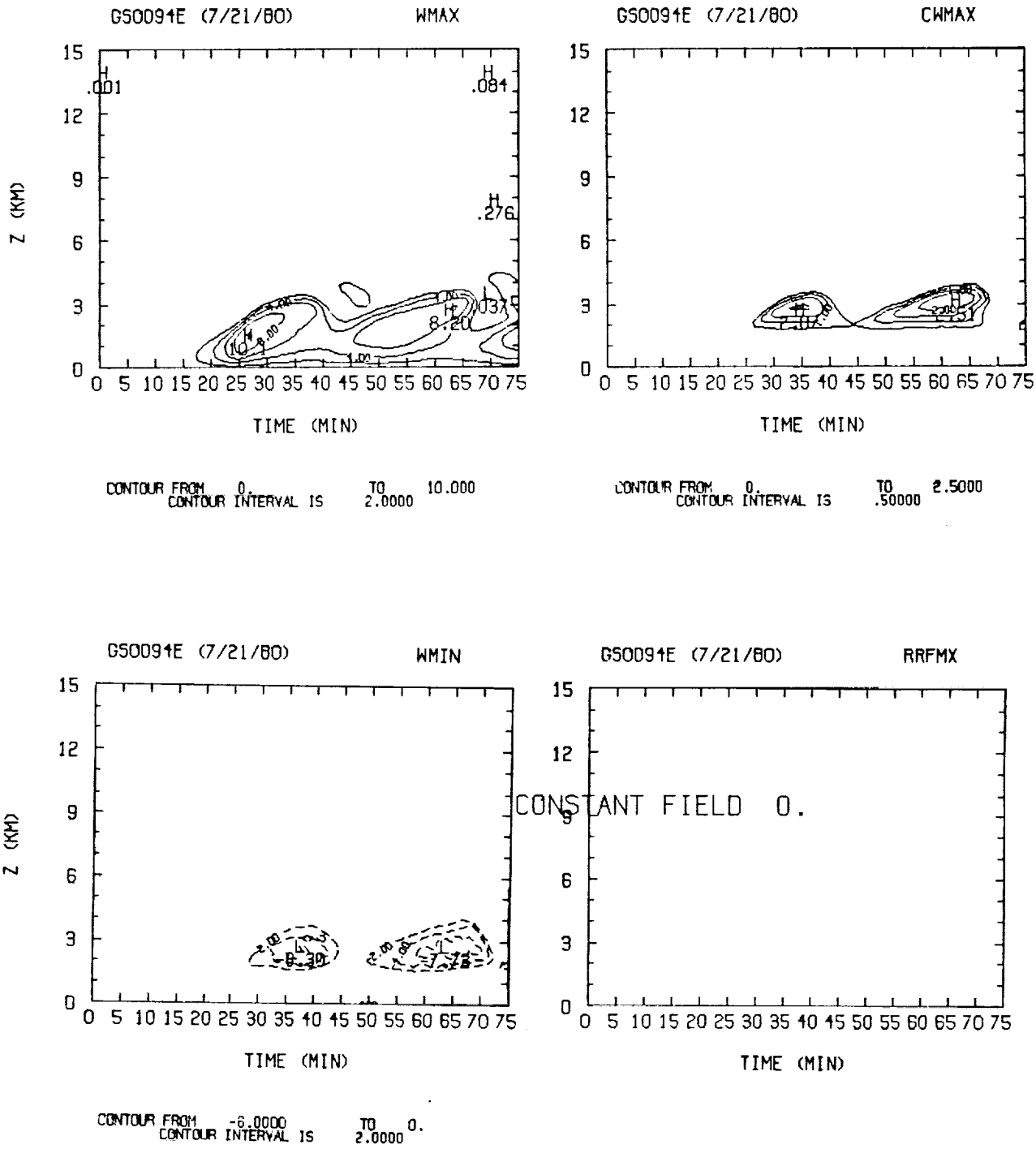
GS0091E (7/21/80) WMAX
GS0091E (7/21/80) CWMAX
GS0091E (7/21/80) WMIN
GS0091E (7/21/80) RRFMX
Z (KM)
TIME (MIN)
CONTOUR FROM 0. TO 10.000
CONTOUR INTERVAL IS 2.0000
CONTOUR FROM 0. TO 2.5000
CONTOUR INTERVAL IS .50000
CONTOUR FROM -6.0000 TO 0.
CONTOUR INTERVAL IS 2.0000
CONSTANT FIELD 0.

FIGURE 23

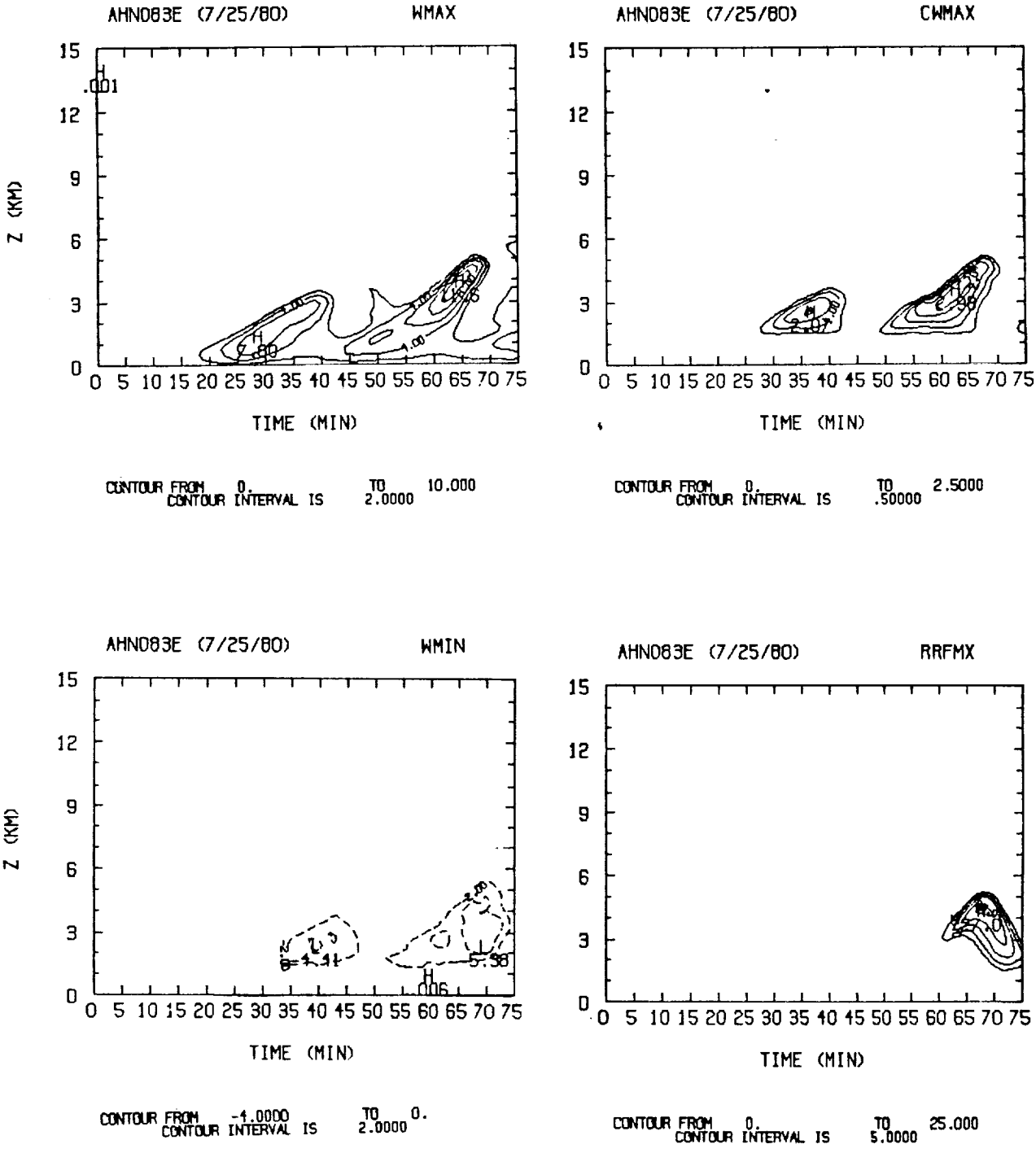

FIGURE 23 cont.

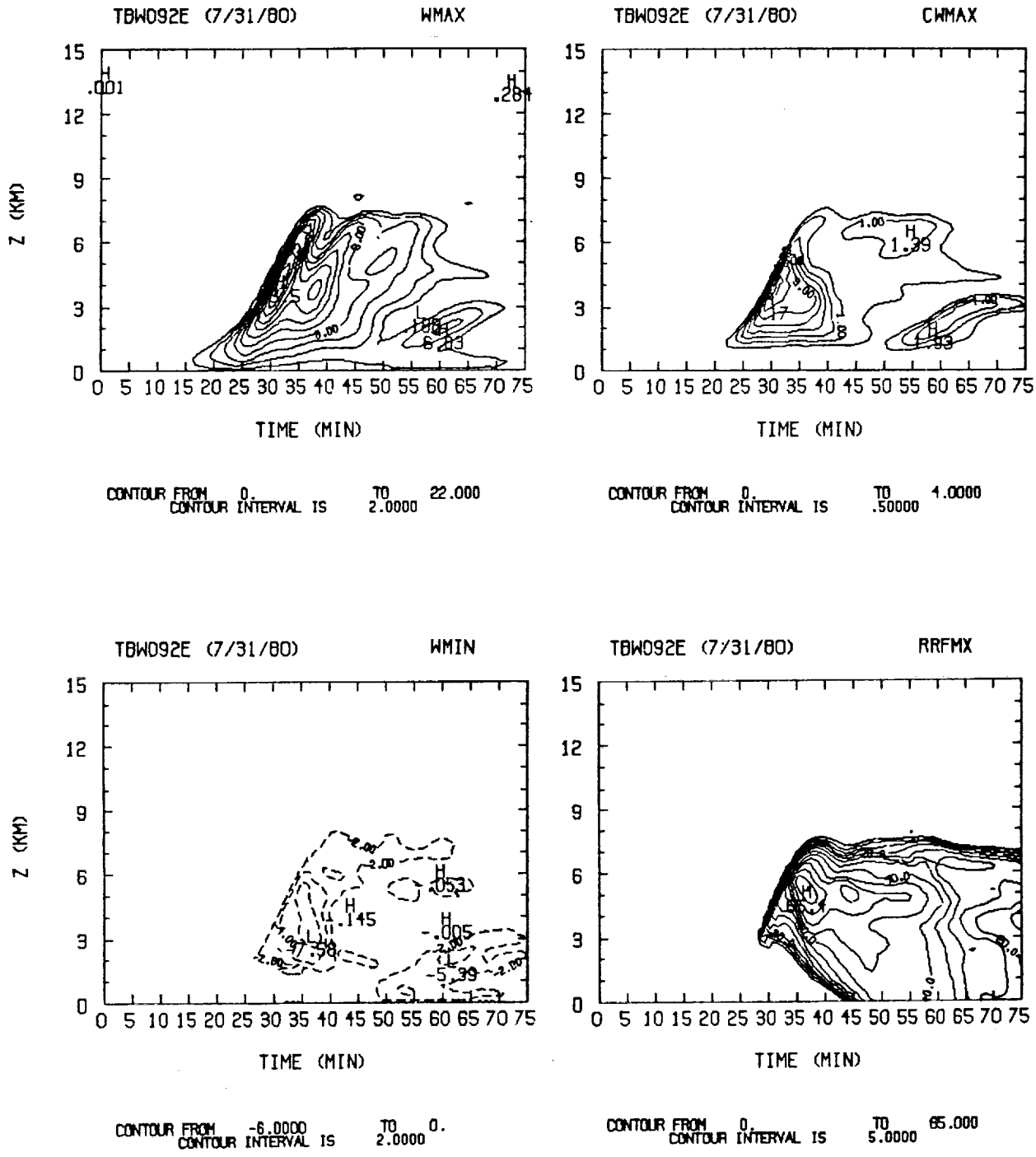

FIGURE 23 cont.

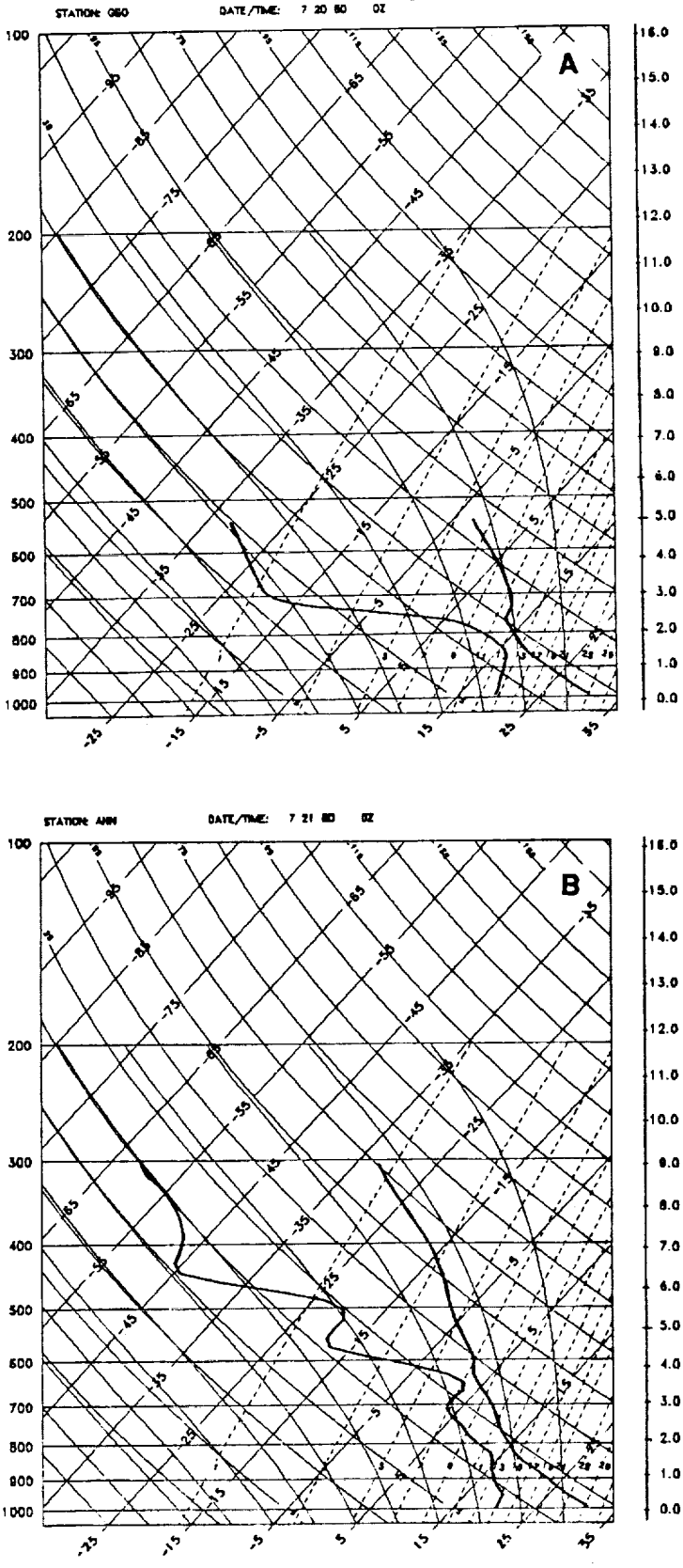

FIGURE 24

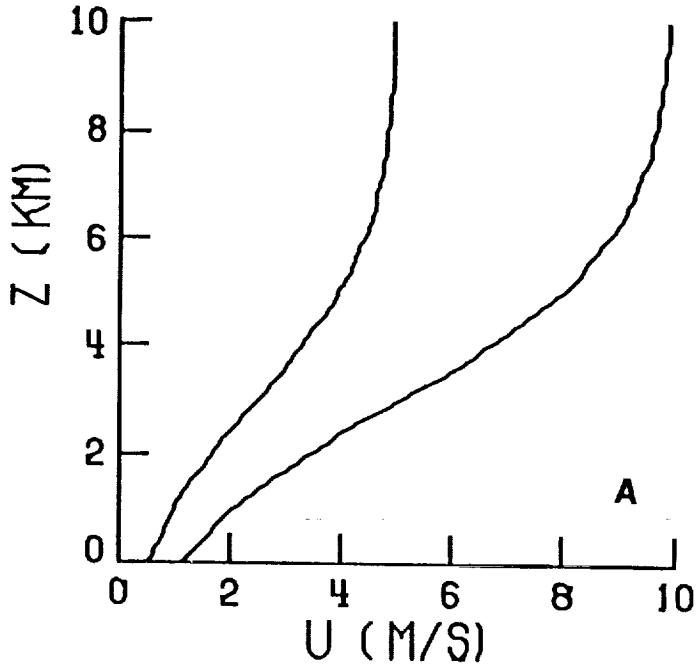

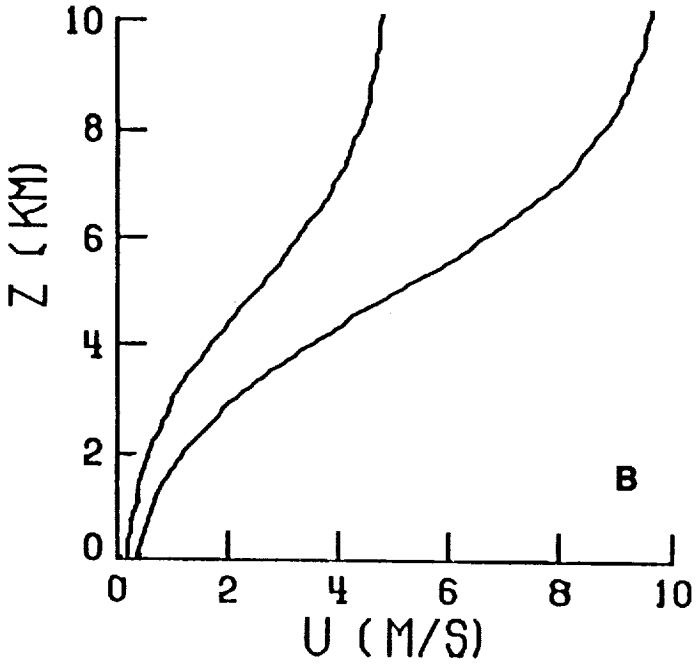

FIGURE 25

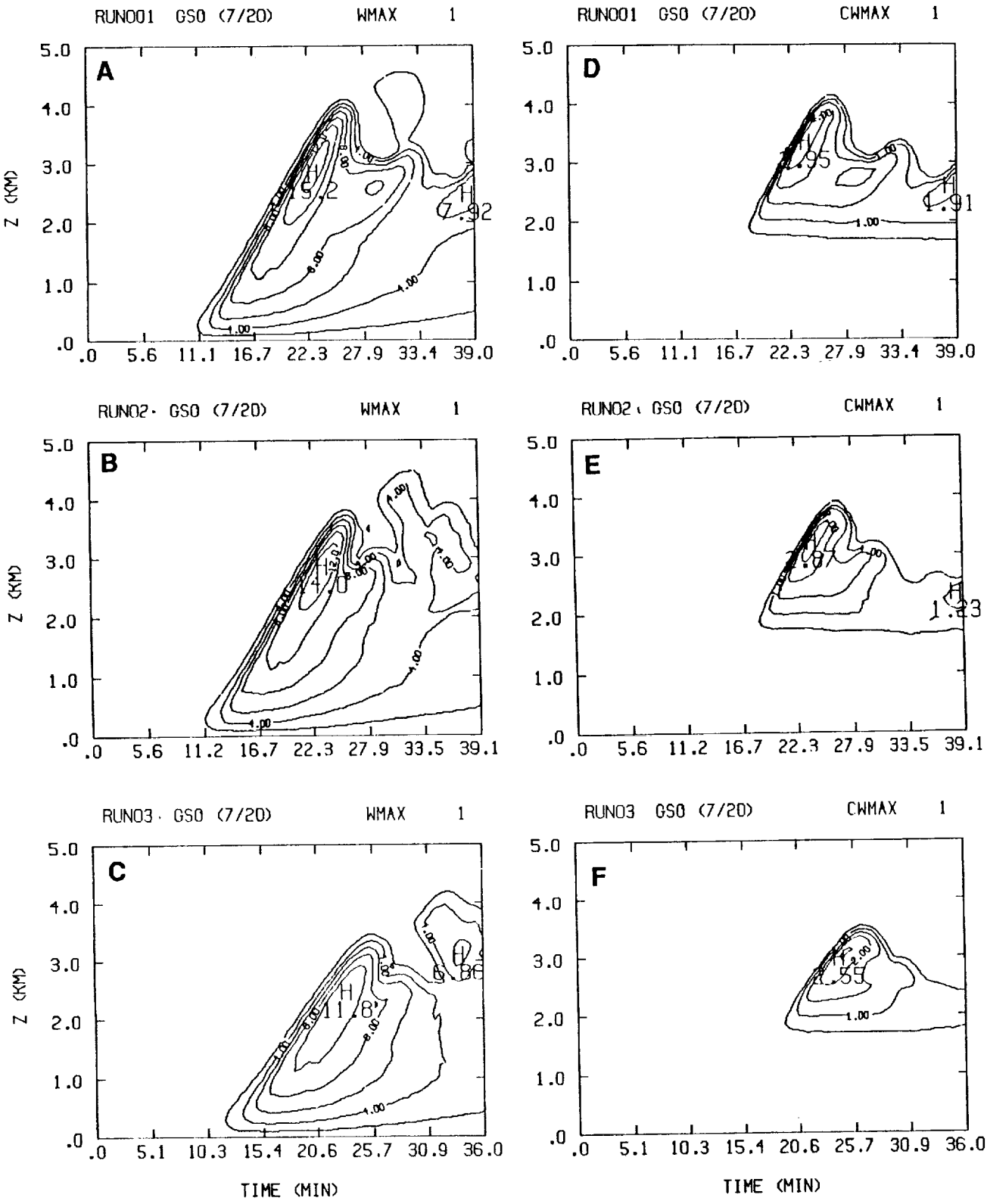
RUN001 GS0 (7/20) WMAX 1
A
RUN001 GS0 (7/20) CWMAX 1
D
RUN02 GS0 (7/20) WMAX 1
B
RUN02 GS0 (7/20) CWMAX 1
E
RUN03 GS0 (7/20) WMAX 1
C
RUN03 GS0 (7/20) CWMAX 1
F
Z (KM)
TIME (MIN)

FIGURE 26

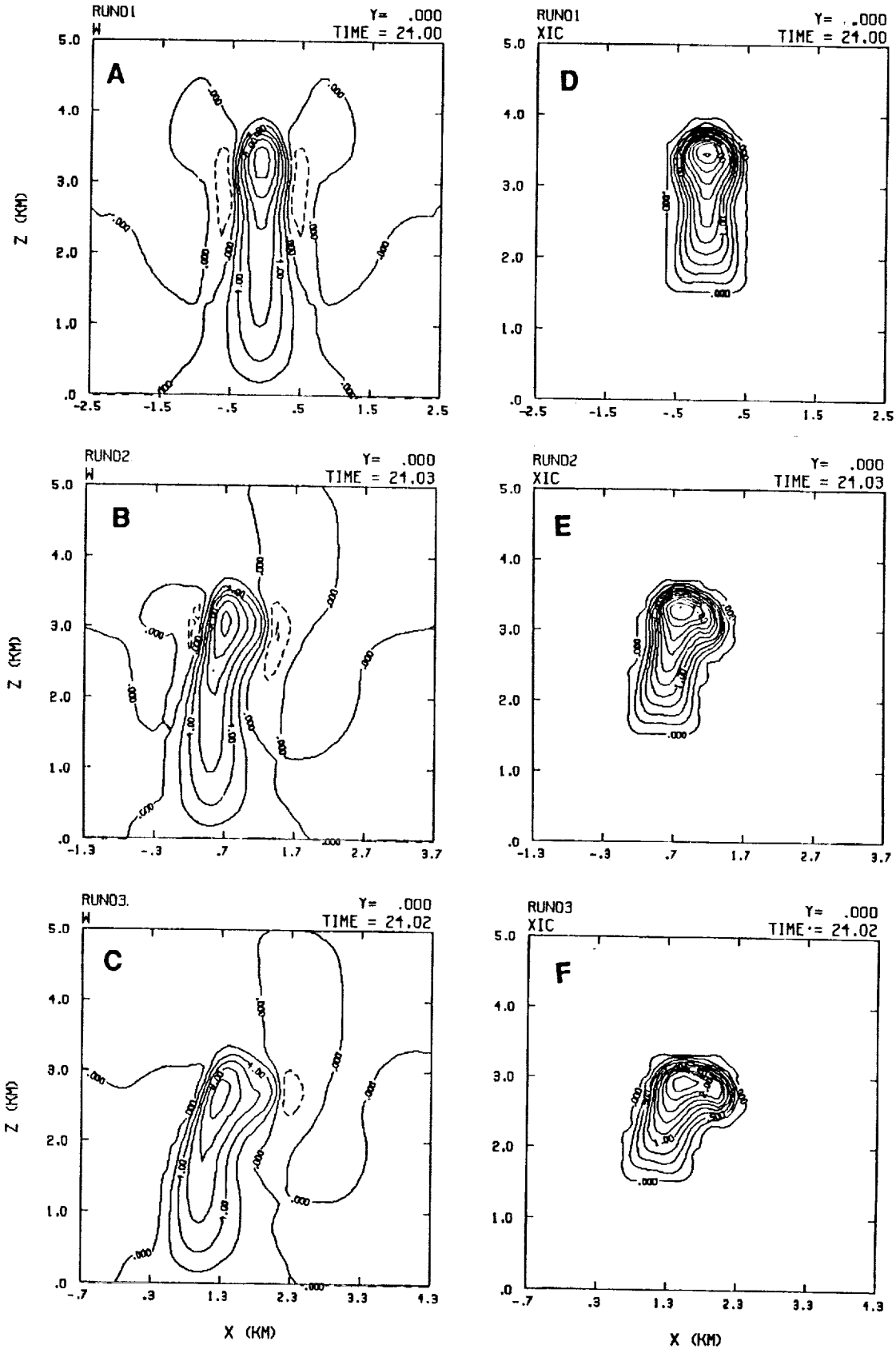
RUN01
W
Y= .000
TIME = 21.00
A
RUN01
XIC
Y= .000
TIME = 21.00
D
RUN02
W
Y= .000
TIME = 21.03
B
RUN02
XIC
Y= .000
TIME = 21.03
E
RUN03
W
Y= .000
TIME = 21.02
C
RUN03
XIC
Y= .000
TIME = 21.02
F
Z (KM)
X (KM)

FIGURE 27

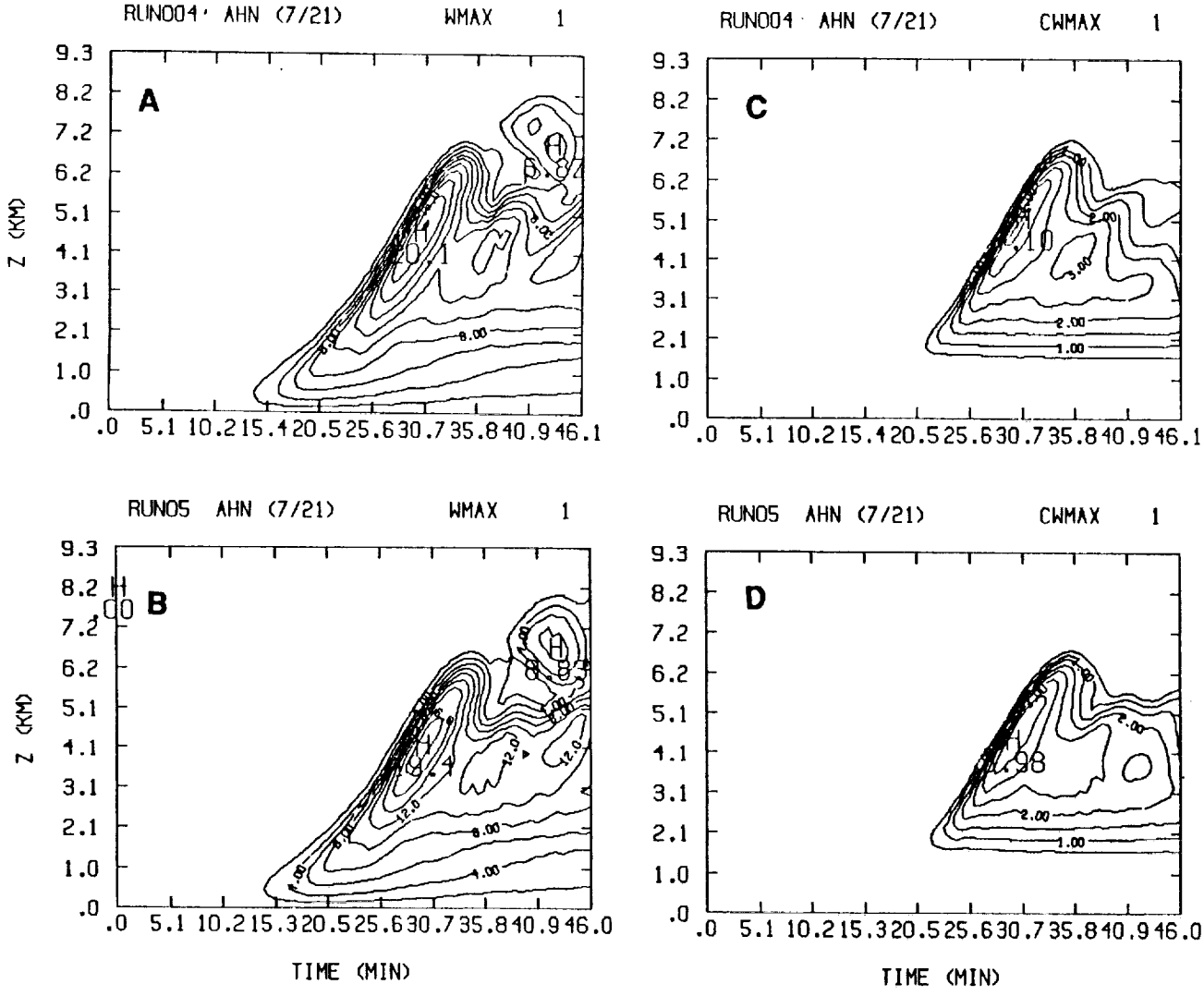
RUN004 AHN (7/21) WMAX 1
A
RUN004 AHN (7/21) CWMAX 1
C
RUN05 AHN (7/21) WMAX 1
B
RUN05 AHN (7/21) CWMAX 1
D
Z (KM)
9.3
8.2
7.2
6.2
5.1
4.1
3.1
2.1
1.0
.0
.0 5.1 10.2 15.4 20.5 25.6 30.7 35.8 40.9 46.1
.0 5.1 10.2 15.3 20.5 25.6 30.7 35.8 40.9 46.0
TIME (MIN)

FIGURE 28

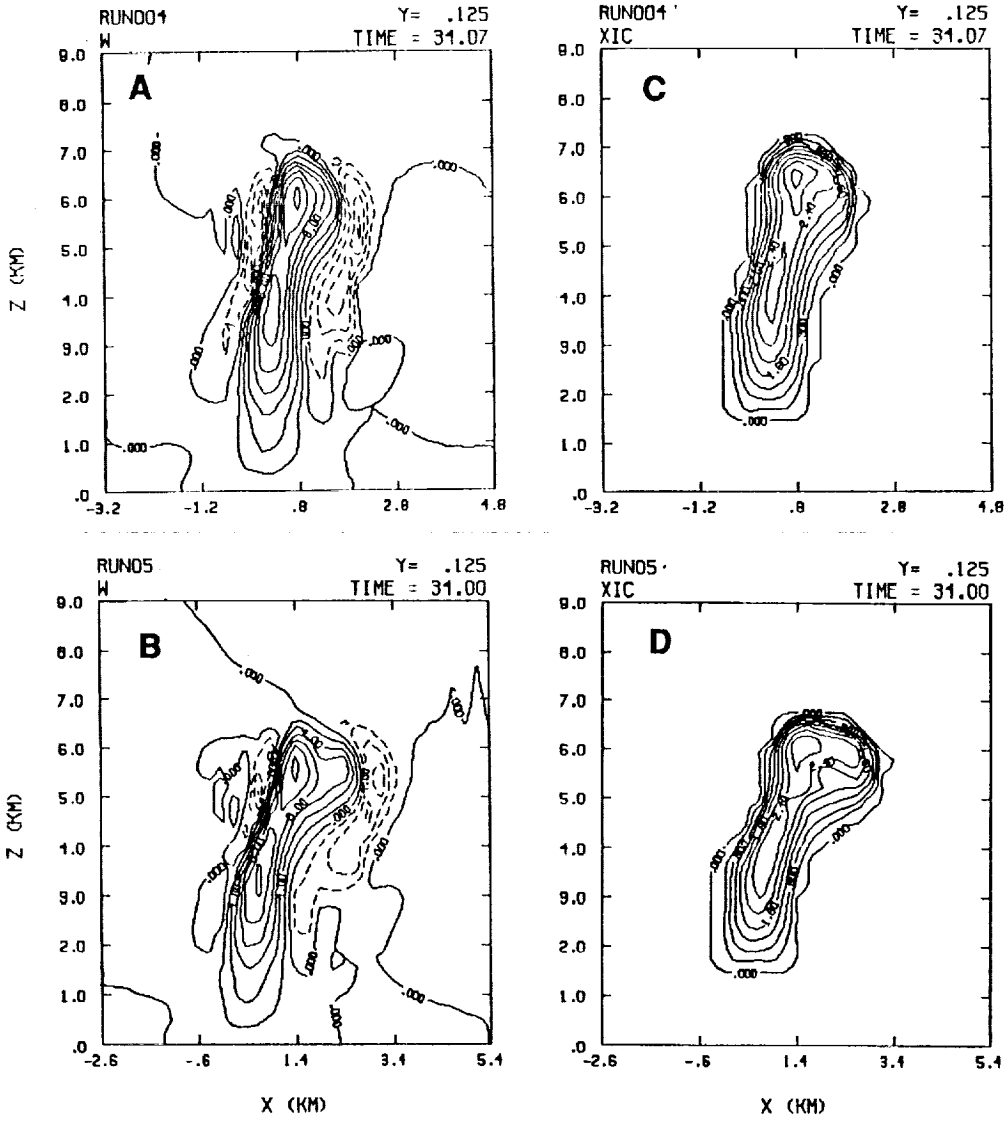
RUN004
W
Y= .125
TIME = 31.07
A
RUN004
XIC
Y= .125
TIME = 31.07
C
RUN05
W
Y= .125
TIME = 31.00
B
RUN05
XIC
Y= .125
TIME = 31.00
D
Z (KM)
X (KM)

FIGURE 29

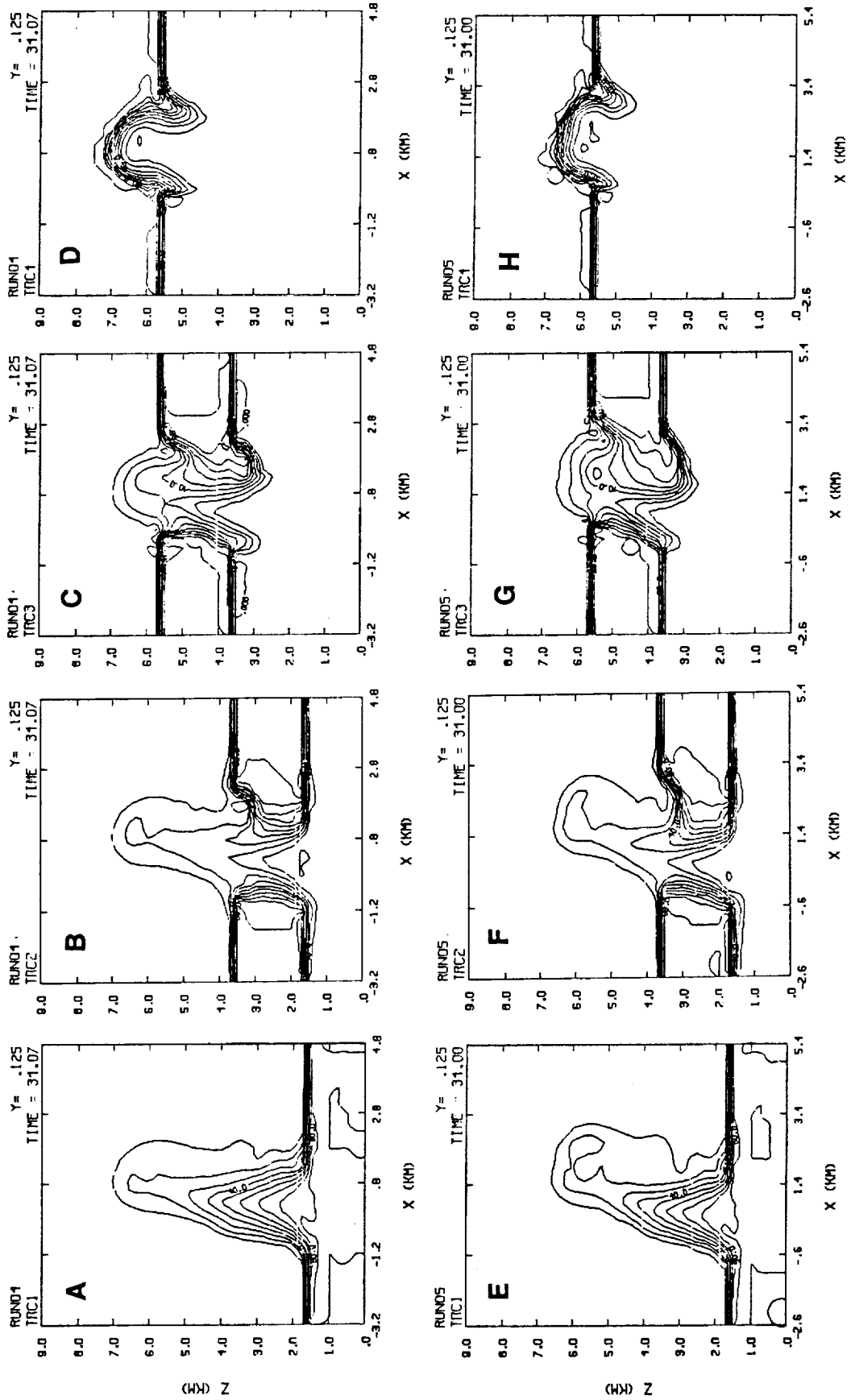
A
B
C
D
E
F
G
H
RUN01
TRC1
RUN01
TRC2
RUN01
TRC3
RUN05
TRC1
RUN05
TRC2
RUN05
TRC3
Y= .125
TIME = 31.07
TIME = 31.00
Z (KM)
X (KM)

FIGURE 30

CASE 1 - NO SHEAR

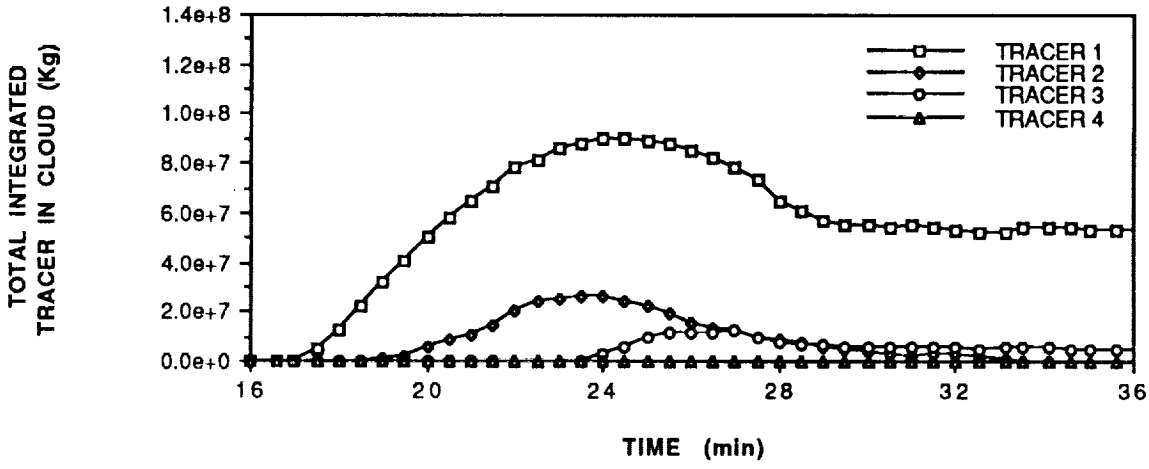

[A]

CASE 2 - LOW SHEAR

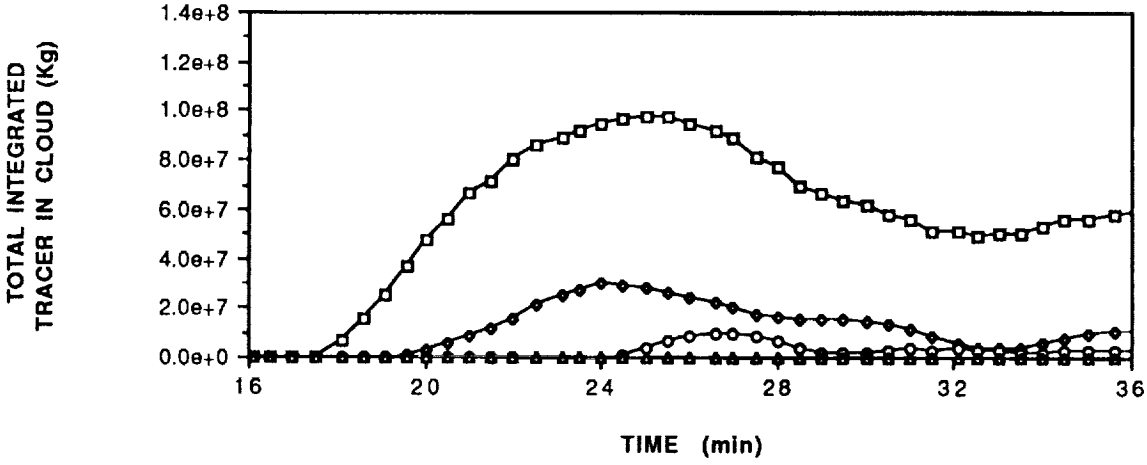

[B]

CASE 3 - MODERATE SHEAR

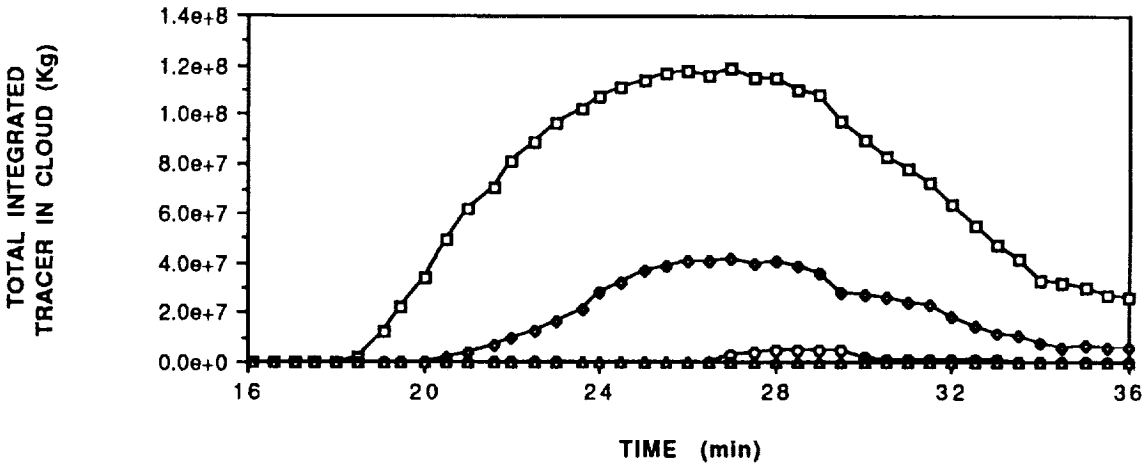

[C]

FIGURE 31

CASE 4 - LOW SHEAR

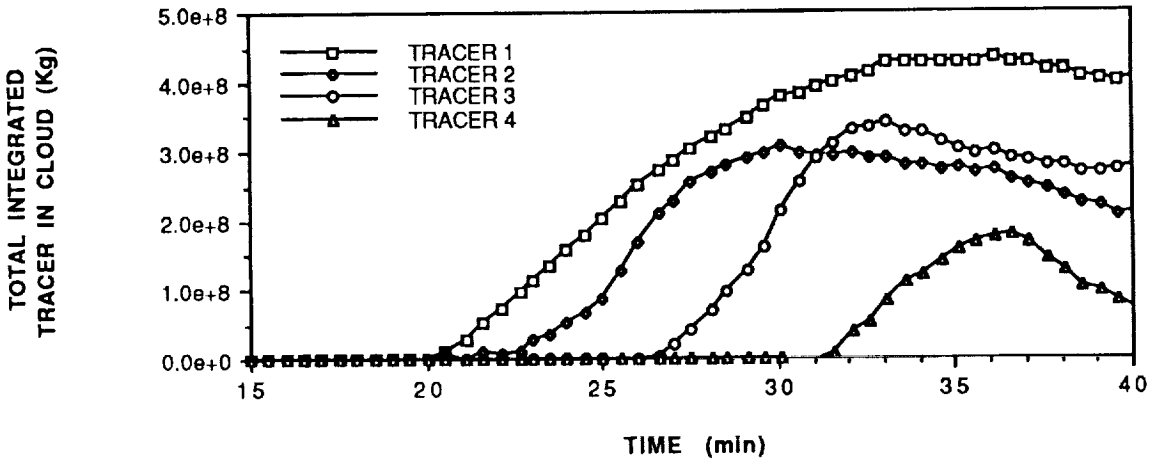

[A]

CASE 5 - MODERATE SHEAR

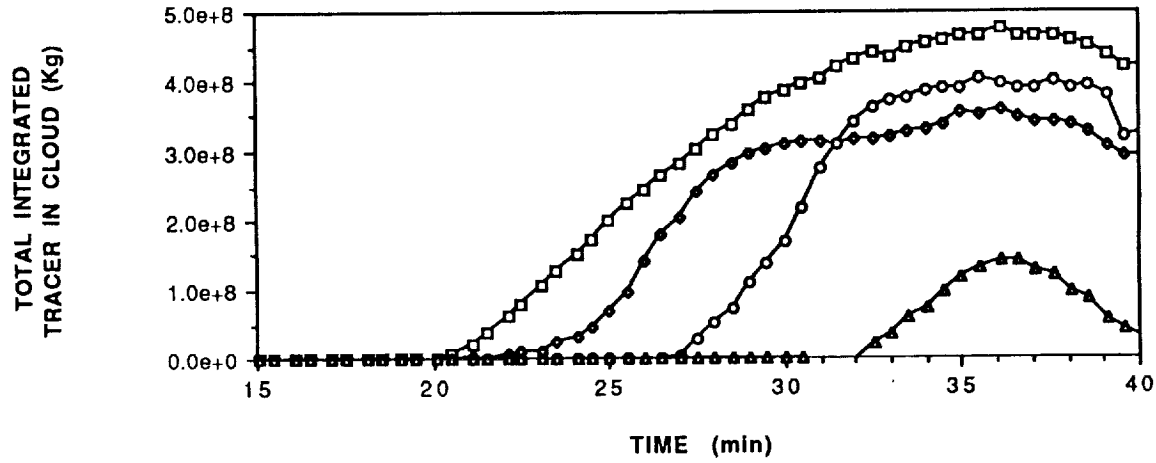

[B]

FIGURE 32

CASE 1 - NO SHEAR

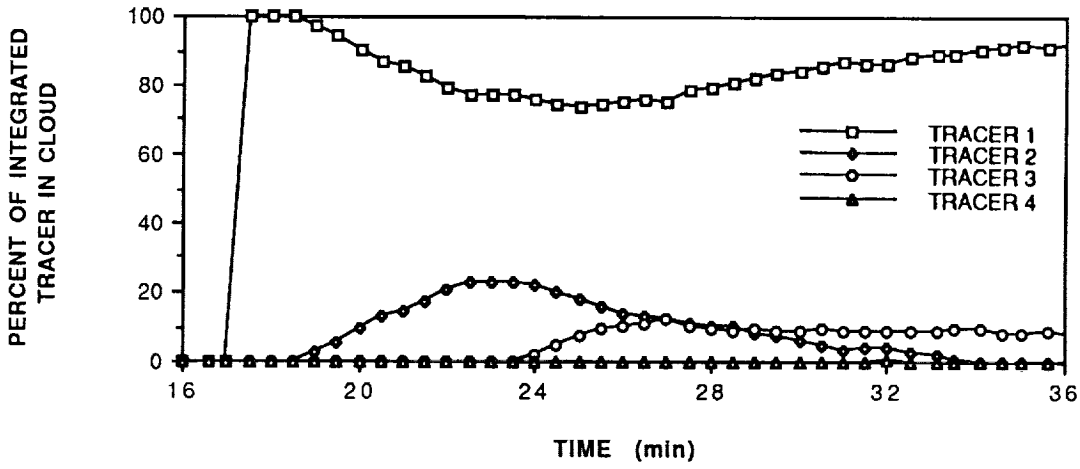

[A]

CASE 2 - LOW SHEAR

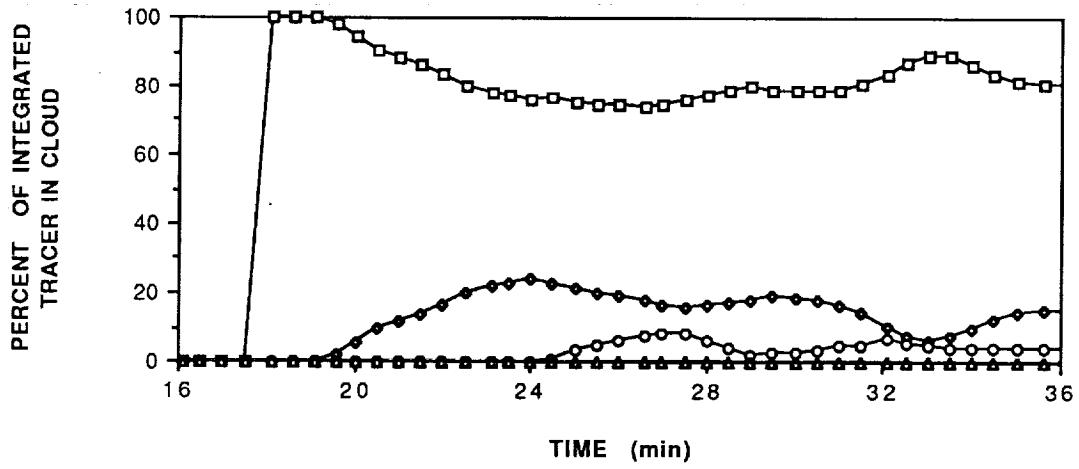

[B]

CASE 3 - MODERATE SHEAR

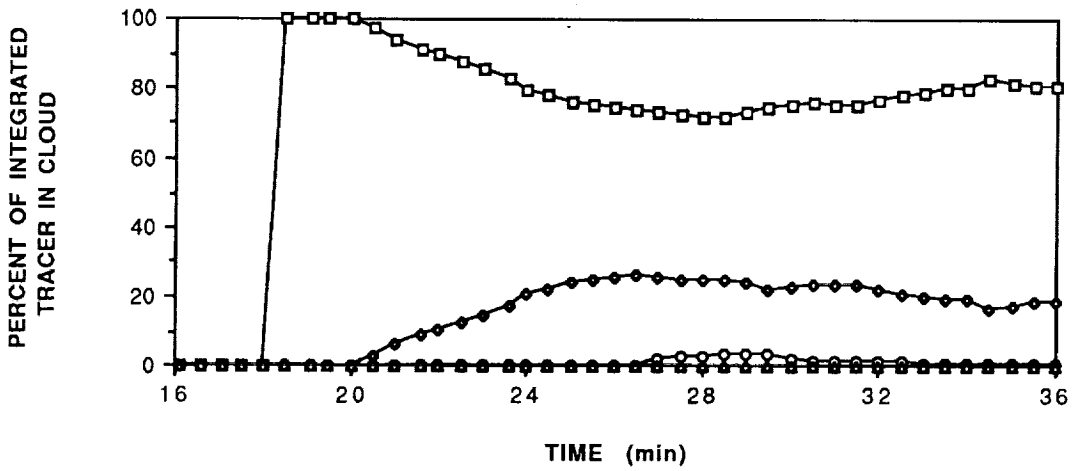

[C]

FIGURE 33

CASE 4 - LOW SHEAR

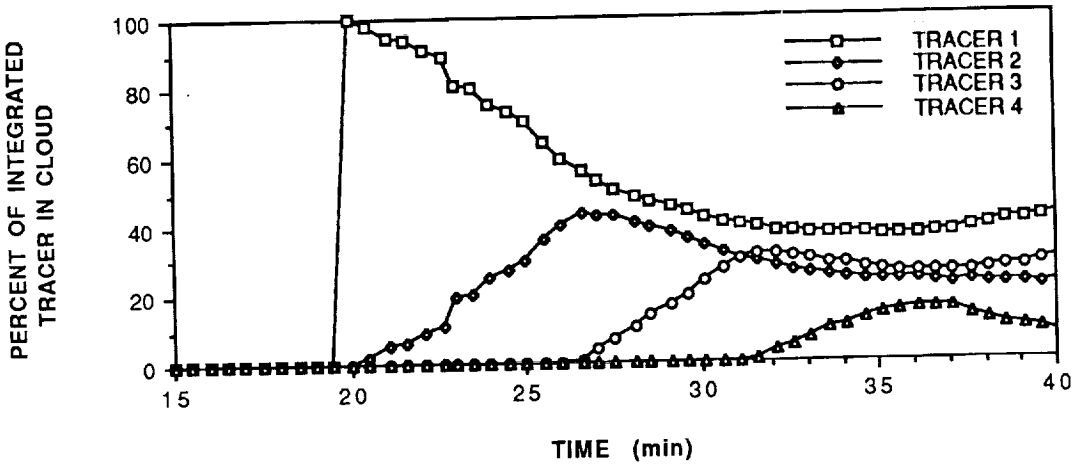

[A]

CASE 5 - MODERATE SHEAR

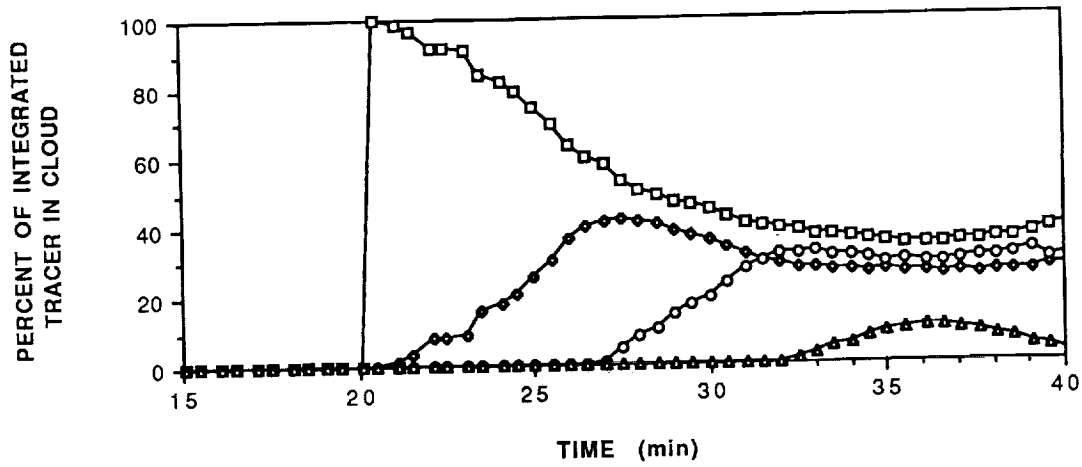

[B]

FIGURE 34

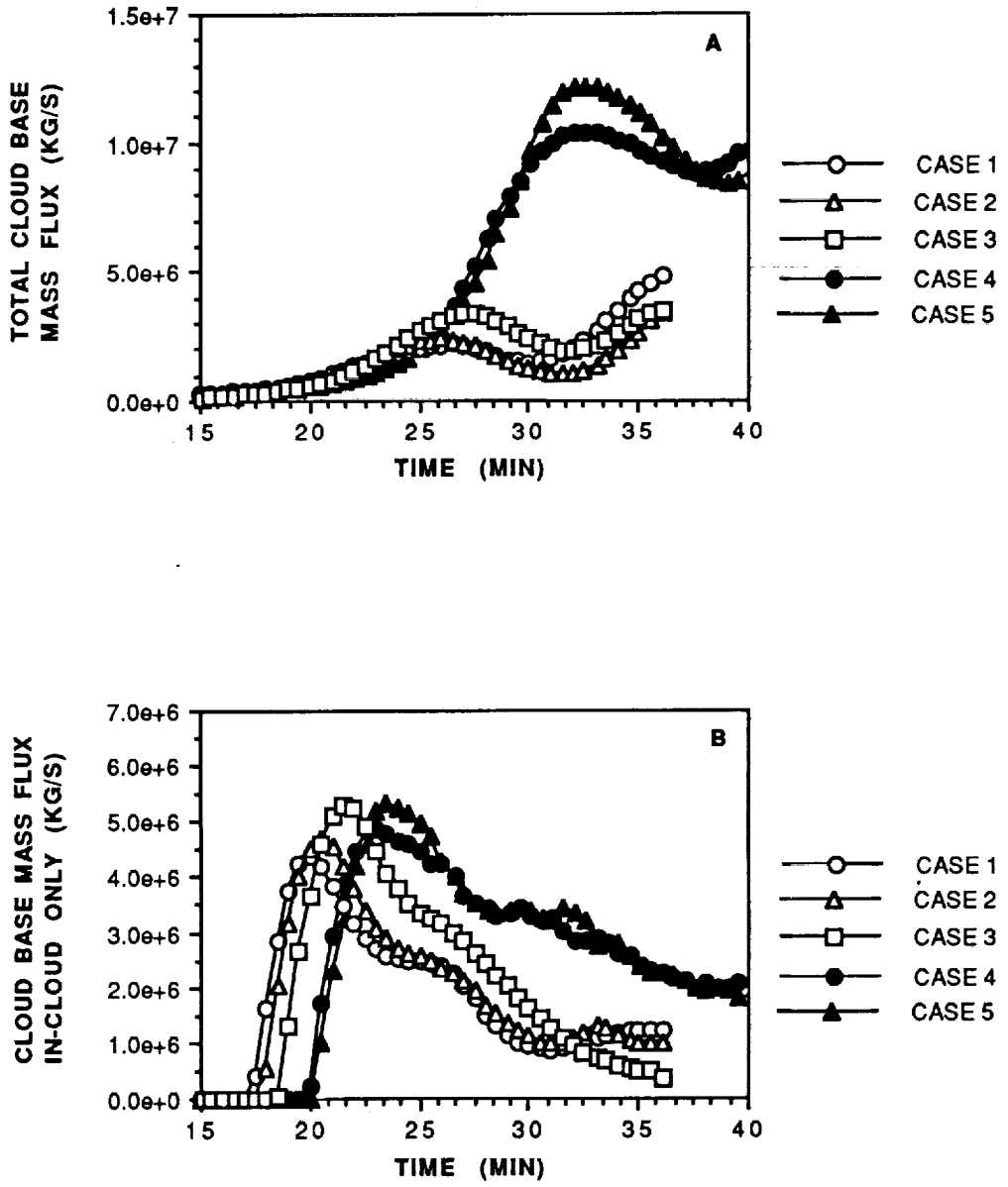
A
TOTAL CLOUD BASE MASS FLUX (KG/S)
1.5e+7
1.0e+7
5.0e+6
0.0e+0
15
20
25
30
35
40
TIME (MIN)
CASE 1
CASE 2
CASE 3
CASE 4
CASE 5
B
CLOUD BASE MASS FLUX IN-CLOUD ONLY (KG/S)
7.0e+6
6.0e+6
5.0e+6
4.0e+6
3.0e+6
2.0e+6
1.0e+6
0.0e+0
15
20
25
30
35
40
TIME (MIN)
CASE 1
CASE 2
CASE 3
CASE 4
CASE 5

FIGURE 35

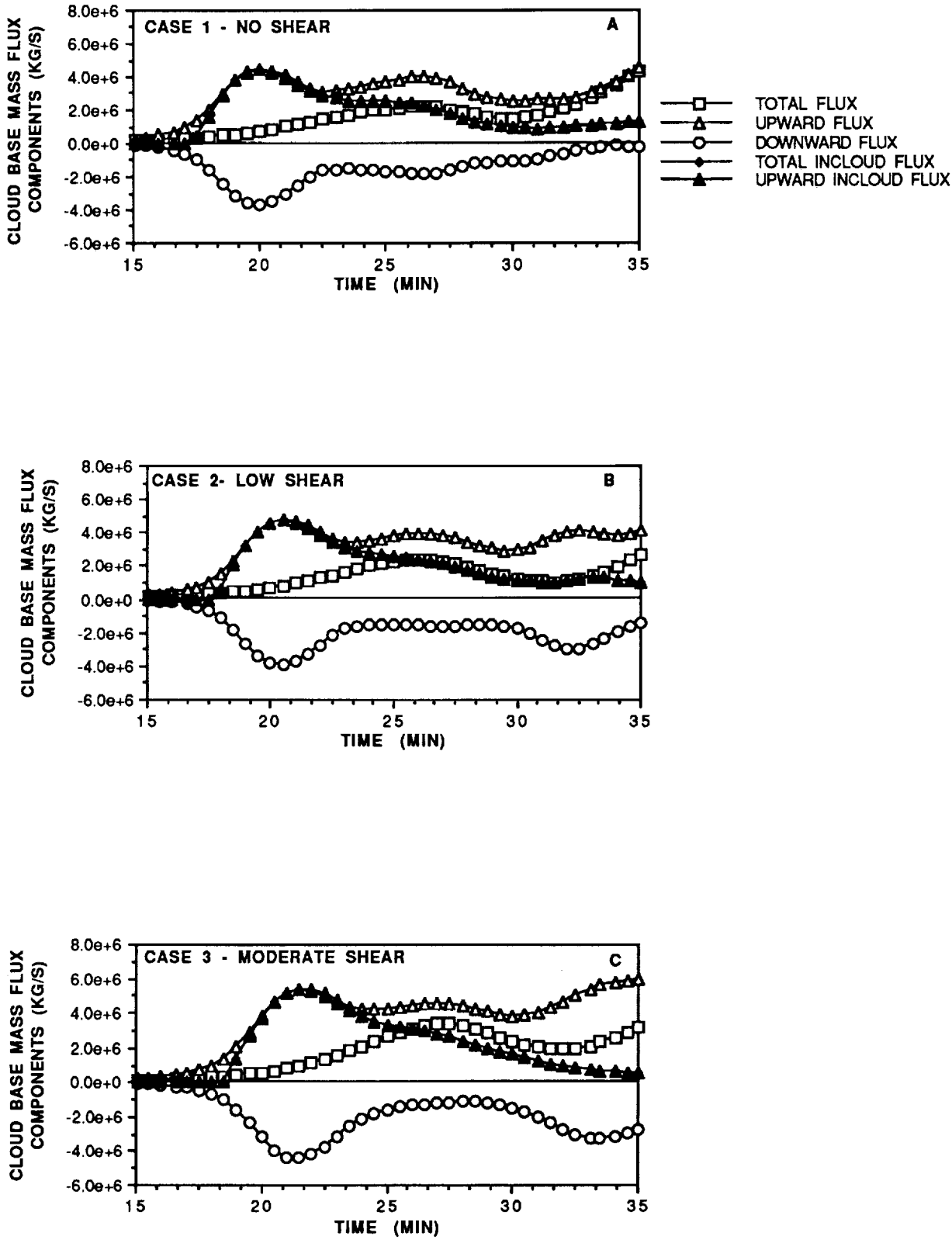
CASE 1 - NO SHEAR
A
CASE 2- LOW SHEAR
B
CASE 3 - MODERATE SHEAR
C
CLOUD BASE MASS FLUX COMPONENTS (KG/S)
8.0e+6
6.0e+6
4.0e+6
2.0e+6
0.0e+0
-2.0e+6
-4.0e+6
-6.0e+6
15
20
25
30
35
TIME (MIN)
TOTAL FLUX
UPWARD FLUX
DOWNWARD FLUX
TOTAL INCLOUD FLUX
UPWARD INCLOUD FLUX

FIGURE 36

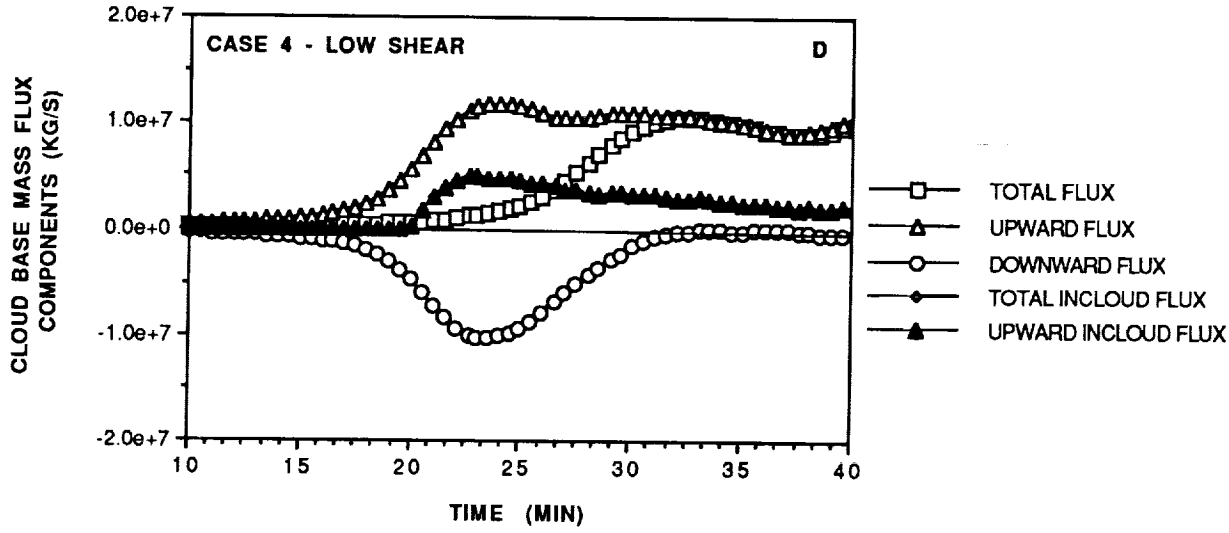

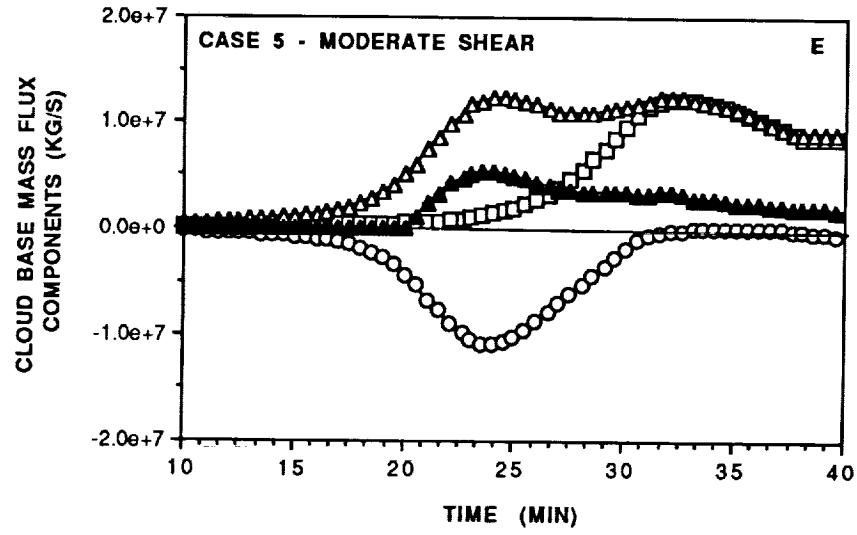

FIGURE 36 cont.

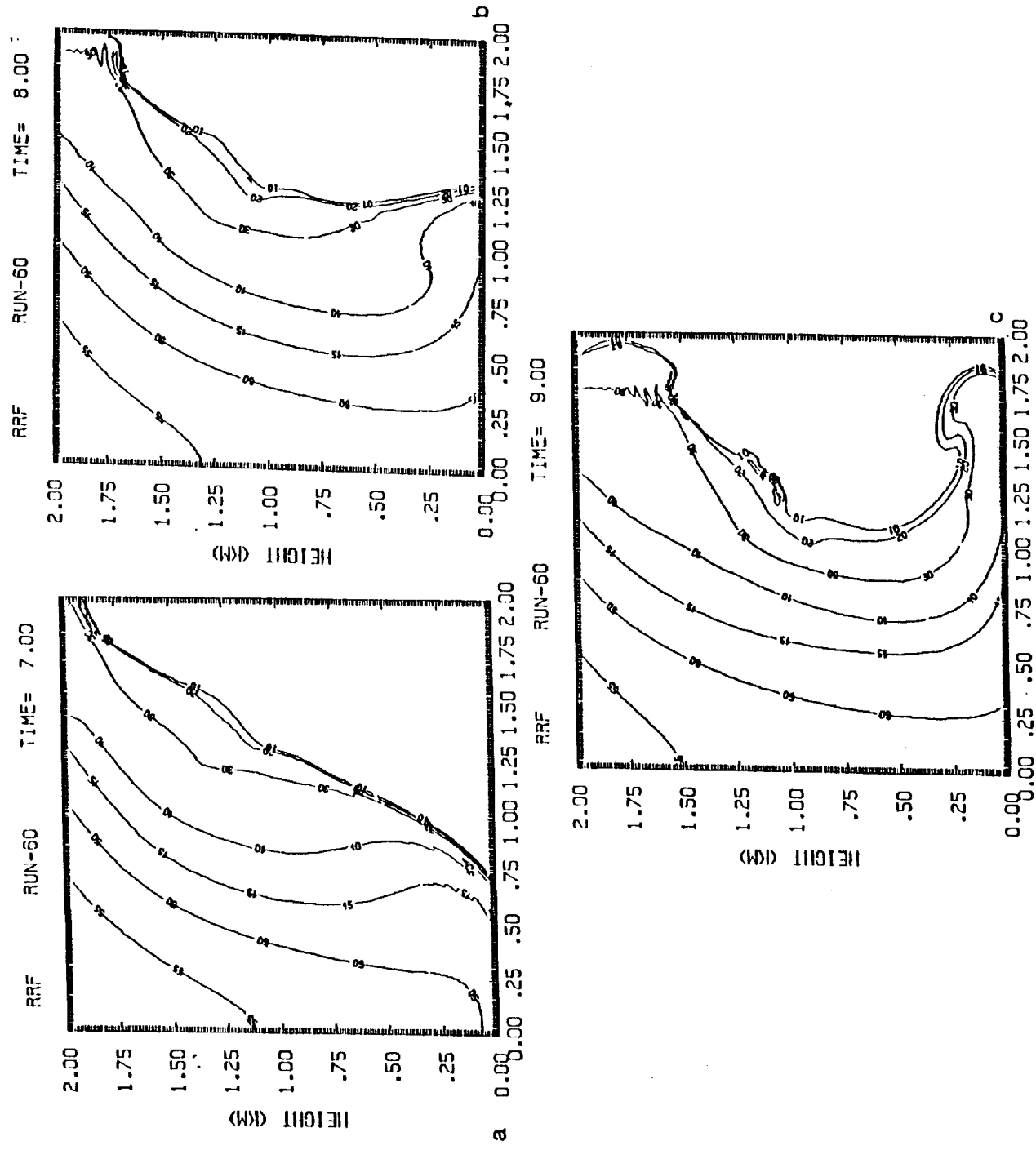

FIGURE 37

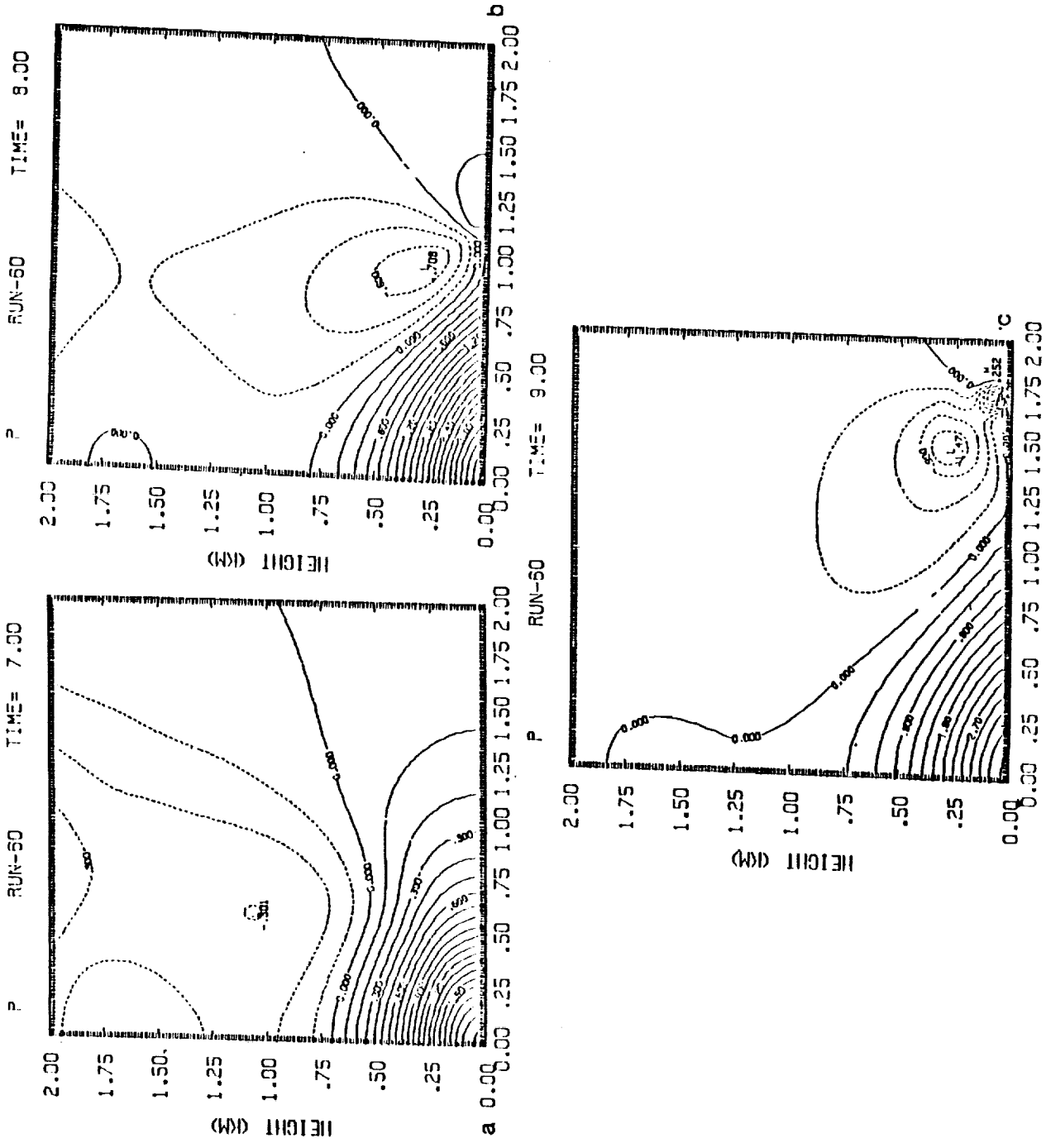
RUN-60
TIME= 7.00
HEIGHT (KM)
RUN-60
TIME= 8.00
HEIGHT (KM)
RUN-60
TIME= 9.00
HEIGHT (KM)
a
b
c

FIGURE 38

ORIGINAL PAGE IS
OF POOR QUALITY

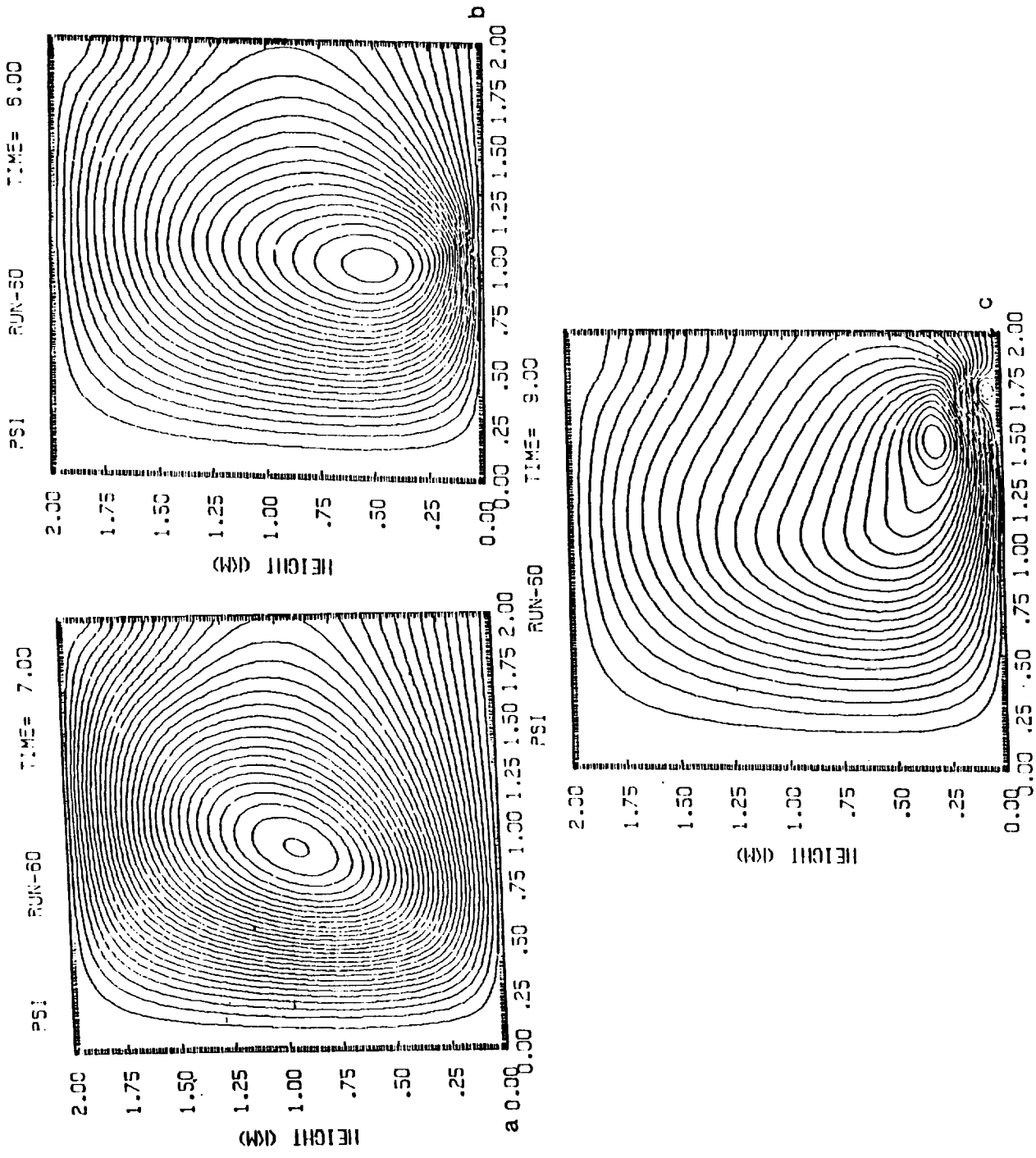

FIGURE 39

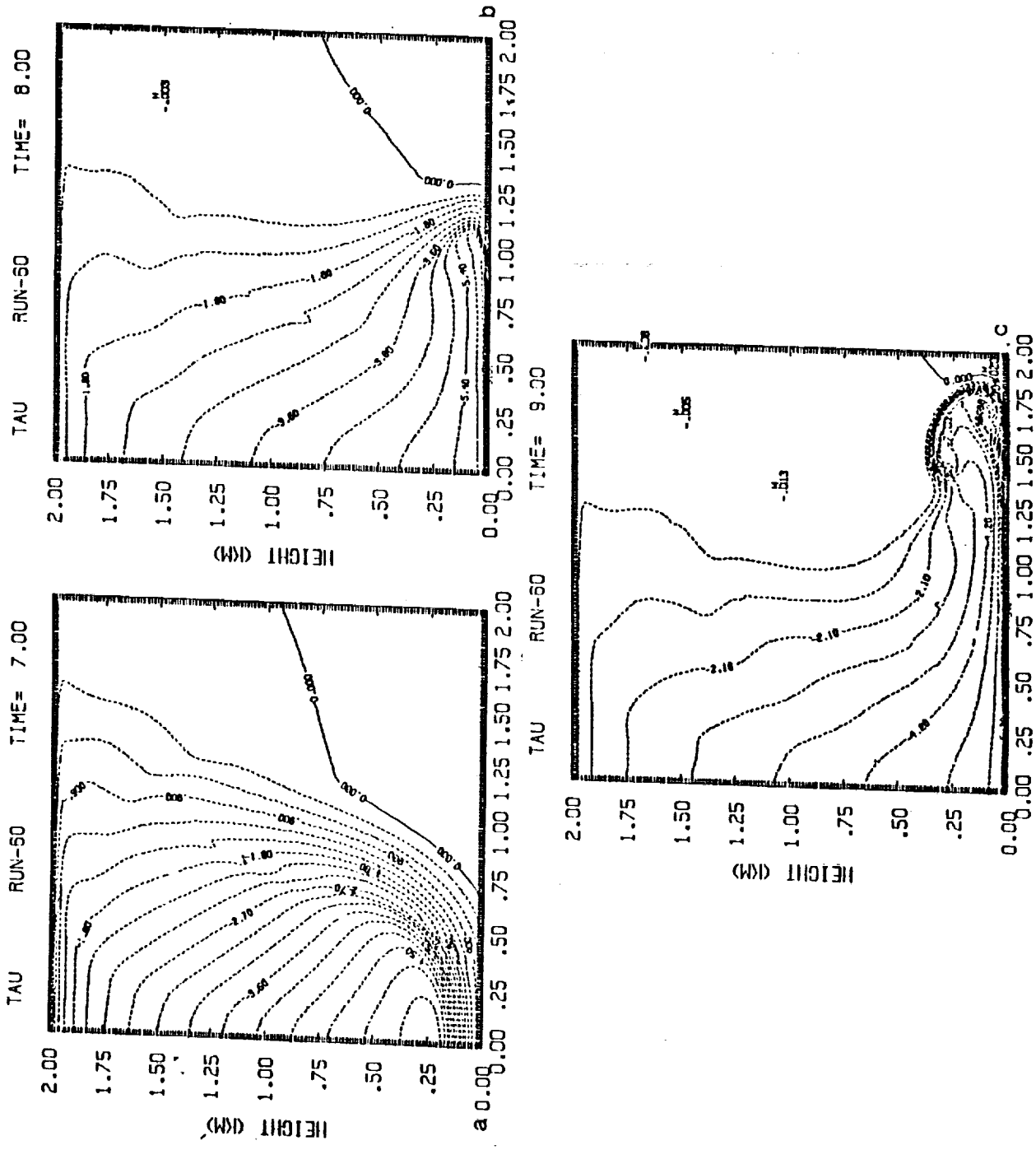
TAU RUN-60 TIME= 7.00
a
HEIGHT (KM)
TAU RUN-60 TIME= 8.00
b
HEIGHT (KM)
TAU RUN-60 TIME= 9.00
c
HEIGHT (KM)

FIGURE 40

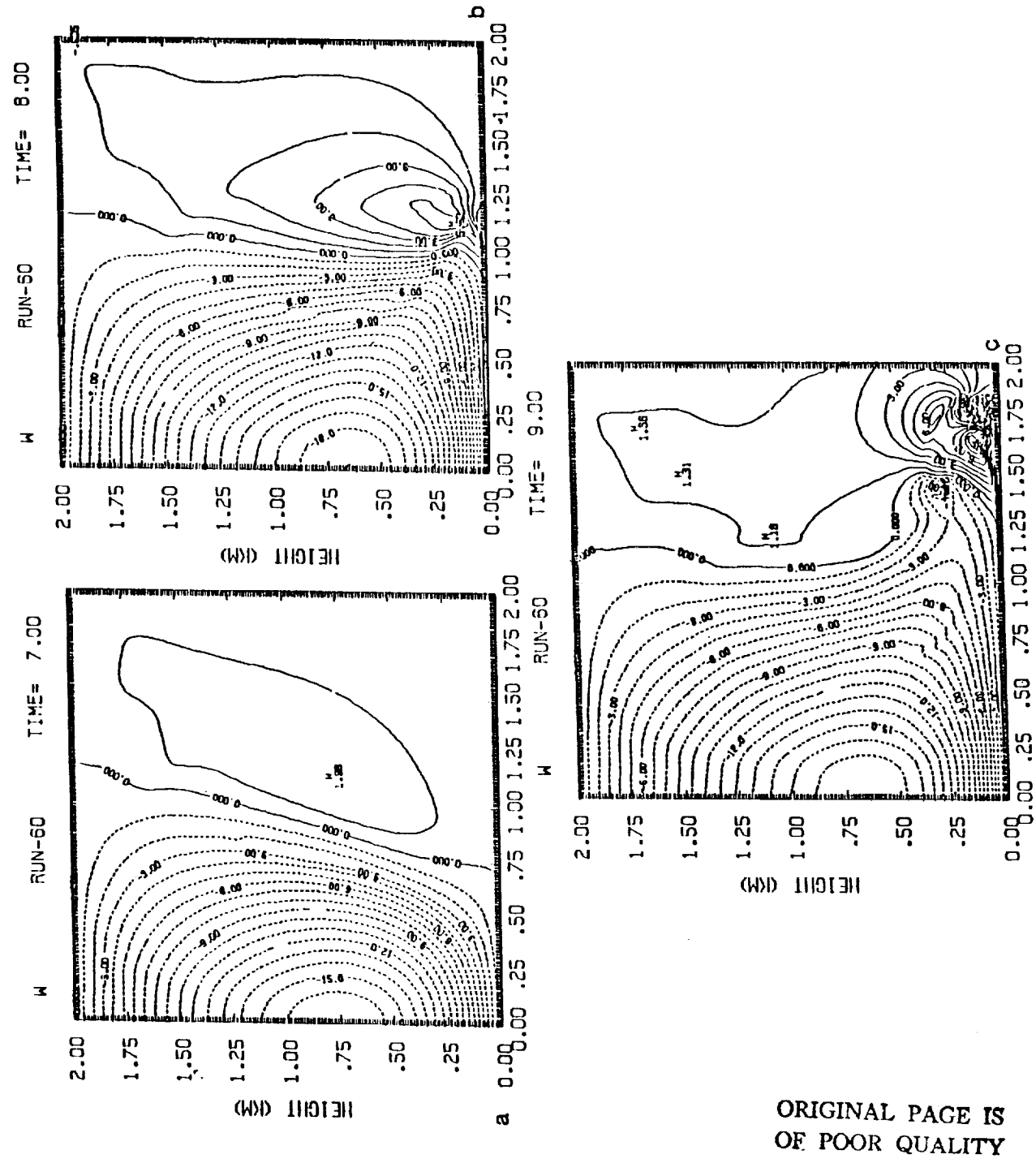

ORIGINAL PAGE IS
OF POOR QUALITY

FIGURE 41

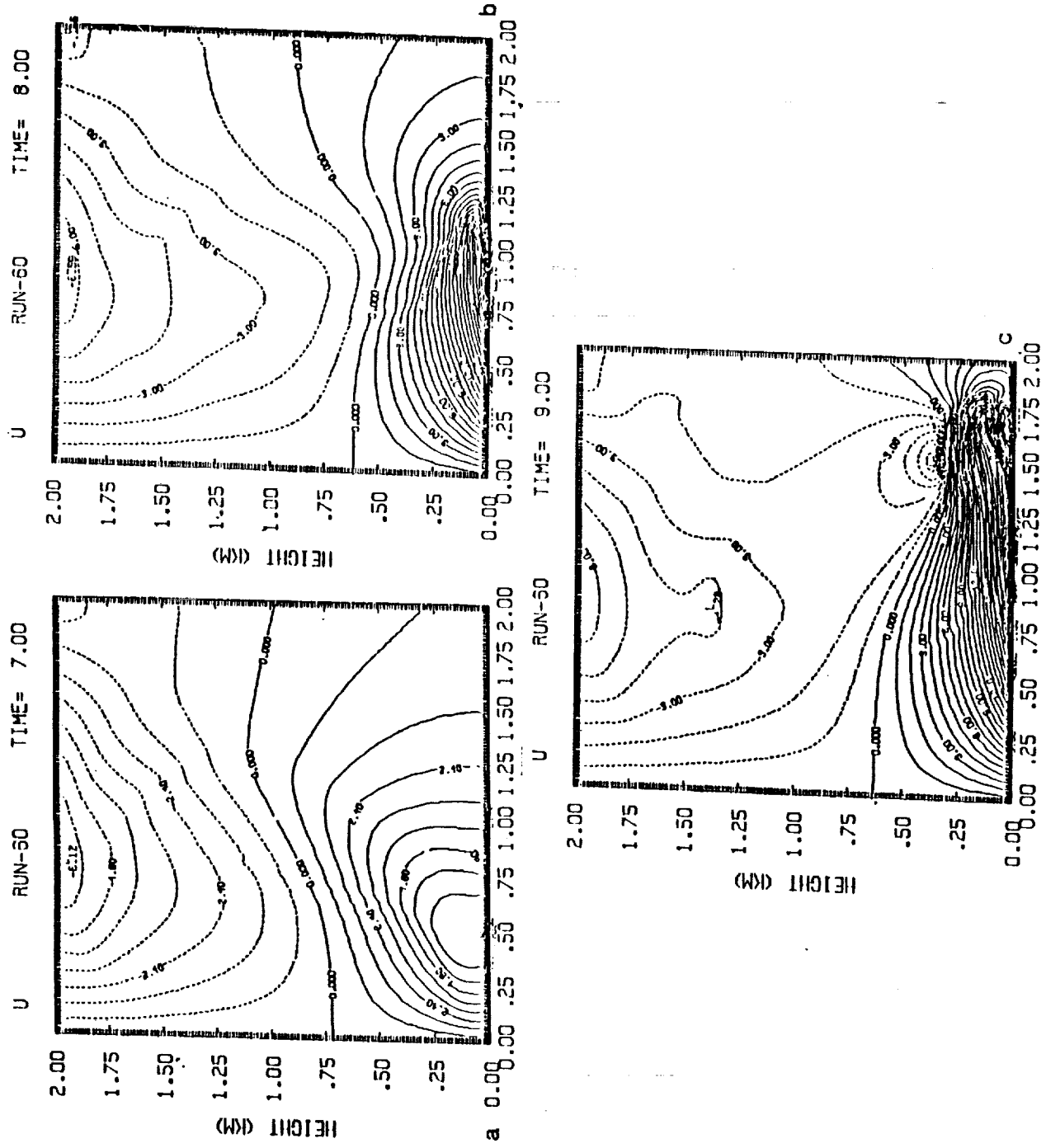
U
RUN-60
TIME= 7.00
HEIGHT (KM)
a
U
RUN-60
TIME= 8.00
HEIGHT (KM)
b
U
RUN-60
TIME= 9.00
HEIGHT (KM)
c

FIGURE 42

C-2

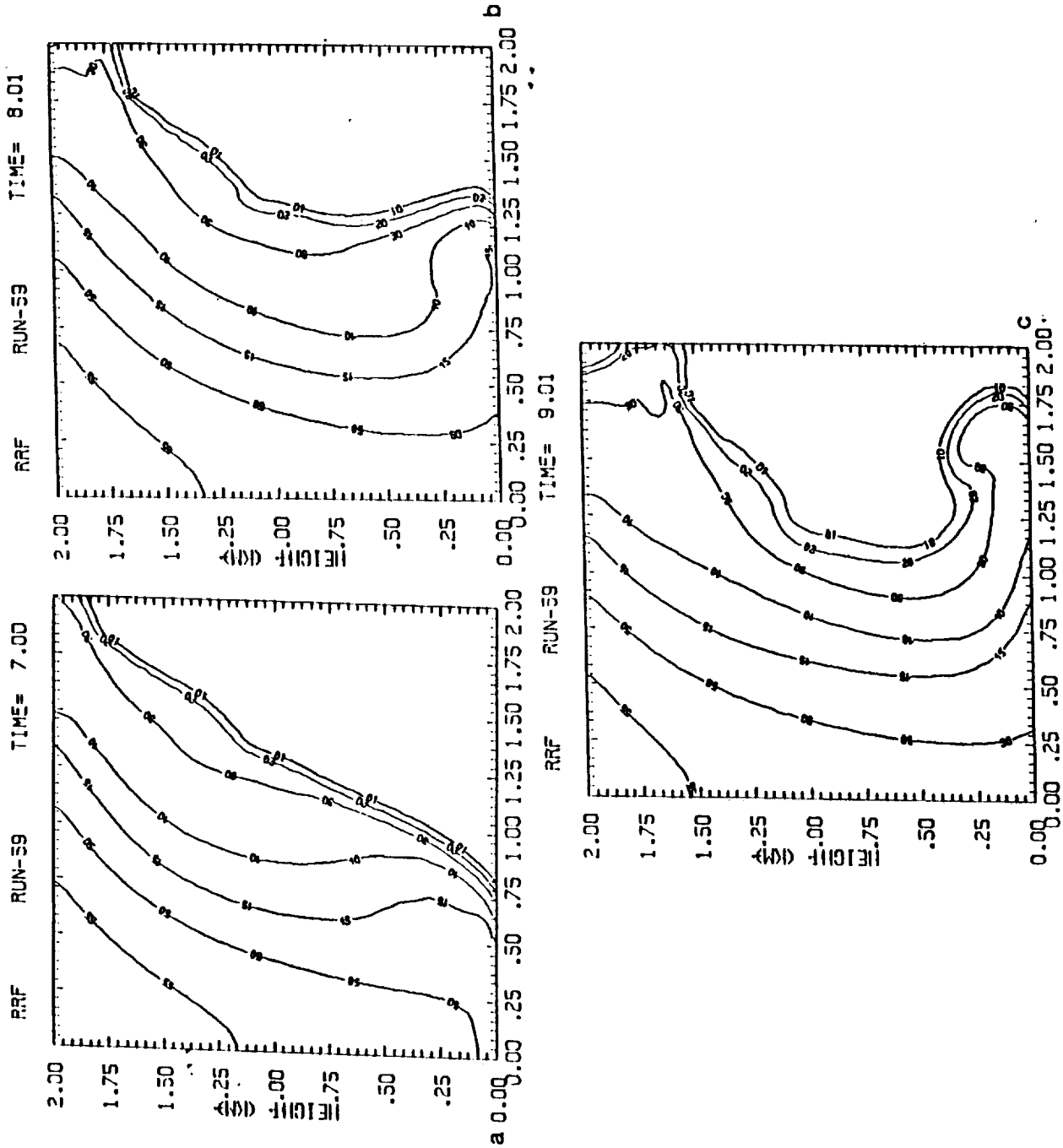
a
RRF
RUN-59
TIME= 7.00
b
RRF
RUN-59
TIME= 8.01
c
RRF
RUN-59
TIME= 9.01
HEIGHT (KM)
0.00
.25
.50
.75
1.00
1.25
1.50
1.75
2.00

FIGURE 43

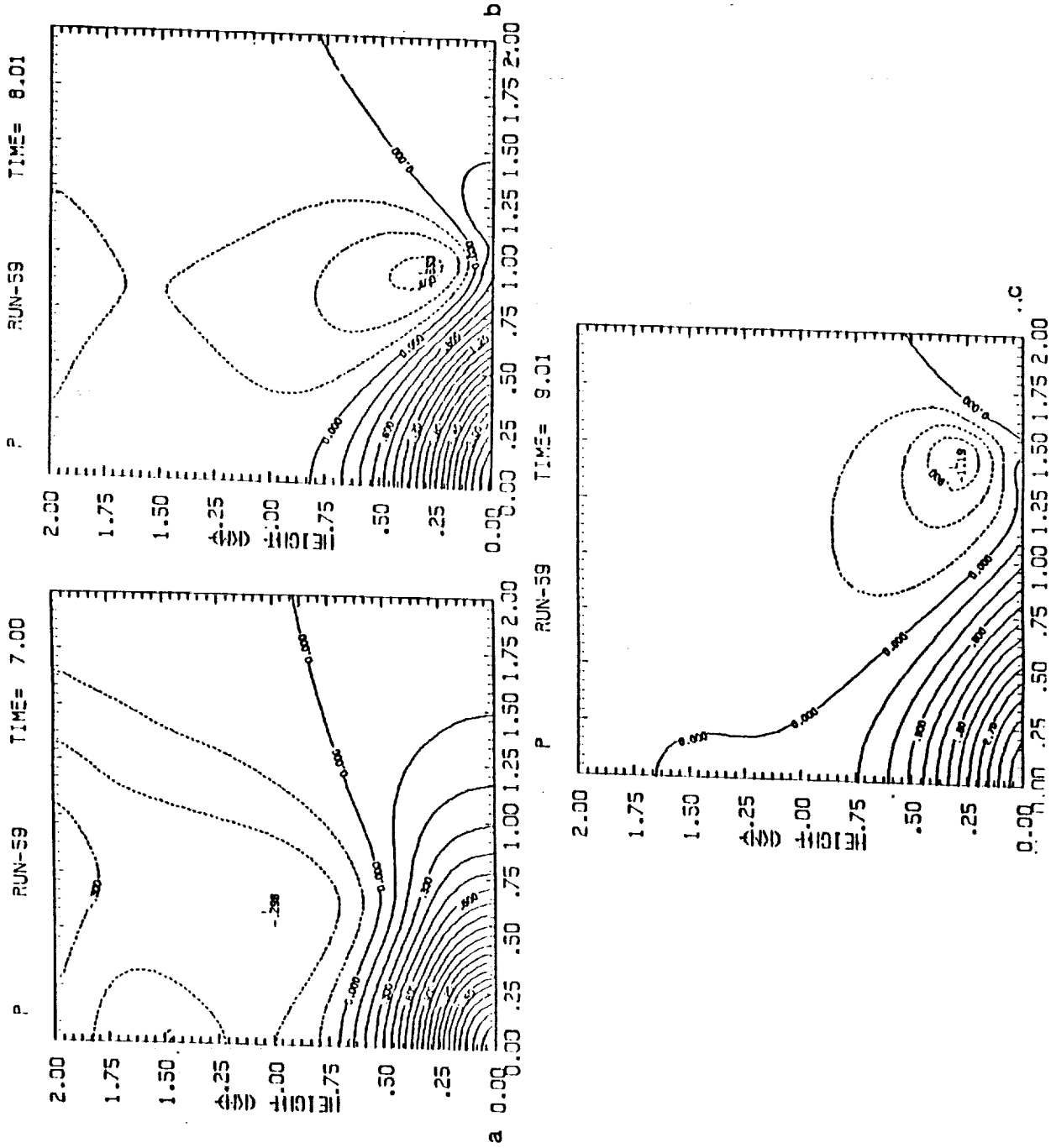
P
RUN-59
TIME= 7.00
a
P
RUN-59
TIME= 8.01
b
P
RUN-59
TIME= 9.01
c
HEIGHT AGL
0.00
.25
.50
.75
1.00
1.25
1.50
1.75
2.00

FIGURE 44

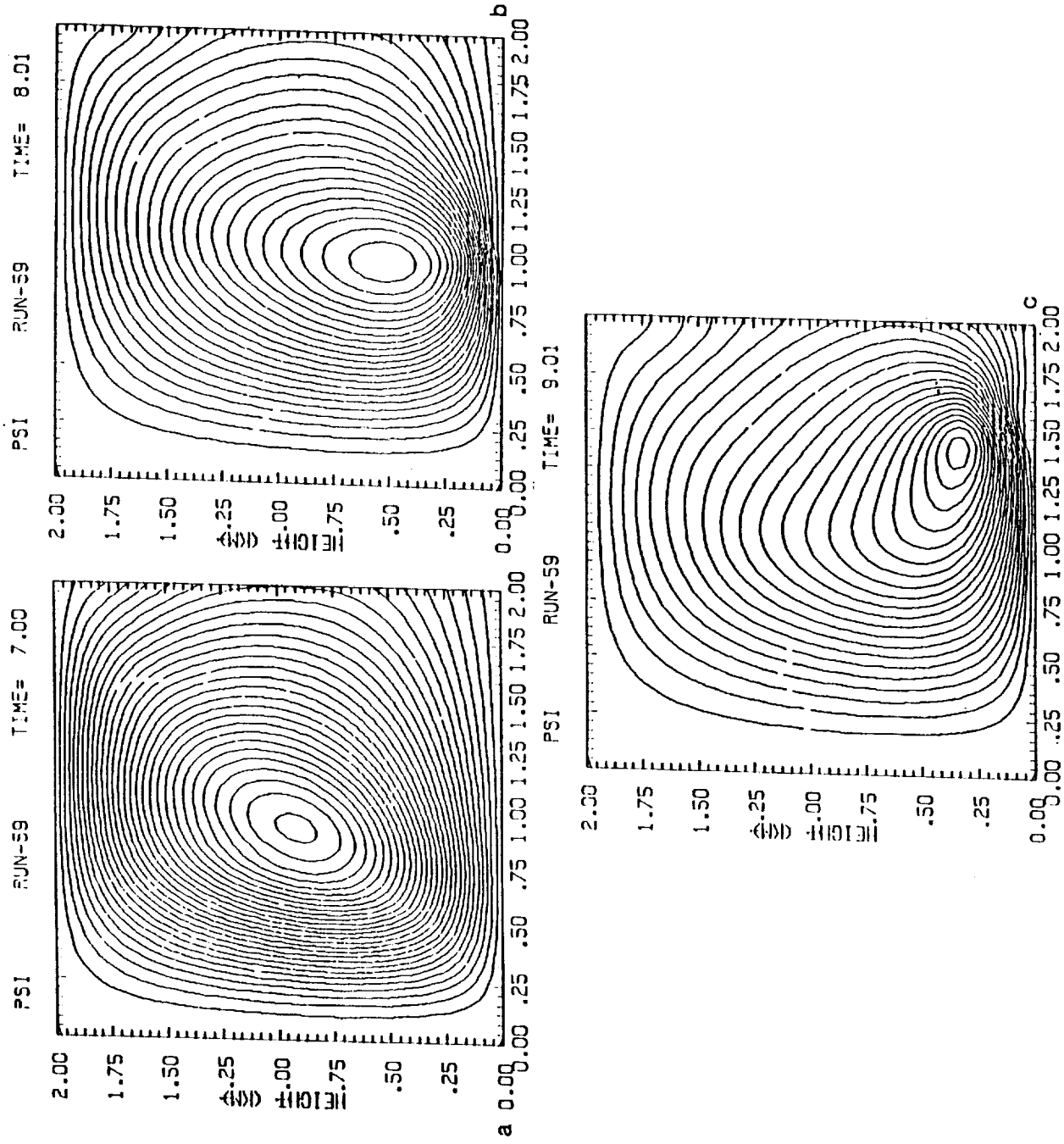
PSI
RUN-59
TIME= 7.00
a
PSI
RUN-59
TIME= 8.01
b
PSI
RUN-59
TIME= 9.01
c
HEIGHT (CM)
0.00
.25
.50
.75
1.00
1.25
1.50
1.75
2.00

FIGURE 45

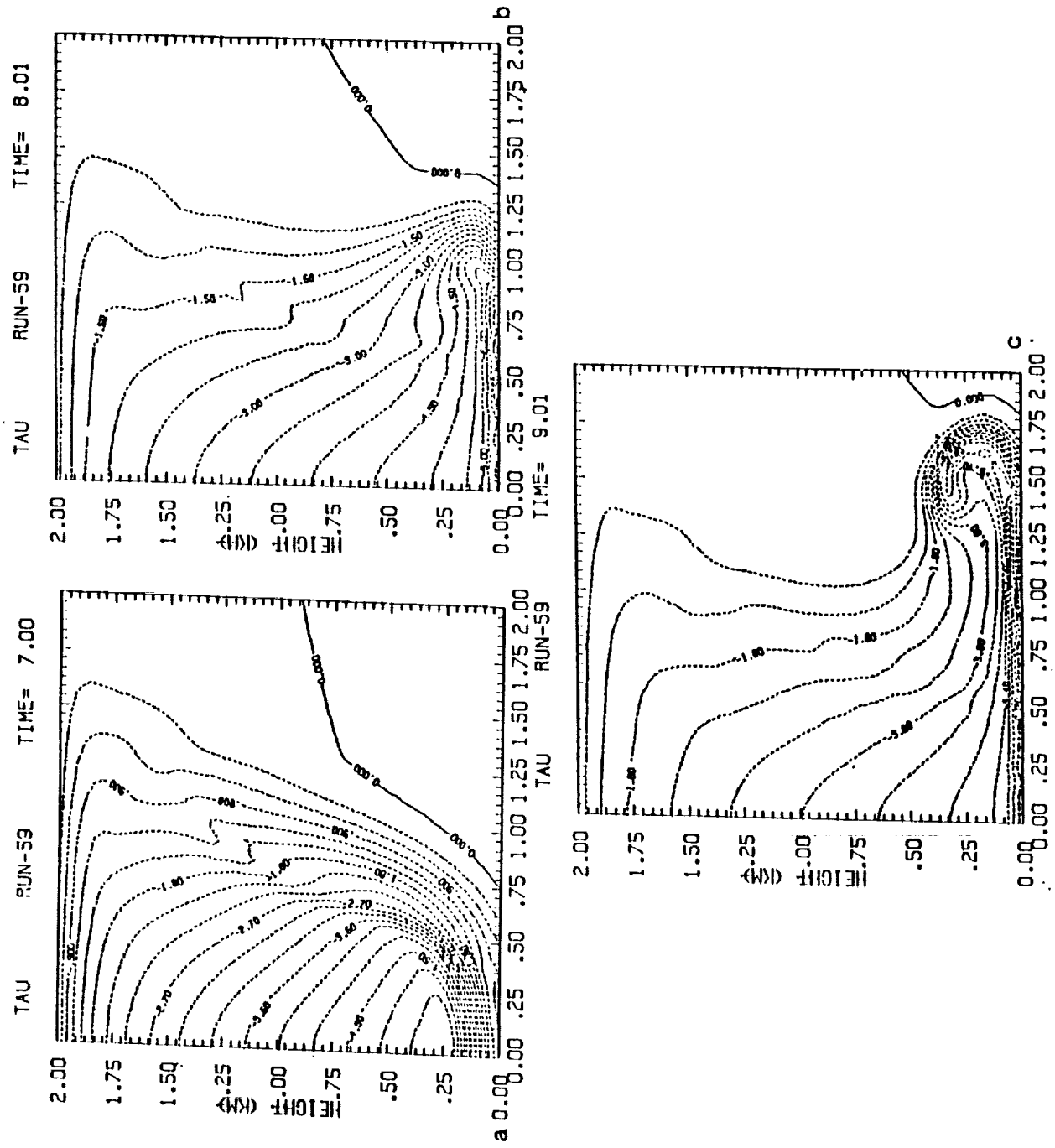
TAU RUN-59 TIME= 7.00
TAU RUN-59 TIME= 8.01
TAU RUN-59 TIME= 9.01
HEIGHT (KM)
TAU
a
b
c

FIGURE 46

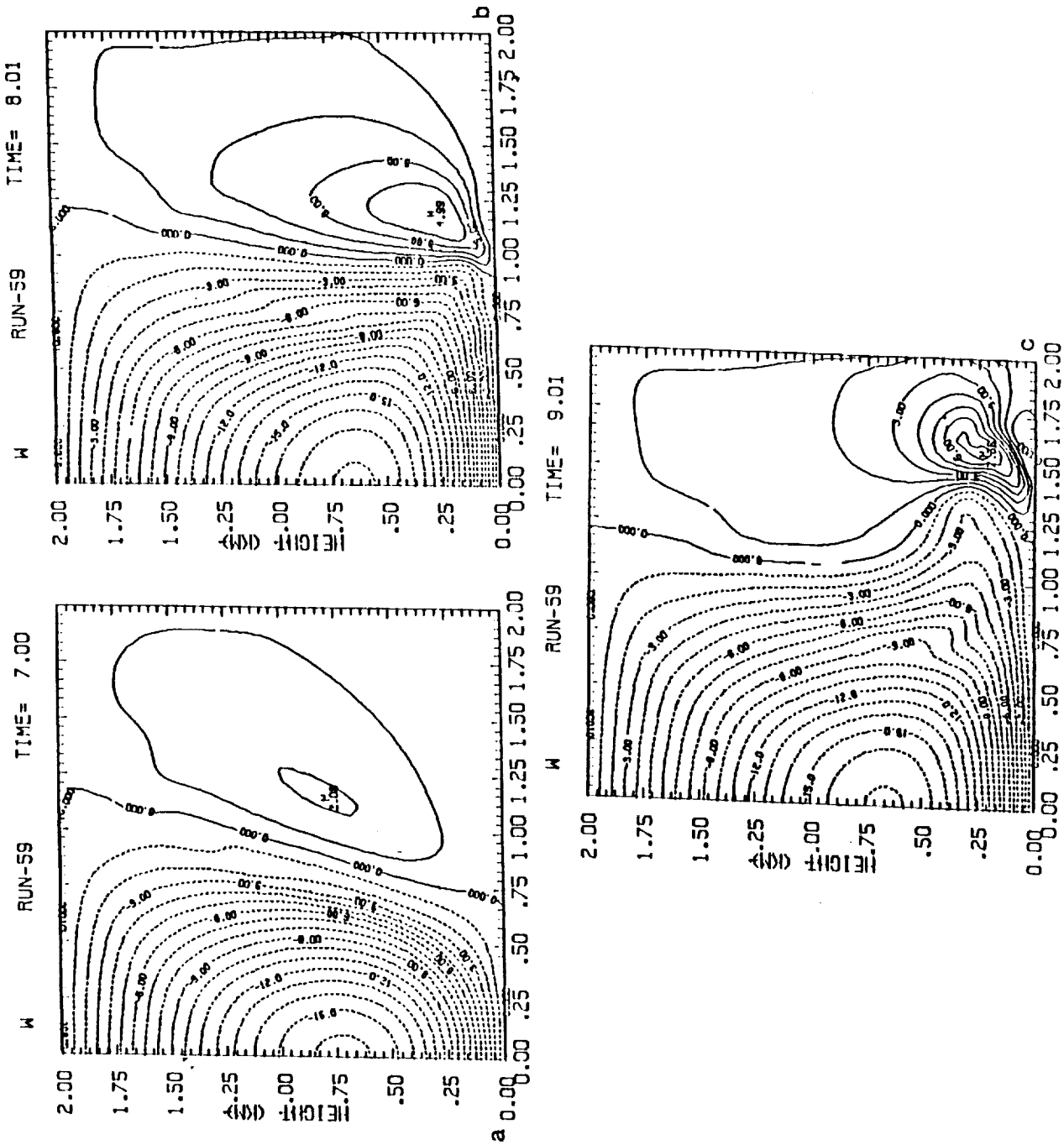
a
b
c
W
RUN-59
TIME= 7.00
TIME= 8.01
TIME= 9.01
HEIGHT (KM)
0.00
.25
.50
.75
1.00
1.25
1.50
1.75
2.00

FIGURE 47

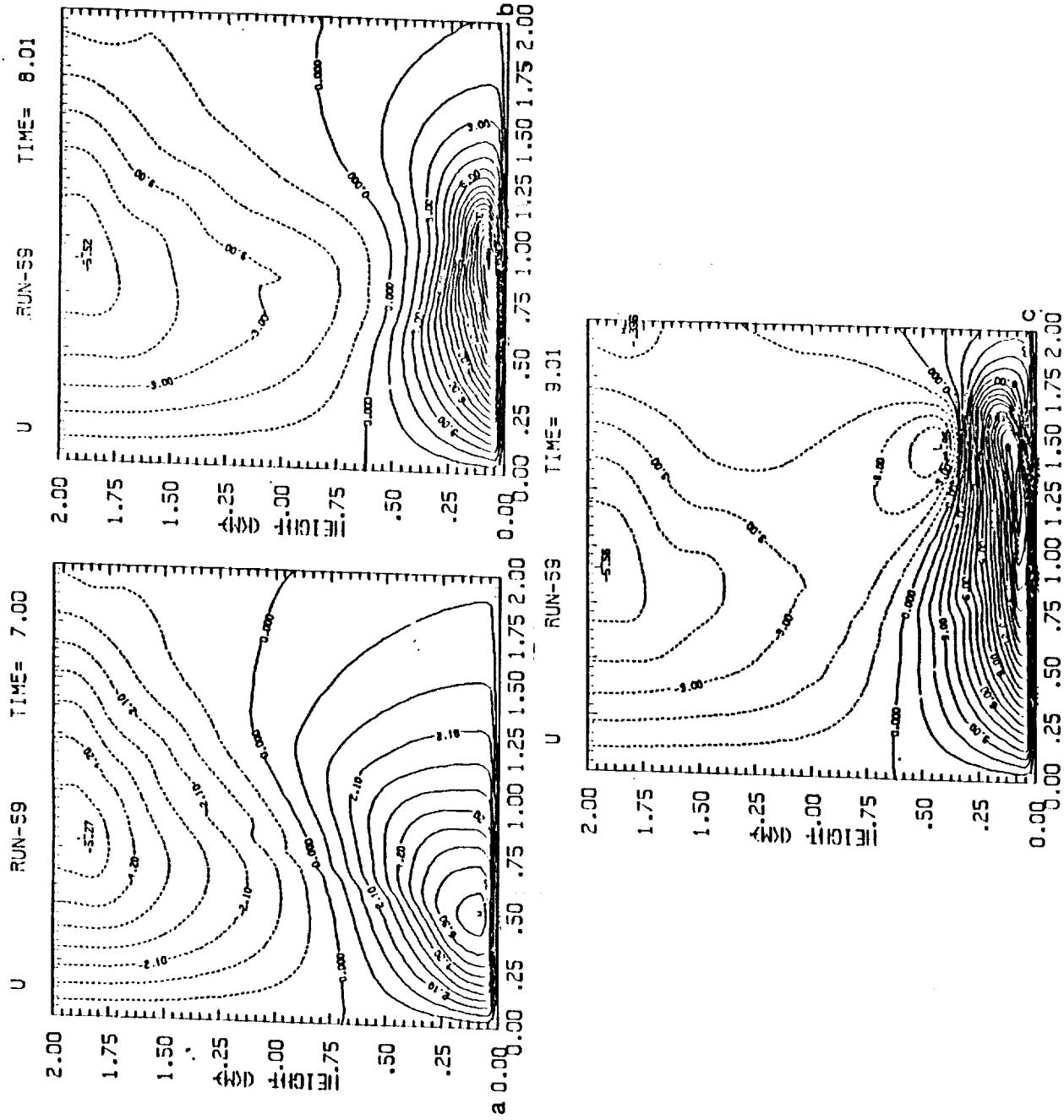

ORIGINAL PAGE IS
OF POOR QUALITY

FIGURE 48

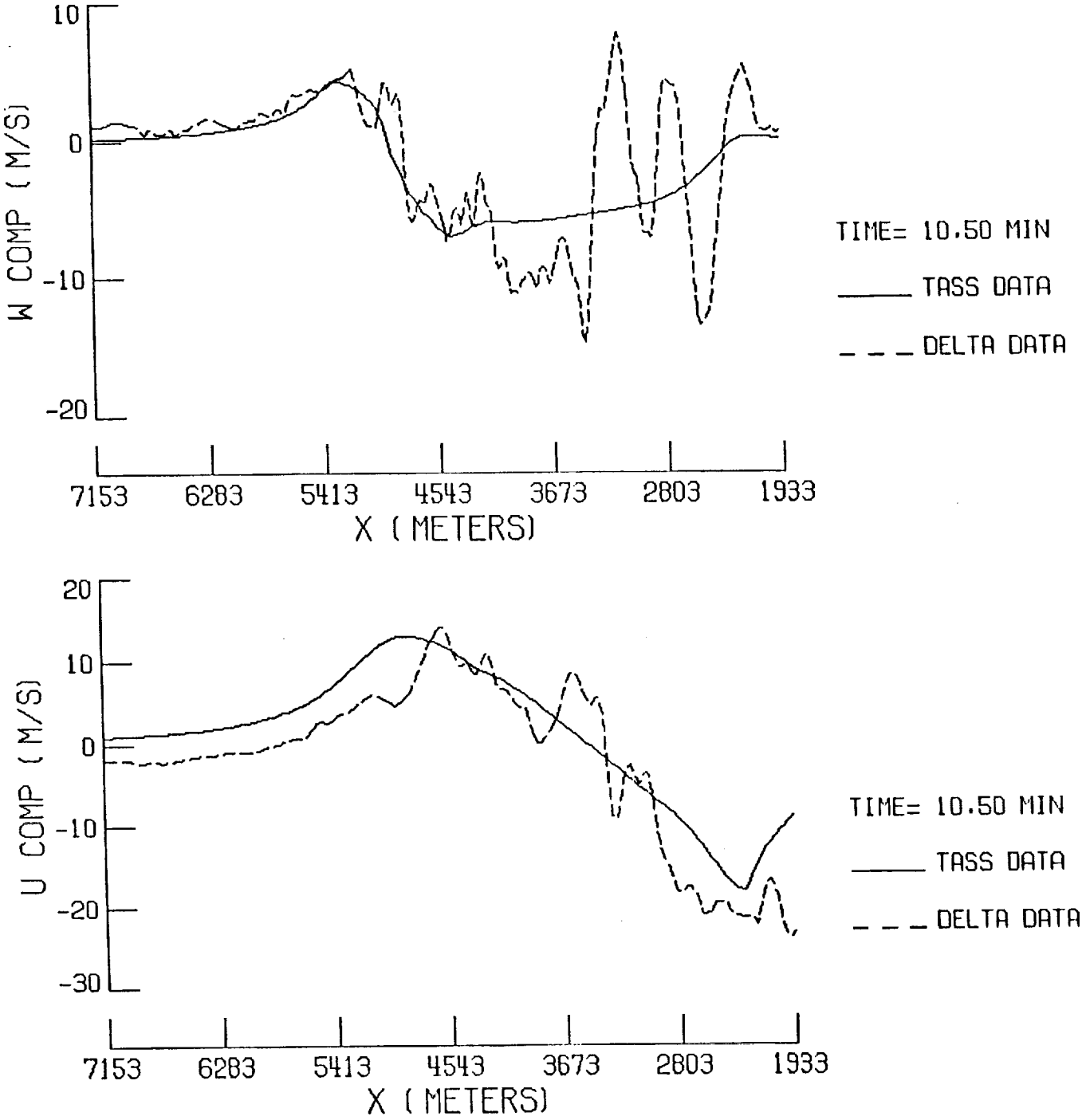
10
0
-10
-20
W COMP (M/S)
7153
6283
5413
4543
3673
2803
1933
X (METERS)
TIME= 10.50 MIN
TASS DATA
DELTA DATA
20
10
0
-10
-20
-30
U COMP (M/S)
7153
6283
5413
4543
3673
2803
1933
X (METERS)
TIME= 10.50 MIN
TASS DATA
DELTA DATA

FIGURE 49A

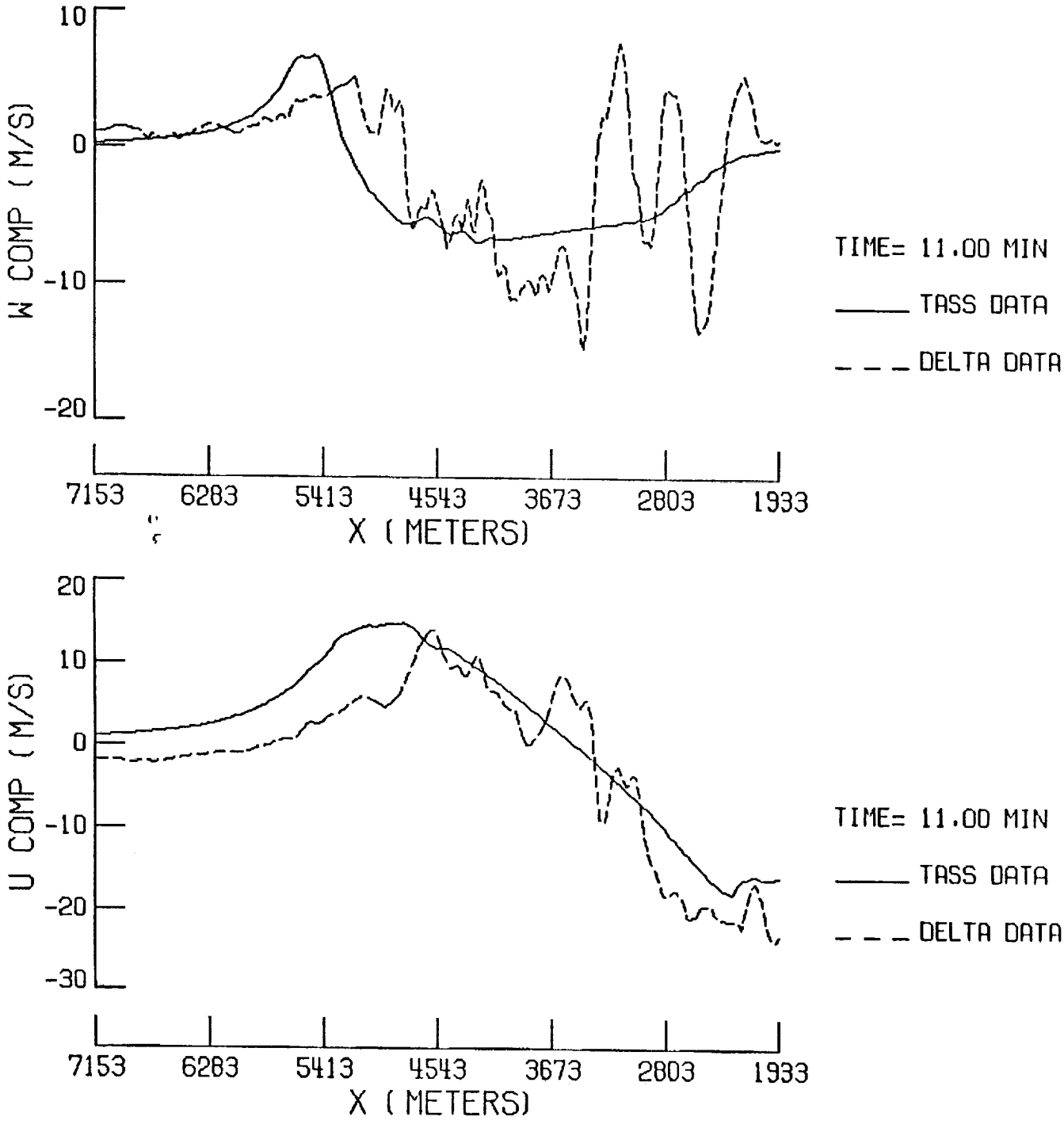
10
0
-10
-20
W COMP (M/S)
7153
6283
5413
4543
3673
2803
1933
X (METERS)
TIME= 11.00 MIN
TASS DATA
DELTA DATA
20
10
0
-10
-20
-30
U COMP (M/S)
7153
6283
5413
4543
3673
2803
1933
X (METERS)
TIME= 11.00 MIN
TASS DATA
DELTA DATA

FIGURE 49B

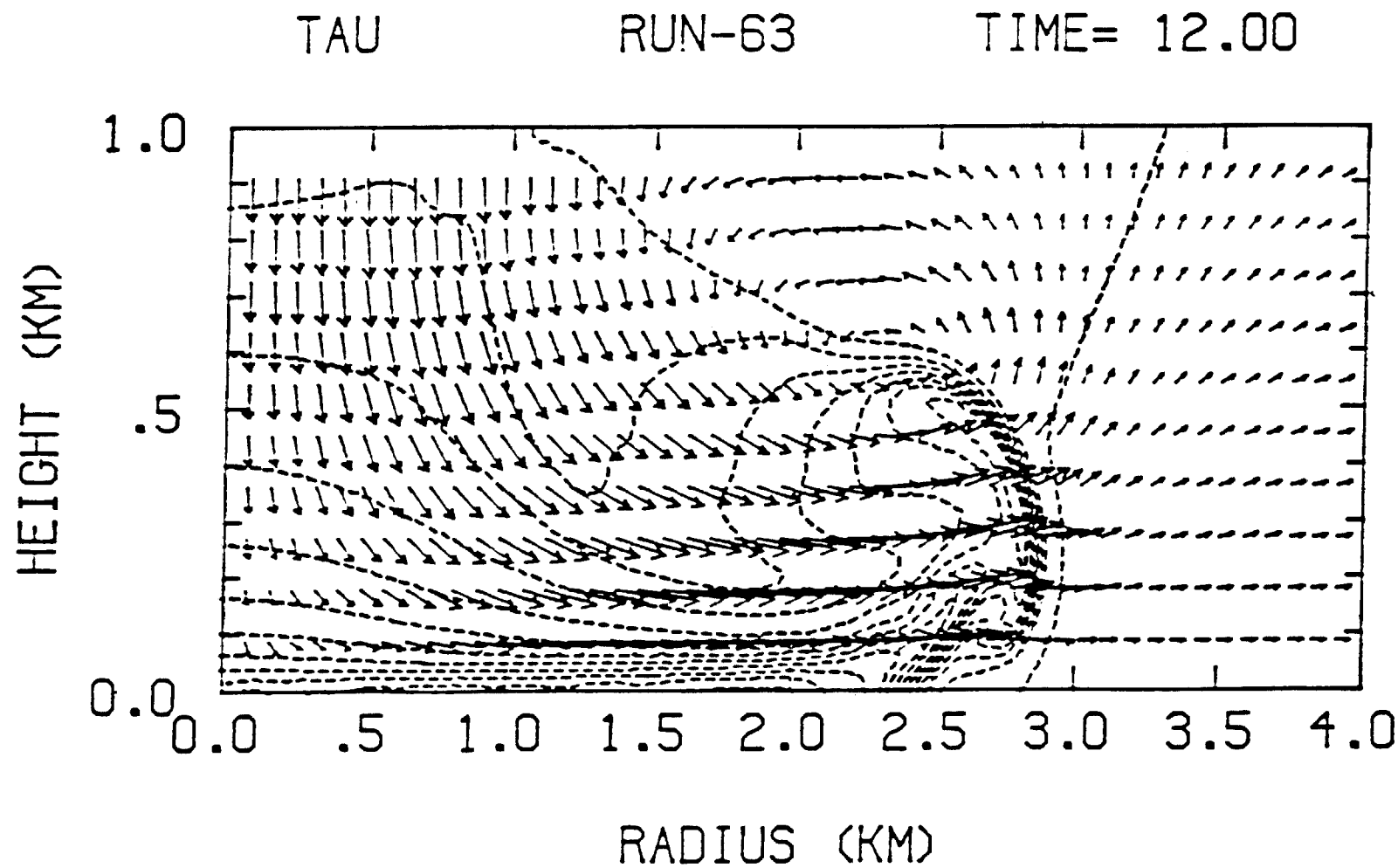
TAU
RUN-63
TIME= 12.00
1.0
.5
0.0
HEIGHT (KM)
0.0
.5
1.0
1.5
2.0
2.5
3.0
3.5
4.0
RADIUS (KM)

FIGURE 50A

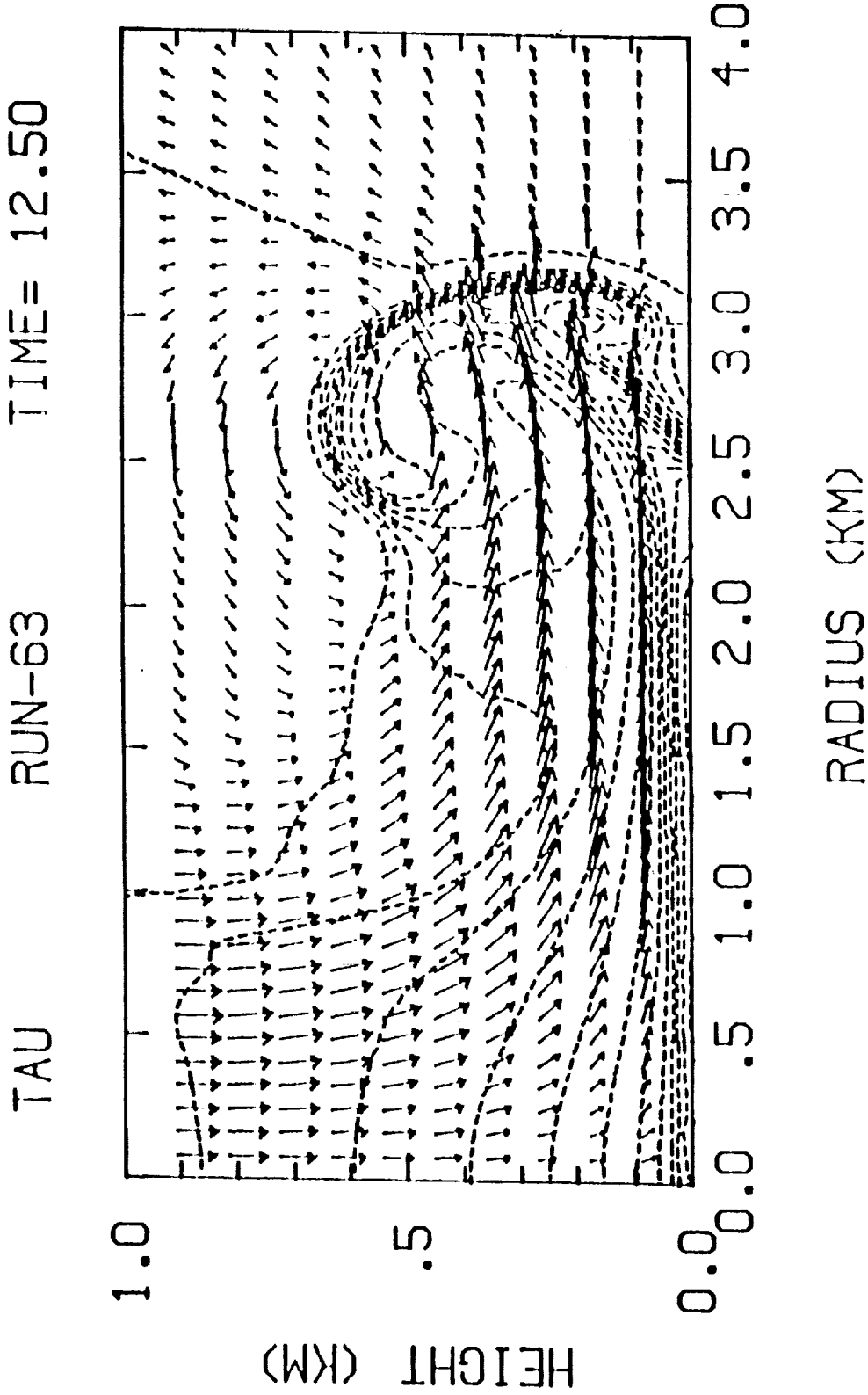
TAU
RUN-63
TIME= 12.50
HEIGHT (KM)
1.0
.5
0.0
0.0
.5
1.0
1.5
2.0
2.5
3.0
3.5
4.0
RADIUS (KM)

FIGURE 50B

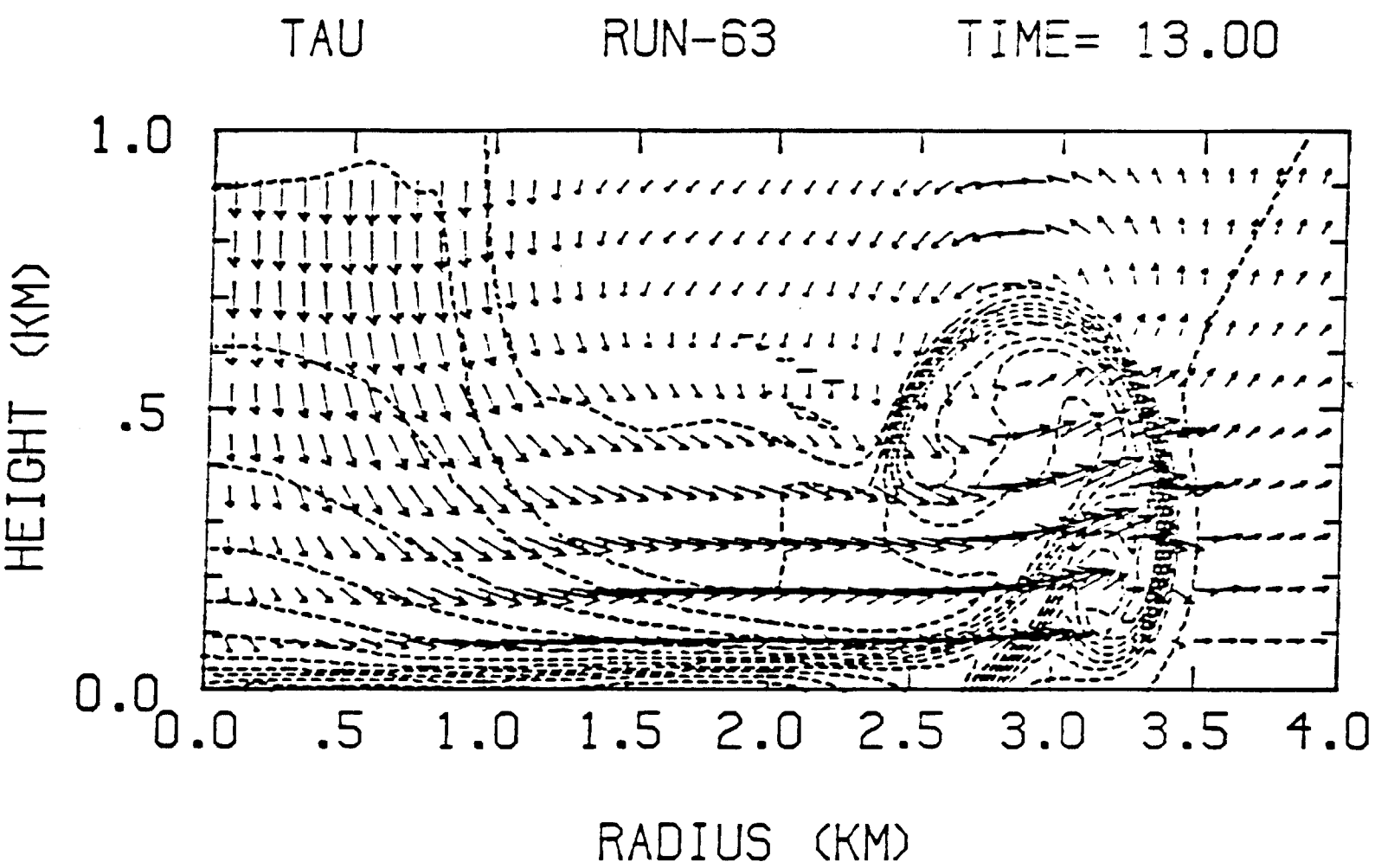
TAU
RUN-63
TIME= 13.00
1.0
.5
0.0
HEIGHT (KM)
0.0
.5
1.0
1.5
2.0
2.5
3.0
3.5
4.0
RADIUS (KM)

FIGURE 50C

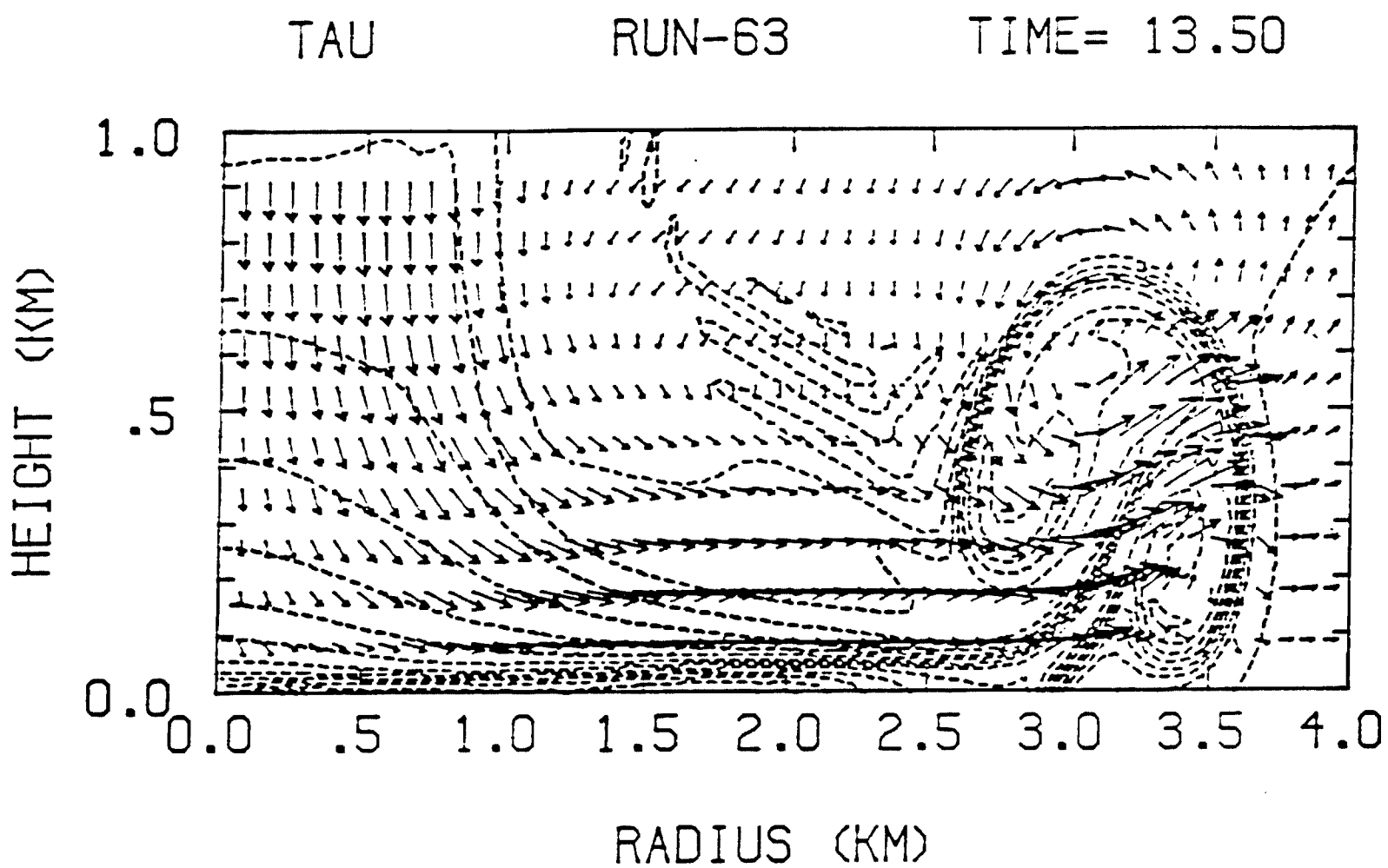
TAU
RUN-63
TIME= 13.50
1.0
.5
0.0
HEIGHT (KM)
0.0
.5
1.0
1.5
2.0
2.5
3.0
3.5
4.0
RADIUS (KM)

FIGURE 50D

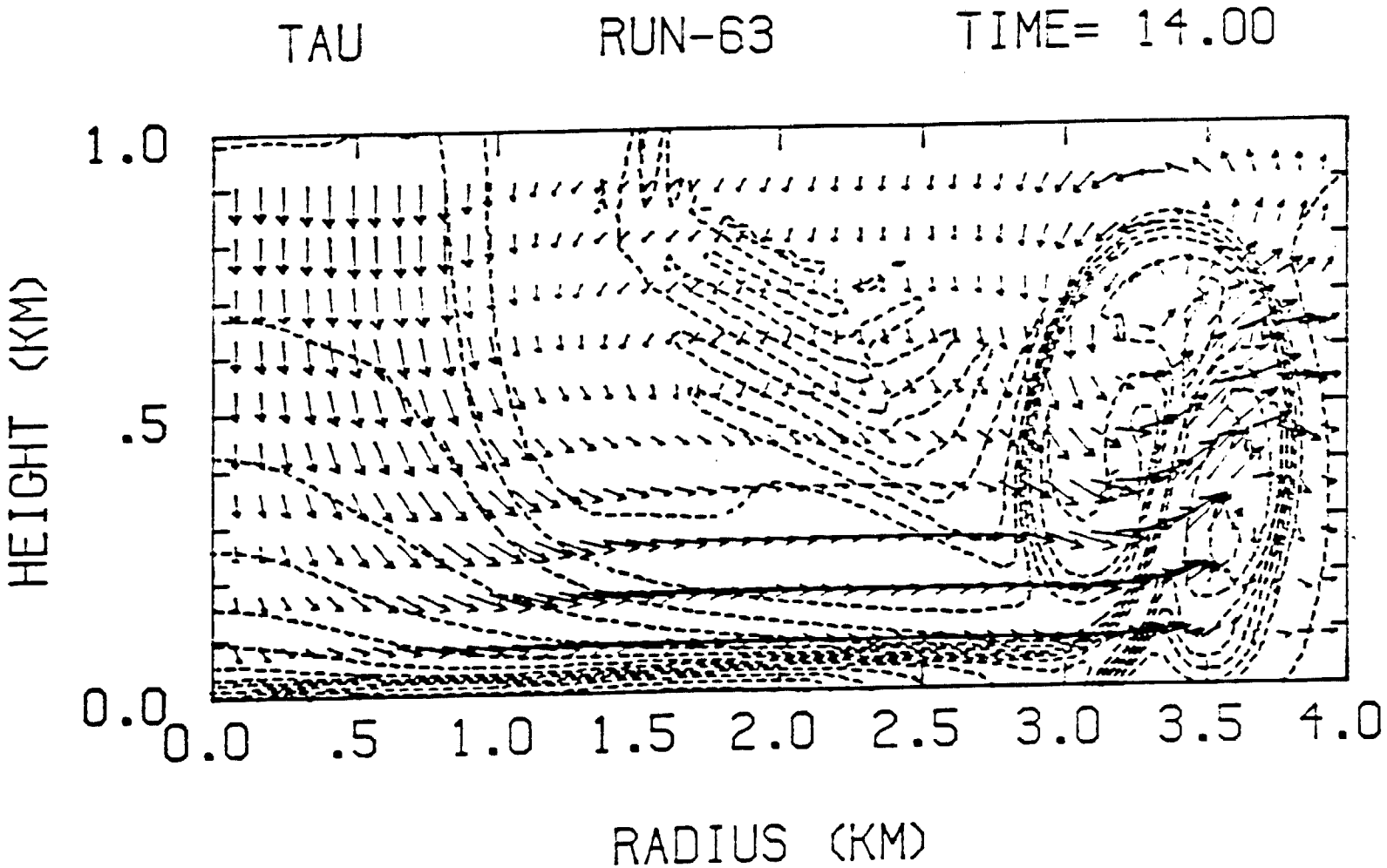
TAU
RUN-63
TIME= 14.00
1.0
.5
0.0
HEIGHT (KM)
0.0
.5
1.0
1.5
2.0
2.5
3.0
3.5
4.0
RADIUS (KM)

FIGURE 50E

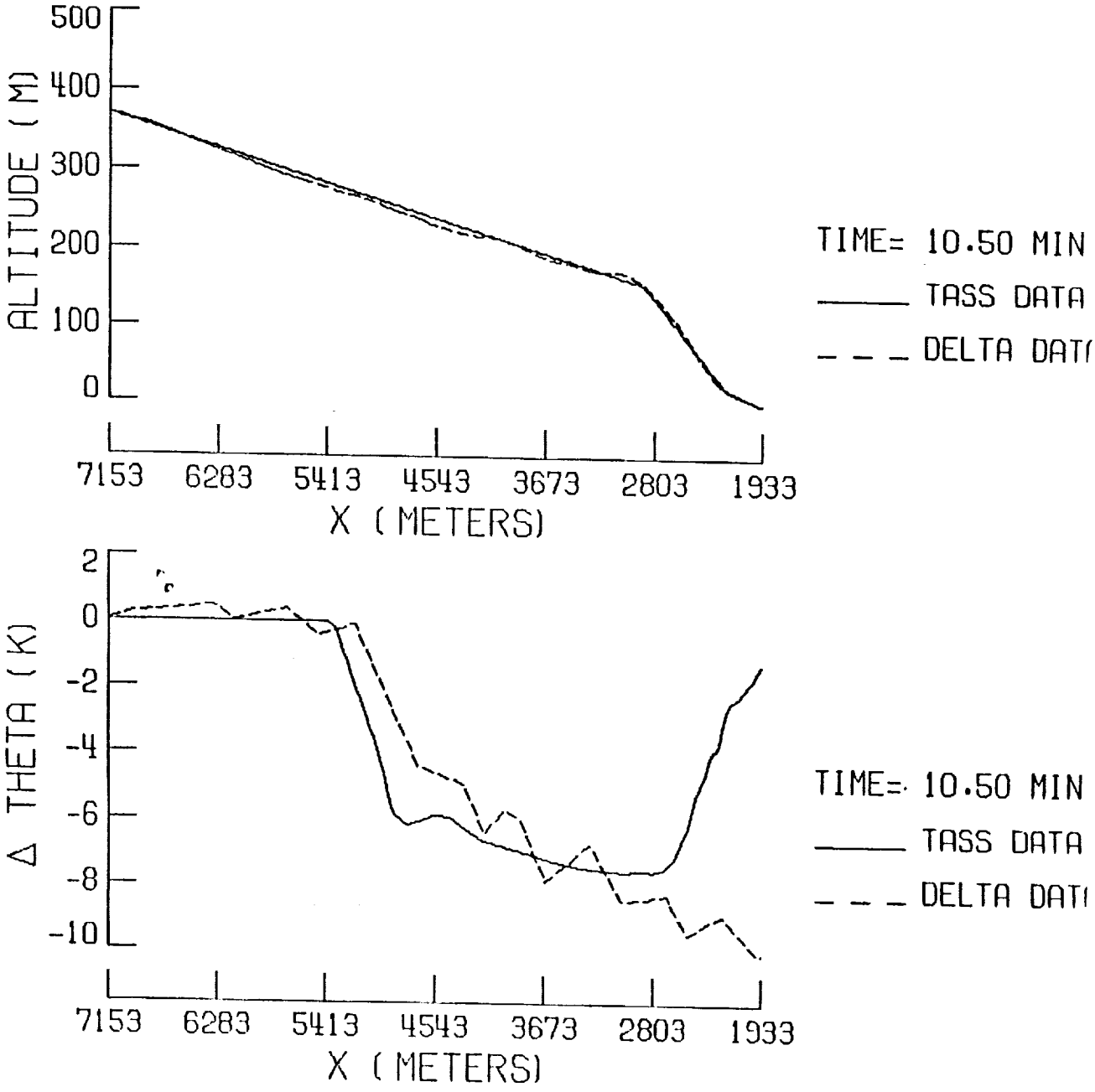
500
400
300
200
100
0
ALTITUDE (M)
7153
6283
5413
4543
3673
2803
1933
X (METERS)
TIME= 10.50 MIN
TASS DATA
DELTA DATA
2
0
-2
-4
-6
-8
-10
Δ THETA (K)
7153
6283
5413
4543
3673
2803
1933
X (METERS)
TIME= 10.50 MIN
TASS DATA
DELTA DATA

FIGURE 51A

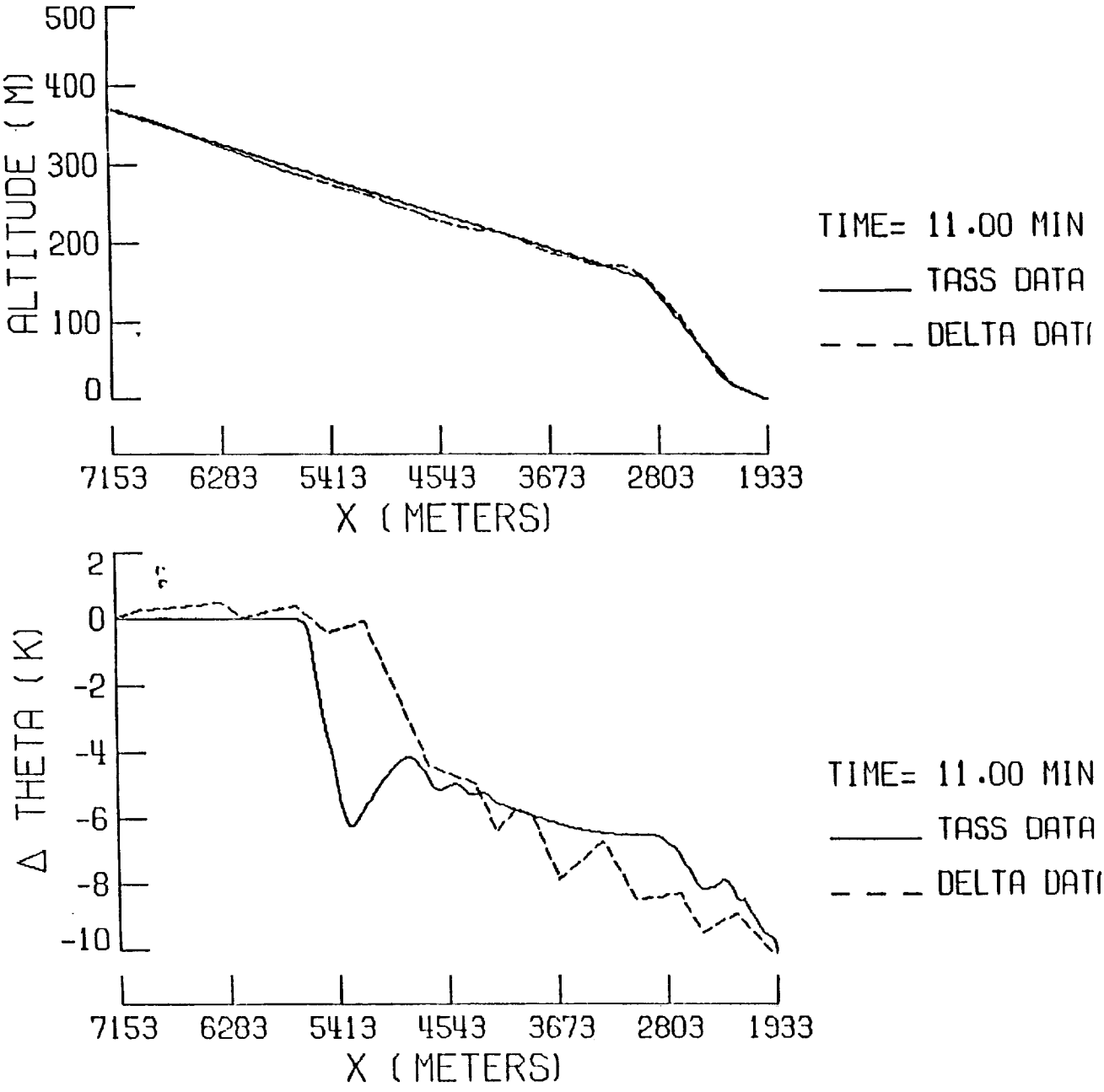
500
400
300
200
100
0
ALTITUDE (M)
7153
6283
5413
4543
3673
2803
1933
X (METERS)
TIME= 11.00 MIN
TASS DATA
DELTA DATA
2
0
-2
-4
-6
-8
-10
Δ THETA (K)
7153
6283
5413
4543
3673
2803
1933
X (METERS)
TIME= 11.00 MIN
TASS DATA
DELTA DATA

FIGURE 51B

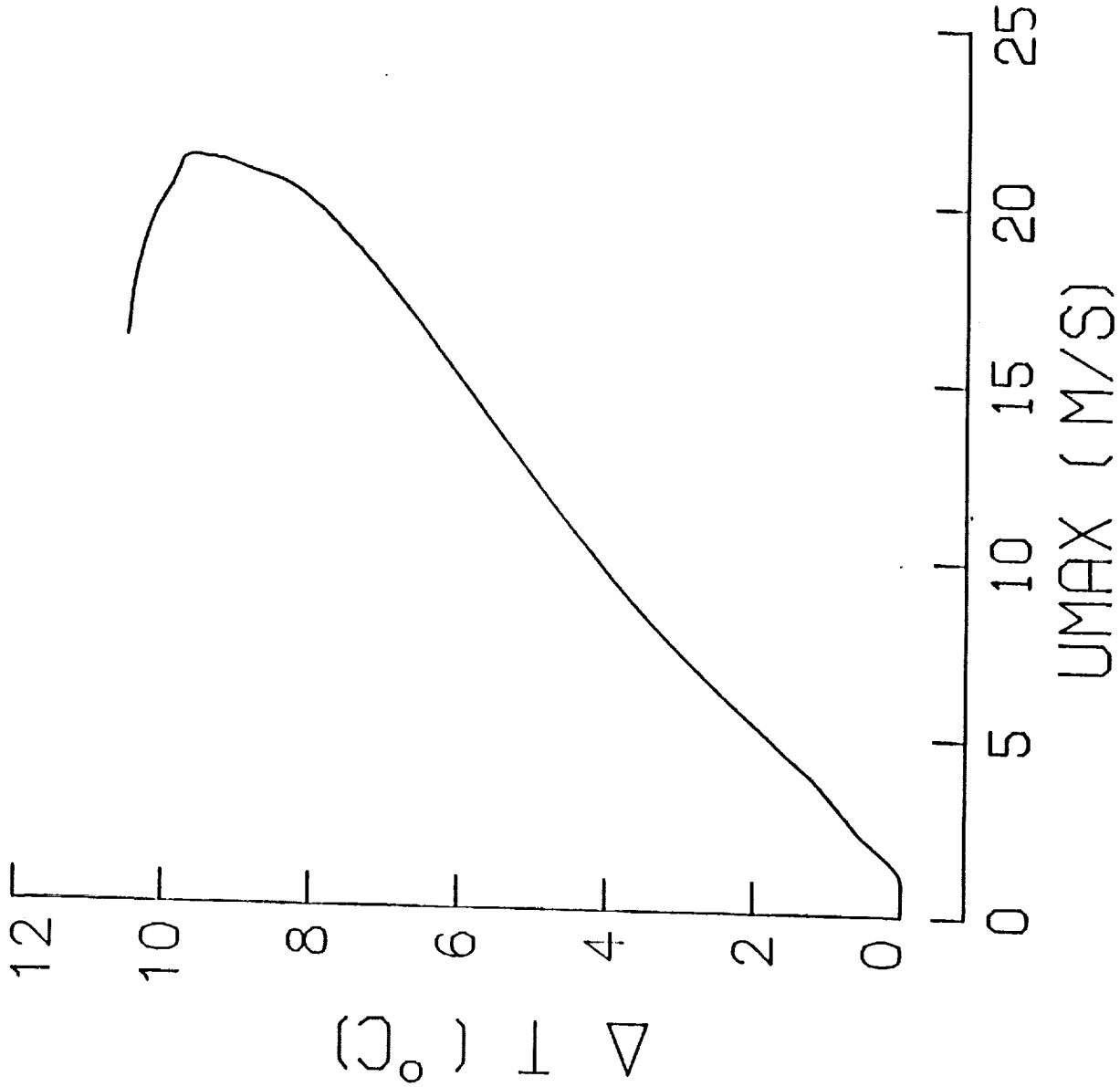

FIGURE 52

NASA
National Aeronautics and Space Administration

Report Documentation Page

1. Report No.	2. Government Accession No.	3. Recipient's Catalog No.
NASA CR-4262		

4. Title and Subtitle

MESOSCALE ACID DEPOSITION MODELING STUDIES

5. Report Date

December 1989

6. Performing Organization Code

7. Author(s)

Michael L. Kaplan, F.H. Proctor, John W. Zack, V. Mohan Karyampudi, P.E. Price, M.D. Bousquet, and G.D. Coats

8. Performing Organization Report No.

10. Work Unit No.

146-90-04-52

9. Performing Organization Name and Address

MESO, Inc.
28 Research Drive
Hampton, VA 23666-1325

11. Contract or Grant No.

NAS1-18336

13. Type of Report and Period Covered

Contractor Report

12. Sponsoring Agency Name and Address

National Aeronautics and Space Administration
Langley Research Center
Hampton, VA 23665-5225

14. Sponsoring Agency Code

15. Supplementary Notes

Langley Technical Monitor: John A. Ritter
Final Report

16. Abstract The work performed can be logically partitioned into two basic applied research topic areas : 1) the use of meso and cloudscale numerical atmospheric simulation models in support of the scientific goals of the joint EPA/DOE Mesoscale Acid Deposition Studies Project, and 2) the use of cloud and mesoscale numerical atmospheric simulation models in support of the joint NASA/FAA Convection-Initiated Low-Level Wind Shear Program. The two numerical models used are the Mesoscale Atmospheric Simulation System (MASS) and the Terminal Area Simulation System (TASS).

The work performed in support of the EPA/DOE MADS Project included the development of meteorological data bases for the initialization of chemistry models, the testing and implementation of new planetary boundary layer parameterization schemes in the MASS model, the simulation of transport and precipitation for MADS case studies employing the MASS model, and the use of the TASS model in the simulation of cloud statistics and the complex transport of conservative tracers within simulated cumuloform clouds.

The work performed in support of the NASA/FAA Wind Shear Program included the use of the TASS model in the simulation of the dynamical processes within convective cloud systems, the analyses of the sensitivity of microburst intensity and general characteristics as a function of the atmospheric environment within which they are formed, comparisons of TASS model microburst simulation results to observed data sets, and the generation of simulated wind shear data bases for use by the aviation meteorological community in the evaluation of flight hazards caused by microbursts.

17. Key Words (Suggested by Author(s))	18. Distribution Statement
MASS, TASS, transport, numerical models, microbursts	Unclassified - Unlimited Subject Category 73

19. Security Classif. (of this report)	20. Security Classif. (of this page)	21. No. of pages	22. Price
Unclassified	Unclassified	120	A06

NASA FORM 1626 OCT 86

For Sale by the National Technical Information Service, Springfield, VA 22161-2171

NASA-Langley, 1989